Determinants of cAMP Affinity in PKA

Dissecting the Determinants of cAMP Affinity in Protein Kinase A

BY

KODY JOHN MOLESCHI, B.Sc.

A Thesis Submitted to
the School of Graduate Studies in Partial Fulfillment
of the Requirements for the Degree
Master of Science

McMaster University
Hamilton, Ontario, Canada

September 2015

McMaster University MASTER OF SCIENCE (2015) Hamilton, ON (Chemical Biology)

TITLE: Dissecting the Determinants of cAMP Affinity in Protein Kinase A

AUTHOR: KODY JOHN MOLESCHI, B.Sc. (University of British Columbia)

SUPERVISOR: Professor Giuseppe Melacini

NUMBER OF PAGES: viii, 116

Abstract

cAMP receptors contain highly conserved cAMP binding pockets, in part responsible for allosteric activation, yet CBDs exhibit a wide array of cAMP binding affinities. While several cAMP:CBD crystallographic structures have been solved, they are insufficient to explain differences in cAMP:CBD affinities. We hypothesize that it is the position of the apo autoinhibitory equilibrium and/or a change in the state-specific association constants of the active and inactive CBD forms that are primarily responsible for modulating ~1000-fold difference in cAMP affinities. Interestingly, we discovered that PKARIα and HCN2 have comparable state-specific association constants, suggesting that the position of the apo autoinhibitory equilibrium is primarily responsible for the large difference in observed cAMP affinities in these systems. In addition, the individual components of the cAMP binding pocket (*i.e.* BBR, PBC, and lid) show functional variability across different CBDs. In RIα, both the BBR and lid are dispensable for high affinity cAMP binding, leaving the PBC as the key determinant of cAMP affinity. Interestingly, in addition the PBC:cAMP contact side-chains, non-contact side-chains are also important in modulating cAMP affinity (*ie.* L201 and Y205). Further dissection of the contributions arising from the apo pre-equilibrium and the cAMP binding pockets is required to better understand cAMP affinity and selectivity.

Acknowledgements

I am particularly indebted to my supervisor Dr. Giuseppe Melacini. Thank you for allowing me to pursue my scientific interests in your lab. Your constant feedback, patience, and support have helped me transition from an amateur scientist to a more independent researcher, and that has been greatly appreciated. Some specific words of wisdom that I take away: “delay, pulse, relax”, where bench-work is not all that different from an NMR pulse sequence. This quotation resonates well with me and I will continue to apply this analogy to future endeavours. I have been most fortunate to work with you throughout this scientific adventure – thank you.

The last two years were only made as enjoyable as they were due to fantastic colleagues. Special thanks to Madoka Akimoto, Mostafa Algamal, Stephen Boulton, Olivia Byun, Melanie Gloyd, Naeimeh Jafari, Maryam Sayadi, and Bryan VanSchouwen for helpful discussions, both scientific and leisurely, as well as the unyielding support for the rollercoaster ride that is grad school. I relished our talks over coffee and lunch, and the odd lab outing to sample some great food in the GTA.

I would also like to extend thanks to my committee members, Drs. Philip Britz-McKibbin and Alba Guarné. The progression of my project was dependent on your helpful suggestions and constructive criticisms.

Finally, thanks to my parents, Leah and Gord, to which none of this would have been possible without. Thank you for supporting my choice and location of study, as I am sure you would have preferred me closer to home, as well as covering some of the (beer) bills ☺. The phone calls home made BC seem a little closer.

Table of Contents

Chapter 3

Measurement of State-Specific Association Constants in Allosteric Sensors through Molecular Stapling and NMR

Chapter 4

The Importance of Non-Contact Side-Chains and Capping Residues in Tuning PKA-RIα cAMP Affinity

Chapter 5

Conclusions and Future Directions: PKA-RIα Signal Termination by Mammalian Phosphodiesterase 8A

List of Abbreviations and Symbols

δ	Chemical shift (ppm)
AC	Adenylate cyclase
AMP	Adenosine monophosphate
ATP	Adenosine triphosphate
BBR	Base binding region
cAMP	Adenosine 3',5'-cyclic monophosphate
CBD	cAMP-binding domain
cGMP	Guanosine 3',5'-cyclic monophosphate
CHESPA	Chemical shift projection analyses
CNG	Cyclic nucleotide gated ion channel
C-subunit	Catalytic subunit of PKA
D_2O	Deuterium oxide
DTT	Dithiothreitol
IC_{50}	Half-maximal concentration of inhibition
K_D	Equilibrium dissociation constant
K_a	Equilibrium association constant
EPAC	Exchange protein activated by cAMP
GEF	Guanine exchange factor
GPCR	G-protein coupled receptor
H-D	Hydrogen-deuterium exchange
HCN	Hyperpolarization-activated cyclic nucleotide-gated ion channel
HSQC	Heteronuclear single quantum coherence
NMR	Nuclear magnetic resonance
PBC	Phosphate binding cassette
PDE	Phosphodiesterase
PKA	Protein kinase A
RIα	Isoform Iα of regulatory subunit of PKA
STD	Saturation transfer difference
STR	Saturation transfer reference
TROSY	Transverse relaxation-optimized spectroscopy
WT	Wild type

Chapter 1

cAMP Signalling and cAMP-Binding Domains

1.1 Introduction

Cyclic adenosine monophosphate (cAMP) is a prevalent second messenger and is critical in eukaryotic signalling[1,2]. Signal propagation first begins with an extracellular stimulus which is then internalized by G protein coupled receptors (GPCR) to begin the cascade of signalling events in response to the external effector (Fig. 1). The GPCR is a heterotrimeric membrane protein containing seven trans-membrane helices, and the G-protein coupled to the trans-membrane domains is broken down into the G_α, G_β, and G_γ subunits[3]. When the GPCR is in an inactive state, *ie.* in the absence of any extracellular stimulus, guanine diphosphate (GDP) is bound to G_α, which is associated with both G_β and G_γ. Upon activation of the GPCR by an extracellular effector molecule, large conformation rearrangements take place to facilitate a change to a guanine nucleotide exchange factor (GEF) functional role, thereby exchanging the G_α-GDP to G_α-GTP. As a result, the G_α subunit dissociates from the remaining G-protein and activates another adjacent membrane protein, adenylate cyclase (AC). AC can then enzymatically alter intracellular adenosine triphosphate (ATP) to cAMP[4]. Due to cAMP's widespread usage in signalling, concentration of the second messenger are tightly controlled through AC activation as well as by phosphodiesterases (PDE), which hydrolyze the phosphodiester bond of cAMP to convert it to cyclic adenosine monophosphate (AMP)[5].

This importance of cAMP signalling is also highlighted by the number of proteins containing cAMP binding domains (CBD), with a number of different isoforms for each CBD[6]. For example, protein kinase A (PKA), exchange protein activated by cAMP (EPAC),

hyperpolarization cyclic nucleotide-gated ion channels (HCN), cyclic nucleotide gated (CNG) channels, and GAF (cGMP and/or cAMP dependent) domains within PDEs are all activated by cAMP binding. Interestingly, isoforms exist for each CBD: PKAR I/IIα and I/IIβ, EPAC 1-2, HCN 1-4, CNG, PDE10 (cAMP dependent), and PDE11 (cAMP and cGMP dependent)[5,7–9]. When AC activation is then coupled with PDE activity, in conjunction with compartmentalization of cAMP and subcellular localization of specific CBD isoforms[4], what results is an exquisitely fine-tuned and selective spatio-temporal intracellular response triggered by the original extracellular effector bound to the GPCR.

1.2 PKA as a Therapeutic Target

As the prototypical receptor for cAMP, PKA regulates the majority of cAMP-dependent responses in mammals[10]. This includes, but is not limited to, ion-channel gating within the heart, cell growth, differentiation, and memory[11–13]. For example, in response to epinephrine, PKA is activated to phosphorylate troponin I and phospholamban thereby altering the rhythmicity between cardiac muscle relaxation and contraction[14]. The diverse roles of PKA in cAMP eukaryotic cellular signalling imply that a wide variety of diseases emerges as a result of improper cAMP signal transduction by PKA. For instance, altered cAMP signalling is associated with acute ischemic stress, as well as dysfunctional binding between PKA and A kinase anchoring proteins (AKAP) has been linked to heart failure[15]. Several point mutations within the regulatory subunit of PKA have been linked to Carney complex and acrodysostosis, which are characterized by cardiac tumours and spotty skin pigmentation, and skeletal malformations and growth delays, respectively[16–20]. It has also been noted that improper PKA signalling is associated with hyperphosphorylation of the intrinsically disordered tau protein, resulting in

accumulation of potentially toxic tau and Aβ aggregates, one of the long-thought hallmarks of neurodegenerative disorders, such as Alzheimer's disease (AD)[21]. In addition, PKA's functional roles in cell growth and development have also made it an ideal drug target for cancer treatment[13]. However, due to the conserved CBD structural architecture, it is difficult to selectively target one CBD over another, and further research is required to better understand the molecular mechanisms underlying cAMP:CBD affinity and selectivity, as well as activation.

1.3 PKA-R Structural Overview and CBD Homology

The PKA holoenzyme exists as an inhibited tetrameric module containing a dimeric regulatory subunit (R), each bound to one catalytic subunit (C). Upon binding of two cAMP molecules, R undergoes large conformational changes to facilitate the release of C (Fig. 2)[22,23]. The C subunit is then free to phosphorylate downstream targets to continue signal transduction. The different R isoforms (*i.e.* RIα, RIIα, RIβ, and RIIβ) are non-redundant, and exhibit different, tissue-specific cAMP responses[24]. By far the most studied through biochemical and biophysical analysis is RIα. In this capacity, it has served as an essential allosteric model to dissect the underlying mechanistic contributions of dynamics in biological regulation.

1.3.1 Conformations of the Regulatory Subunit

The R-subunit is a dimeric inhibitory protein that serves to silence catalytic activity of C in a cAMP-dependent manner. Each R is comprised of two cAMP binding sites, denoted as CBD-A and CBD-B. In RIα, both sites exhibit very tight cAMP binding (K_D ~nM), with CBD-B occupied with cAMP first due to its lower cAMP K_D[25]. The binding of the cyclic nucleotide to CBD-B then primes CBD-A to also accept a cAMP molecule. Conformational rearrangement

occur for CBD-A to bind cAMP[23]. In this manner, the release of C is facilitated by the structural changes needed to accommodate cAMP. To better understand the mechanism of cAMP activation, crystals structures were sought for PKA-R in its different states.

Several well-defined, high resolution crystallographic X-ray structures have been solved for PKA-RIα in its end point conformations[22,23]. Static snapshots exist for fully inactive, C-subunit-bound R (H-state), as well as the fully active (B-state) cAMP-bound form sans C. Together these states of the R-subunit tightly control the catalytic activity of C, and therefore, secondary signalling by cAMP. The apo R (*i.e.* R-subunit in the absence of both C and cAMP) has been shown to dynamically sample both H and B-states[26].

The regulatory subunit prevents C-dependent catalysis through occlusion of the active site[22]. An N-terminal flexible linker found in R contains an inhibitory sequence (IS: Arg[94]-Arg-Gly-Ala-Ile[98]), which interacts with the catalytic cleft to prevent the uptake of substrate (Fig. 2). To further stabilize the inactive form, CBD-A also interact with the C-subunit[23]. Due to the complexity of the PKA-R:C holoenzyme, comprised of four subunits (2 x R, 2 x C) and four cAMP binding pocket (2 x CBD-A, 2 x CDB-B), totalling ~ 150 kDa, it is of great importance to simplify the system. Through a 'divide and conquer' strategy, more meaningful data can be collected and pieced together to dissect the determinants of cAMP-dependent allostery in PKA. This is normally performed by developing shorter, but still biologically relevant, constructs.

1.3.2 PKARIα (91-244) as a Simplified Model for Full Length R

A widely used, single nucleotide binding R-subunit of PKA Iα is the 91-244 segment (Fig 3). This shorter construct maintains the N-terminal linker which is inclusive of the IS. As a result, 91-244 is fully able to inhibit C in a cAMP-dependent manner due to the presence of CBD-A[26]. Crystallographic structures of the C- and cAMP-bound forms have also been solved

for this construct, with the resulting structures essentially identical to longer versions including CBD-B[27]. Dilute RIα 91-244 is monomeric as it lacks the dimerization-docking domain. Consequently, analyses are simplified as there is only one binding pocket (CBD-A) and accounting for binding contributions of CBD-B is no longer required. In addition, the molecular weight of the system is significantly reduced thereby simplifying NMR spectral analyses through fewer peak numbers and greater signal:noise for the remaining peaks due to increased molecular tumbling rates. Since the RIα 91-244 construct preserves biological relevance, while simplifying resulting analyses, RIα 91-244 was used in the majority of experiments discussed in this thesis.

1.3.3 CBD Homology and cAMP Affinity

The conserved CBD architecture has made the development of translational therapeutics challenging. CBDs are defined by three highly conserved structural elements: a phosphate binding cassette (PBC), a base binding region (BBR), which is part of the rigid β-subdomain, and a more dynamic α-subdomain capping helix known as the lid[6] (Fig. 4). The PBC makes direct polar and ionic contacts with the ribose and phosphate moieties within cAMP, whereas parts of the BBR and lid interact with the adenine base. While these features are mostly conserved, making selective CBD targeting inherently difficult, it still remains possible to exploit selectivity due to unique cAMP-CBD binding affinities.

Binding affinity is an important determinant of selectivity and varies considerably among CBDs. For instance, the observed cAMP affinities of PKA RIα (K_D ~nM) and of EPAC and HCN (K_D ~μM) are surprisingly different, despite their structural and sequence similarities (Table 1, Fig. 5)[25,26,28,29]. X-ray crystallographic structures exist for the aforementioned structurally homologous CBDs (Fig. 5), but alone they are not sufficient to fully explain these differences in cAMP affinities [22,30–32].

The cAMP binding pockets of RIα, HCN, and EPAC are structurally homologous, with little changes observed. There is some CBD heterogeneity at the level of the lid, but complete deletion does not cause order of magnitude changes in affinities[33]. Furthermore, the syn *vs.* anti cAMP orientation does not correlate with affinity. Both cAMP bound PKARIα and EPAC have syn cAMP orientations, but cAMP binds HCN in the anti-position[30,34]. To understand cAMP-selectivity, it is necessary to model affinities in the context of the full allosteric thermodynamic cycle, arising from the coupling of the auto-inhibitory inactive *vs.* active equilibrium and the cAMP-binding apo *vs.* holo equilibrium (Fig. 6)[26]. The holo-active CBD is just one of the four states in this thermodynamic cycle. The other states must be taken into account as well to understand cAMP affinity, because high affinity binding is exhibited by RIα for cAMP in the B-state, but not in the H-state[26].

The cAMP-affinity of CBDs is tuned by an apo autoinhibitory equilibrium that is responsible for buffering proteins between inactivation and activation by cAMP[36]. cAMP-free RIα exists in a dynamic equilibrium between inactivated C-subunit bound (~50%) and cAMP bound (~50%) forms, and their structures are illustrated in Fig. 7. As such, apo RIα is primed to maximally associate with C or cAMP. In contrast, this equilibrium is greatly shifted towards the inactive state in the case of apo HCN, with > 99% of the population being in the inactive form[36]. While apo RIα is minimally and transiently populated, as it is primarily bound to cAMP or the C-subunit, the inherent dynamics displayed by apo RIα is a key determinant in cAMP affinity.

1.4 Thesis Goals

1.4.1 Probing the Determinants of CBD:cAMP Affinity Differences

It is necessary to consider the apo populations of active *vs.* inactive states in conjunction with their state-specific affinities. Observed affinities are averages of state-specific association constants weighted by apo populations of the active and inactive states. As a result, we hypothesize that the differences in K_D values between PKA and HCN arise from differences at the level of state-specific association constants and/or of the apo populations of the active vs. inactive states.

We also wanted to dissect the individual contributions to cAMP affinity of the three conserved canonical cAMP binding sites (*ie.* BBR, PBC, and lid). While it is known that the defining elements of the cAMP binding pocket are the BBR, the PBC, and the lid, it still remains unclear how each specifically modulates cAMP affinity and selectivity. The PBC hydrogen bonds cAMP to anchor it within the binding pocket, while the lid of cAMP in CBD-A orchestrates inter-domain crosstalk between CBD-A and CBD-B but is not required to modulate cAMP affinity within PKA-RIα. It could be that that BBR facilitates the anti-to-syn base transition of cAMP through its stabilization of the adenine base, but further study is needed to test this hypothesis.

1.4.2 Open Questions and Objectives

While the crystal structures of the different conformations of PKA-R have been invaluable in modelling cAMP-dependent activation, they are only static snapshots and do not capture the dynamic processes underlying cAMP binding and CBD selectivity. As stated previously, the inherent dynamic nature of PKA RIα modulates cAMP affinity and the variable

components of observed affinities (*ie.* apo populations, state-specific K_a values), in conjunction with possibly dissimilar contributions of the cAMP binding sites, likely differentiate it from other CBDs.

Several questions remain unclear in the context of cAMP signalling and activation of CBDs. We wish to define the determinants of cAMP:CBD affinity (*ie.* PKA-R vs. HCN) using nuclear magnetic resonance (NMR) spectroscopy. It is known that these systems exist in active and inactive states to modulate biological activity and their apo populations and state-specific K_a values directly influence the observed cAMP affinity. As a result, we wish to trap the low-affinity inactive PKA-R state complexed with cAMP using designed molecular staples (*i.e.* disulfide bridges) to measure the state-specific association constants using nuclear magnetic resonance (NMR), and compare them to homologous CBDs.

The distinct roles of the three components of the cAMP binding pocket (BBR, PBC, and lid) are also under-evaluated in PKARIα. While it is known that the PBC is responsible for making direct cAMP contacts, as is common to all CBDs, the contributions of the BBR are unknown, and that of the lid remain controversial. For example, Trp260 of the lid region within PKA-R is said to gate and hydrophobically cap cAMP, expectedly influencing binding. However deletion of the lid region altogether does not affect cAMP affinity or base orientation. The BBR region is much more variable in sequence among CBDs, but also makes several CBD-conserved hydrophobic interactions with the adenine base of cAMP. Combination of these components regulates cAMP affinity and further study is required to dissect the individual roles. Affinity is a critical component of CBD selectivity and activation, and understanding the interplay between these overarching themes is expected to aid in the development of translational therapeutics.

1.4.3 Experimental Design

Previous attempts to extract state-specific association constants from PKA-R, mainly of the inactive cAMP-bound form, have made use of the C-subunit to stabilize the inactive form of R. However, direct polar contacts exist between the PBC of R and an adjacent C helix, altering cAMP affinity. To extract reliable state-specific association constants from the PKA system, the inactive conformation must be selected for without the C-subunit. This was performed by using designed molecular staples, in the form of disulfide bridges, where oxidation of proximal cysteine residues serves as a covalent thread to immobilize the inactive state. This is then coupled with NMR chemical shift analyses to gauge state populations as well as saturation transfer difference (STD) competition experiments to measure the resulting cAMP affinities. A different approach was used to assess individual cAMP binding pocket contributions. In an attempt to dissect further roles of the PBC and BBR within PKA-R, point mutations were engineered at particular positions of the cAMP binding pocket. This included an alanine scan of the PBC, where each non-alanine residue was mutated to alanine. In addition, hydrophobic BBR:cAMP contacts were also mutated to alanine. Each mutant was screened using STD cAMP and Sp-cAMPs to check for reduced ligand affinity.

1.5 Summary of Chapters

1.5.1 Chapter 1: Introduction to cAMP Signalling and cAMP Binding Domains

1.5.2 Chapter 2: Materials and Methods of Experimental Work

1.5.3 Chapter 3: Measurement of State-Specific Association Constants in Allosteric Sensors through Molecular Stapling and NMR

Allostery is a ubiquitous mechanism to control biological function and arises from the coupling of inhibitory and binding equilibria. The extent of coupling reflects the inactive *vs.* active state selectivity of the allosteric effector. Hence, dissecting allosteric determinants requires quantification of state-specific association constants. However, observed association constants are typically population-averages, reporting on overall affinities but not on allosteric coupling. Here we propose a general method to measure state-specific association constants in allosteric sensors based on three key elements, *i.e.* state-selective molecular stapling through disulphide bridges, competition binding saturation transfer experiments and chemical shift correlation analyses to gauge state populations. The proposed approach was applied to the prototypical cAMP-dependent protein kinase (PKA-RIα), for which the structures of the inactive and active states are available, as needed to design the state-selective disulphide bridges. Surprisingly, the PKA-RIα state-specific association constants are comparable to those of a structurally homologous domain with ~10^3-fold lower cAMP-affinity, suggesting that the affinity difference arises primarily from changes in the position of the dynamic apo inhibitory equilibrium.

1.5.4 Chapter 4: The Importance of Non-Contact Side-Chains and Capping Residues in Tuning PKARIα cAMP Affinity

Cyclic adenosine monophosphate (cAMP) selectivity is important for specific targeting of cAMP binding domains (CBDs), *i.e.* protein kinase A (PKA) selection over exchange protein activated by cAMP (EPAC) and hyperpolarization-activated cyclic nucleotide-gated ion channels (HCN) or vice versa. However, the underlying mechanism for selective CBD targeting remains

largely elusive. A critical factor in selectivity is binding affinity, which varies considerably among CBDs. Here we identified three PBC residues in RIα, two of which that form a solvent exposed hydrophobic stack between Leu^{201} and Tyr^{205}, and a C-terminal Ala^{211} hydrophobic cap. The resulting L201A and Y205A mutations significantly reduced cAMP affinity without perturbing the apo autoinhibitory equilibrium or introducing structural defects. The side chains of Leu^{201} and Tyr^{205} do not contact cAMP but their role in cAMP binding is rationalized by hydrophobic stacking at positions i, i + 4 of the PBC helix, which increases its overall stability. In this case the i, i + 4 stack is critical in maintaining cAMP affinity, which is not observed in EPAC or HCN PBCs. The C-terminal alanine residues of the PBC hydrophobically stabilize the adenine base and mutations to A211D and A211T are associated with CNC and acrodysostosis, respectively. Each mutant displayed decreased cAMP sensitivity (A211D K_D > 200 µM, A211T K_D ~5 µM), again without changing the position of the pre-equilibrium. The added steric bulk of Asp or Thr likely clashes with cAMP, resulting in decreased affinities.

1.5.5 Chapter 5: Conclusions and Future Directions: PKARIα Signal Termination by Mammalian Phosphodiesterase 8A

Another critical implication of the high affinity of cAMP for PKA RIα is that the lifetime of bound cAMP, which is inaccessible to PDEs, is longer than in other CBDs. Hence, it has been proposed[37] that cAMP signal termination requires the formation the binding of PDEs to PKA RIα and the active "extraction" of cAMP from PKA RIα. Recently, the RIα:PDE8A interaction has been mapped by HDXMS at peptide resolution, providing essential groundwork in understanding kinase signal termination by PDEs[37]. However, many outstanding questions still remain, which prompted further investigations into this interaction. Using transverse relaxation-optimized spectroscopy (TROSY), we were able to map the RIα:PDE8A interaction at atomic

resolution. NMR analyses yielded results consistent with those obtained at peptide resolution through HDXMS for the RIα:PDE8A binding interface. Residues within the cAMP binding pocket are perturbed in the presence of PDE8A, suggesting PDE-induced cAMP channelling. Furthermore, our preliminary data suggest that both CBD-A and CBD-B of RIα are channelled with similar time scales. It still remains unclear which RIα conformation PDE8A preferentially binds, and addressing this open question likely is facilitated by the use of methyl TROSY for direct observation of the RIα:PDE8A complex.

1.6 References

(1) Krebs, E. G. *Angew. Chemie Int. Ed. English* **1993**, *32*, 1122–1129.

(2) Daniel, P. B.; Walker, W. H.; Habener, J. F. *Annu. Rev. Nutr.* **1998**, *18*, 353–383.

(3) Neves, S. R.; Ram, P. T.; Iyengar, R. *Science* **2002**, *296*, 1636–1639.

(4) Scott, J. D. *Biochem. Soc. Trans.* **2006**, *34*, 465–467.

(5) Houslay, M. D.; Adams, D. R. *Biochem. J.* **2003**, *370*, 1–18.

(6) Rehmann, H.; Wittinghofer, A.; Bos, J. L. *Nat. Rev. Mol. Cell Biol.* **2007**, *8*, 63–73.

(7) Taylor, S. S.; Kim, C.; Cheng, C. Y.; Brown, S. H. J.; Wu, J.; Kannan, N. *Biochim. Biophys. Acta - Proteins Proteomics* **2008**, *1784*, 16–26.

(8) Herrmann, S.; Schnorr, S.; Ludwig, A. *Int. J. Mol. Sci.* **2015**, *16*, 1429–1447.

(9) Gloerich, M.; Bos, J. L. *Annu. Rev. Pharmacol. Toxicol.* **2010**, *50*, 355–375.

(10) Bos, J. L. *Trends Biochem. Sci.* **2006**, *31*, 680–686.

(11) Kuschel, M.; Zhou, Y. Y.; Cheng, H.; Zhang, S. J.; Chen, Y.; Lakatta, E. G.; Xiao, R. P. *J. Biol. Chem.* **1999**, *274*, 22048–22052.

(12) Lochner, A.; Genade, S.; Tromp, E.; Podzuweit, T.; Moolman, J. a. *Circulation* **1999**, *100*, 958–966.

(13) Cho-Chung, Y. S.; Pepe, S.; Clair, T.; Budillon, A.; Nesterova, M. *Crit. Rev. Oncol. Hematol.* **1995**, *21*, 33–61.

(14) Katz, a M.; Lorell, B. H. *Circulation* **2000**, *102*, IV69–V74.

(15) Zakhary, D. R.; Moravec, C. S.; Stewart, R. W.; Bond, M. *Circulation* **1999**, *99*, 505–510.

(16) Greene, E. L.; Horvath, A. D.; Nesterova, M.; Giatzakis, C.; Bossis, I.; Stratakis, C. a. *Hum. Mutat.* **2008**, *29*, 633–639.

(17) Horvath, A.; Bertherat, J.; Groussin, L.; Guillaud-Bataille, M.; Tsang, K.; Cazabat, L.; Libé, R.; Remmers, E.; René-Corail, F.; Faucz, F. R.; Clauser, E.; Calender, A.; Bertagna, X.; Carney, J. A.; Stratakis, C. a. *Hum. Mutat.* **2010**, *31*, 369–379.

(18) Cazabat, L.; Ragazzon, B.; Varin, A.; Potier-cartereau, M.; Vandier, C.; Vezzosi, D.; Risk-rabin, M.; Guellich, A.; Schittl, J.; Lechêne, P.; Richter, W.; Nikolaev, V. O.; Zhang, J.; Bertherat, J.; Vandecasteele, G. *Hum. Mol. Genet.* **2014**, *23*, 1163–1174.

(19) Bertherat, J.; Horvath, A.; Groussin, L.; Grabar, S.; Boikos, S.; Cazabat, L.; Libe, R.; René-Corail, F.; Stergiopoulos, S.; Bourdeau, I.; Bei, T.; Clauser, E.; Calender, A.; Kirschner, L. S.; Bertagna, X.; Carney, J. A.; Stratakis, C. a. *J. Clin. Endocrinol. Metab.* **2009**, *94*, 2085–2091.

(20) Kirschner, L. S.; Carney, J. a; Pack, S. D.; Taymans, S. E.; Giatzakis, C.; Cho, Y. S.; Cho-Chung, Y. S.; Stratakis, C. a. *Nat. Genet.* **2000**, *26*, 89–92.

(21) Su, Y.; Ryder, J.; Ni, B. *FEBS Lett.* **2003**, *546*, 407–410.

(22) Su, Y.; Dostmann, W. R.; Herberg, F. W.; Durick, K.; Xuong, N. H.; Ten Eyck, L.; Taylor, S. S.; Varughese, K. I. *Science* **1995**, *269*, 807–813.

(23) Kim, C.; Cheng, C. Y.; Saldanha, S. A.; Taylor, S. S. *Cell* **2007**, *130*, 1032–1043.

(24) Doskeland, S. O.; Maronde, E.; Gjertsen, B. T. *Biochimica et Biophysica Acta - Molecular Cell Research*. 1993, pp 249–258.

(25) Dostmann, W. R. G.; Taylor, S. S.; Genieser, H. G.; Jastorff, B.; Doskeland, S. O.; Ogreid, D. *J. Biol. Chem.* **1990**, *265*, 10484–10491.

(26) Akimoto, M.; Selvaratnam, R.; McNicholl, E. T.; Verma, G.; Taylor, S. S.; Melacini, G. *Proc. Natl. Acad. Sci. U. S. A.* **2013**, *110*, 14231–14236.

(27) Badireddy, S.; Yunfeng, G.; Ritchie, M.; Akamine, P.; Wu, J.; Kim, C. W.; Taylor, S. S.; Qingsong, L.; Swaminathan, K.; Anand, G. S. *Mol. Cell. Proteomics* **2011**, *10*, M110.004390.

(28) Lolicato, M.; Nardini, M.; Gazzarrini, S.; Moller, S.; Bertinetti, D.; Herberg, F. W.; Bolognesi, M.; Martin, H.; Fasolini, M.; Bertrand, J. a.; Arrigoni, C.; Thiel, G.; Moroni, A. *J. Biol. Chem.* **2011**, *286*, 44811–44820.

(29) Mazhab-Jafari, M. T.; Das, R.; Fotheringham, S. a.; SilDas, S.; Chowdhury, S.; Melacini, G. *J. Am. Chem. Soc.* **2007**, *129*, 14482–14492.

(30) Xu, X.; Vysotskaya, Z. V.; Liu, Q.; Zhou, L. *J. Biol. Chem.* **2010**, *285*, 37082–37091.

(31) Rehmann, H.; Schwede, F.; Doøskeland, S. O.; Wittinghofer, A.; Bos, J. L. *J. Biol. Chem.* **2003**, *278*, 38548–38556.

(32) Rehmann, H.; Arias-Palomo, E.; Hadders, M. a; Schwede, F.; Llorca, O.; Bos, J. L. *Nature* **2008**, *455*, 124–127.

(33) Zhou, L.; Siegelbaum, S. A. *Structure* **2007**, *15*, 655–670.

(34) Das, R.; Chowdhury, S.; Mazhab-Jafari, M. T.; SilDas, S.; Selvaratnam, R.; Melacini, G. *J. Biol. Chem.* **2009**, *284*, 23682–23696.

(35) Akimoto, M.; Zhang, Z.; Boulton, S.; Selvaratnam, R.; Van Schouwen, B.; Gloyd, M.; Accili, E. a.; Lange, O. F.; Melacini, G. *J. Biol. Chem.* **2014**, *289*, 22205–22220.

(36) Boulton, S.; Akimoto, M.; VanSchouwen, B.; Moleschi, K.; Selvaratnam, R.; Giri, R.; Melacini, G. *Biochem. Soc. Trans.* **2014**, *42*, 302–307.

(37) Krishnamurthy, S.; Moorthy, B. S.; Xin Xiang, L.; Xin Shan, L.; Bharatham, K.; Tulsian, N. K.; Mihalek, I.; Anand, G. S. *Biophys. J.* **2014**, *107*, 1426–1440.

Table 1. cAMP binding pocket sequence and affinity comparisons.

	Sequence		
Protein	BBR	PBC	Affinity
PKARIIβ	FDIYVKCD-GVGRCV	G**E**LALMYNTP**R**AA	0.9 nM
PKARIα	MDVYVNNE-WA-TSV	G**E**LALIYGTP**R**AA	4 nM
HCN4	VSVLTKGN-KE-TKL	G**E**ICLLTRGR**RT**A	0.8 μM
EPAC2	VNVVIYGKGVV-CTL	GKLALVNDAP**R**AA	1 μM
EPAC1	VNVVTHGKGLV-TTL	GQLALVNDAPRAA	3 μM
HCN2	VSVLTKGN-KE-MKL	G**E**ICLLTRGR**RT**A	3.6 μM

Hydrophobic contact, **side-chain H-bond**, backbone H-bond

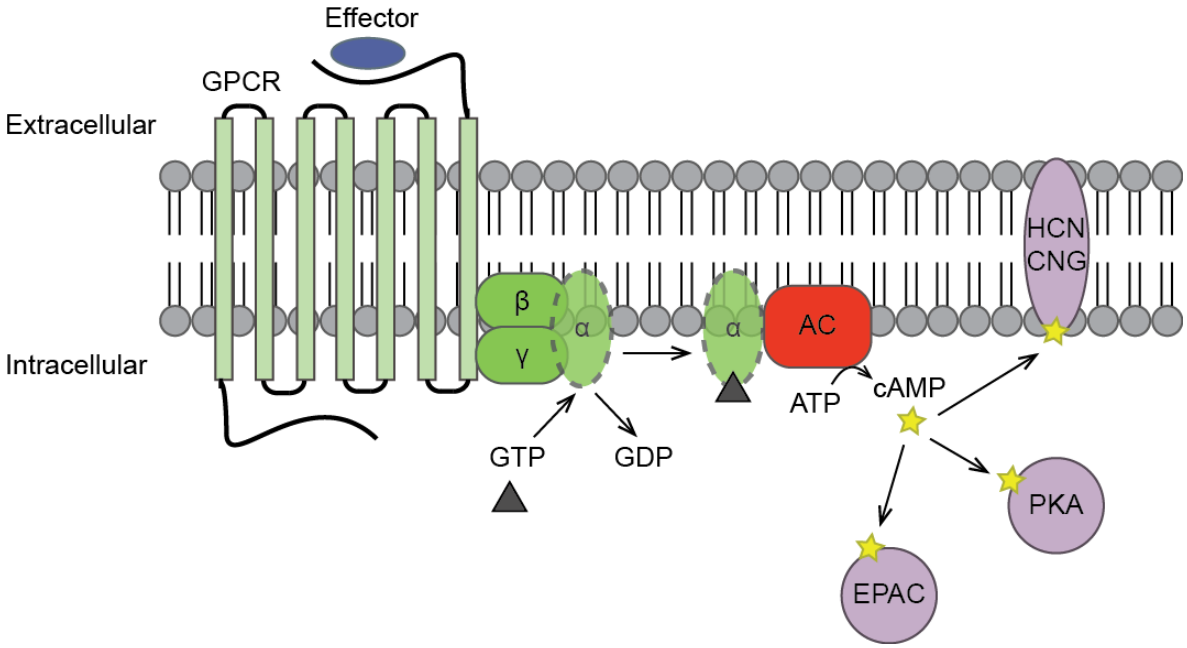

Figure 1. General signalling and CBD activation scheme. General process on converting an extracellular stimulus to an internalized response with cAMP as a second. An extracellular effector molecule first binds the GPCR, causing the associated G_{β} and G_{γ} subunits to undergo conformational changes. This facilitates the replacement GDP-bound G_{α} with GTP, thereby activating AC. The active AC can then convert local ATP into cAMP, resulting in the activation of downstream cAMP receptors.

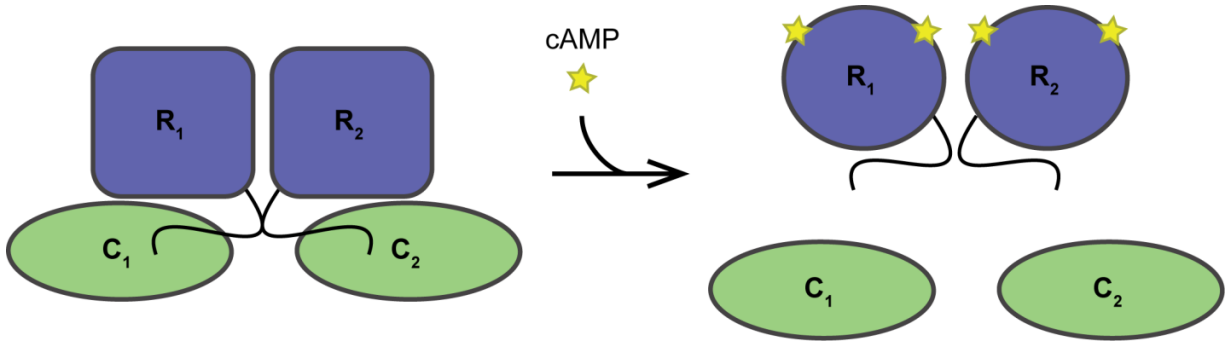

Figure 2. Tetrameric PKA domain organization. The regulatory subunits (R) are dimeric and inhibitory by nature, and each bind one catalytic subunit (C) to silence its activity. Once two cAMP molecules bind each subunit, large conformational rearrangements take place to release C. As such, the active kinase is available to phosphorylate downstream targets.

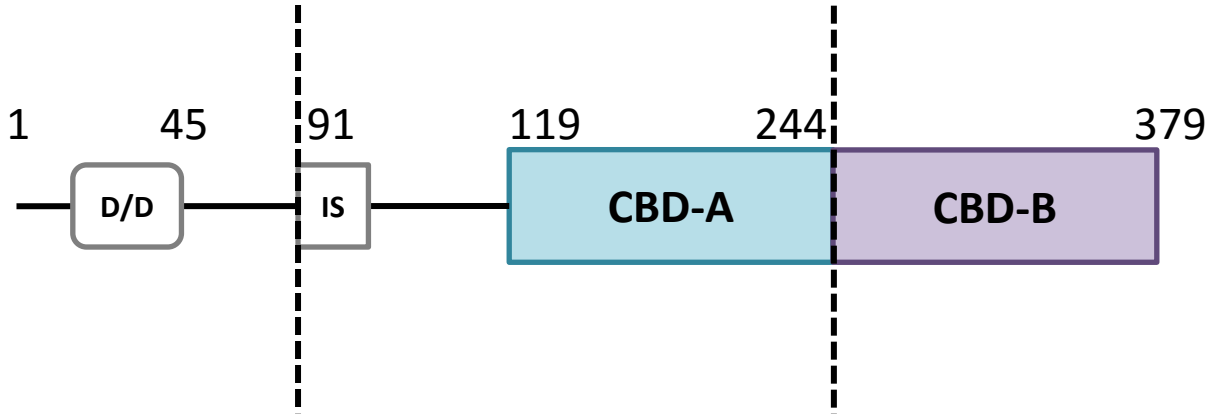

Figure 3. Monomeric PKA RIα domain organization. Full length PKA RIα is comprised of residues 1-379, spanning the dimerizing/docking domain (D/D), inhibitory sequence (IS), as well as CBD-A and CBD-B. The construct used for the majority of experiments spans residues 91-244 and includes the IS for C-subunit binding and the single cAMP binding unit CBD-A.

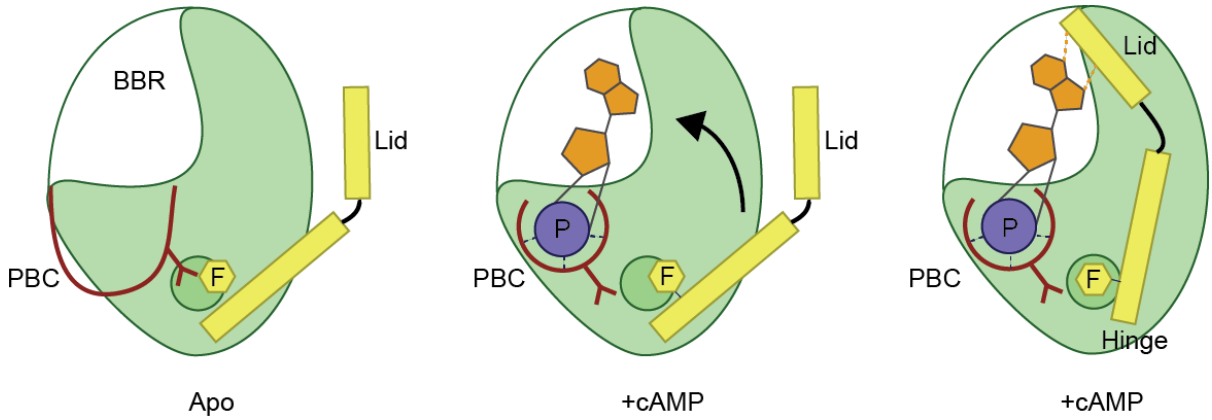

Figure 4. Conserved CBD architecture. All CBDs are composed of a rigid β-subdomain (green), which is inclusive of the BBR and PBC. In the apo form, the pocket is relatively open and ready to accept cAMP. The PBC hydrogen bonds the phosphate and ribose moieties of cAMP, while the BBR stacks against the adenine base. Once anchored, the dynamic α-subdomain (light yellow), referred to as the lid, moves into place near cAMP, typically by a hydrophobic hinge mechanism Adapted from Rehmann *et al*[6].

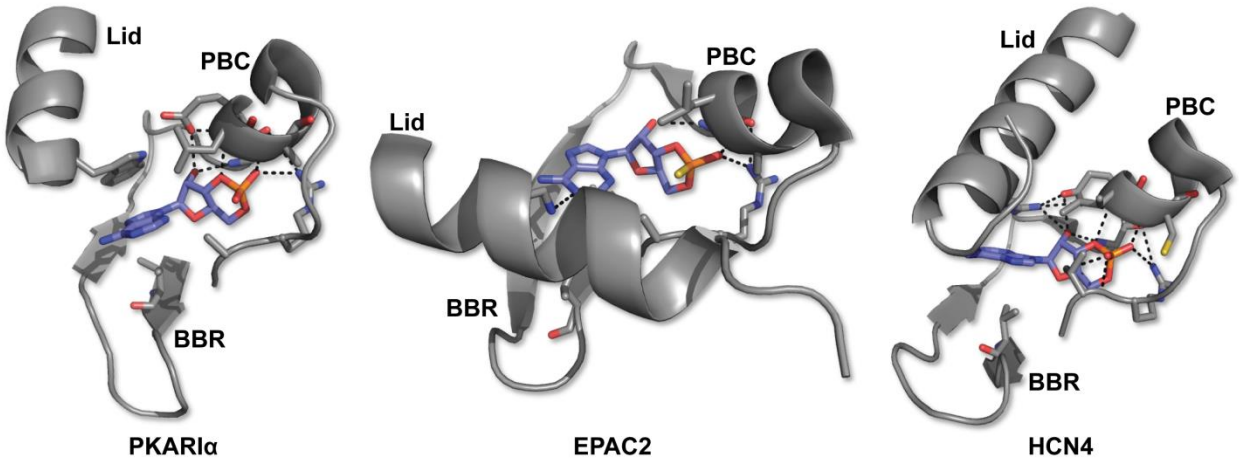

Figure 5. cAMP-bound crystal structures PKA RIα, EPAC2, and HCN4. The cAMP binding pocket is shown for each cAMP-bound CBD; base binding region (BBR), phosphate binding cassette (PBC), and the capping lid helix. cAMP is shown as blue and orange sticks. PDB accession codes are as follows: PKA RIα (1RGS), EPAC2 (3CF6), HCN4 (3OTF).

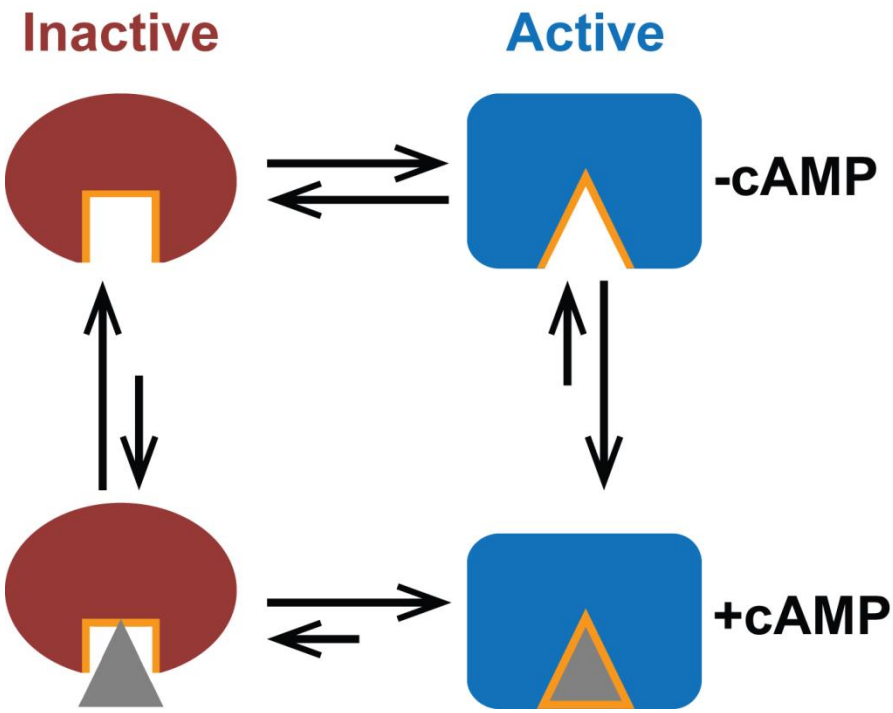

Figure 6. PKARIα thermodynamic allosteric cycle. Apo RIα equally samples inactive (red) and active (blue) states. The inactive state exhibits high affinity for the catalytic subunit, while the active state preferentially interacts with cAMP. Arrows indicate the favourable interactions. The cAMP binding pocket is shown in orange, while cAMP is illustrated by the gray triangle.

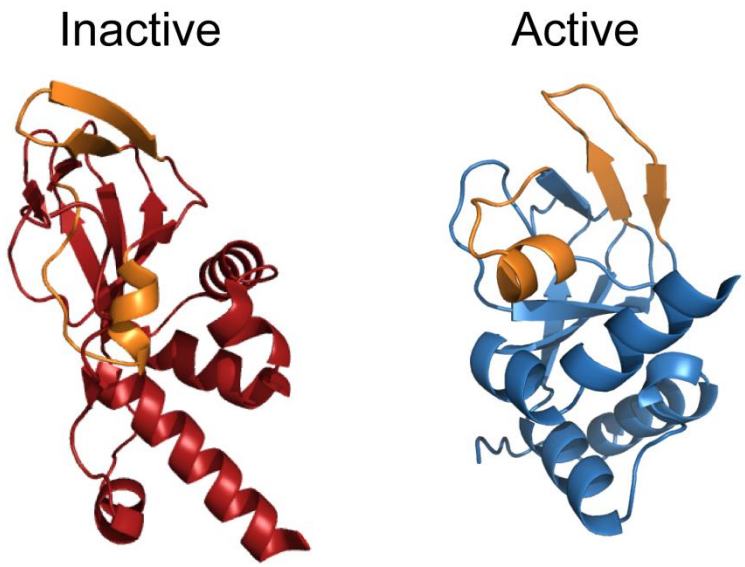

Figure 7. Endpoint conformations of RIα. Distinct structural rearrangements occur, depending on the presence of the C-subunit or cAMP. The inactive form (red) is poised to bind C, while the active conformation (blue) selectively interacts with cAMP. cAMP binding pocket is in orange.

Chapter 2

Materials and Methods

2.1 Cloning and Site-directed Mutagenesis

All mutations were generated using a variation of the Quikchange™ protocol. For a point mutation to be generated, changes were made at the level of ~20-30mer oligonucleotide primers with the mutation occurring in the middle on both complementary strands. Care was taken to minimize the number of altered nucleotides to facilitate the desired translated mutation and to use *E. coli* optimized codons. Polymerase chain reactions (PCR) consisted of 0.6 µL forward and reverse primers (10 µM) with the desired mutation, 0.5 µL template WT PKARIα cDNA (~10ng/ µL), 1 µL dimethylsulfoxide (DMSO, 5% v/v), 7.3 µL sterile DH_2O, and 10 µL KOD Hotstart master mix, totalling 20 µL. The PCR cycle is as follows: initial denaturation 5 min at 95 °C, cycled denaturation of 50 s at 95 °C, annealing for 50 s at 65 °C, and extension for 7 min at 68 °C, which was cycled 18 times. A final extension of 7 min at 68 °C was applied after the last cycle.

2.2 Expression and Purification of PKARIα (91-244)

All mutations were generated using a variation of the Quikchange protocol. pRSET plasmid encoding the small ubiquitin-like modifier (SUMO)-PKA fusion protein was transformed into BL-21 (DE3) *Escherichia coli.* Mature colonies were picked and used to inoculate 10 mL or 100 mL of Luria broth (LB), for isotopically labelled and unlabelled samples, respectively. All cultures were incubated for ~18 h at 37 °C, shaking at 200 rpm. For unlabelled

cultures, the 100 mL culture was transferred to 1 L LB. In the case of cultures enriched with $^{15}NH_4Cl$, the 10 mL culture was transferred to 100 mL M9 media, incubated overnight, and then transferred to 1 L of M9. Protein expression was induced with 0.5 mM IPTG once an OD_{600} of 0.7-0.8 was reached. Upon induction, cultures were placed in an 18 °C incubator for ~18 h. Cells were harvested by centrifugation at 7000 rpm for 20 min. Cell pellets were stored at -80 °C for future use.

Frozen cell pellets were thawed on ice and resuspended in lysis/wash buffer (50 mM MOPS pH 7.4, 500 mM NaCl, 20 mM imidazole, 5 mM 2-mercaptoethanol). Resuspended cells were then supplemented with protease inhibitors (final concentrations of 10mM benzamidine, 0.4 mM AEBSF, 1 µM pepstatin, 1 µM leupeptin, 28 µM TPCK and TLCK). Lysis was achieved by sonication (1 min sonicating, followed by 1 min resting on ice, repeated 3-4 times). Lysate was then centrifuged at 14000 rpm for 1 h at 4 °C. The soluble fraction was passed through a 0.45 µm filter then applied to a Ni^{2+} affinity resin immobilized within a gravity column (GE). The insoluble portion was resuspended in urea-containing wash buffer (50 mM MOPS pH 7.4, 500 mM NaCl, 20 mM imidazole, 5 mM 2-mercaptoethanol, 8 M urea) and centrifuged as before. This fraction was applied separately to the Ni^{2+} resin.

Unfolding and washing occurred simultaneously. The protein was washed with 10 mL of urea-containing wash buffer (50 mM MOPS pH 7.4, 500 mM NaCl, 20 mM imidazole, 5 mM 2-mercaptoethanol, 8 M urea). Since endogenous bacterial cAMP is found to co-purify with PKA, this step is critical in obtaining the apo form. Elution of the unfolded protein was then carried out with 15-20 mL elution buffer (50 mM MOPS pH 7.4, 500 mM NaCl, 5 mM 2-mercaptoethanol, 300 mM imidazole, 8 M urea). The protein was placed in dialysis tubing (3500 MWCO, Thermo

Scientific) with 0.5 mg in-house-purified TEV protease and then into 4 L of dialysis buffer (50 mM MOPS pH 7.4, 100 mM NaCl, 5 mM 2-mercaptoethanol) at room temperature overnight.

The dialyzed protein was then run on the Ni^{2+} resin for a second time to remove both cleaved and uncleaved His_6-SUMO solubility tag, as well as His_6-TEV protease. Centrifugal filter columns (Amicon) were used to concentrate the protein in preparation for SEC (Superdex 75, GE) to remove any misfolded, soluble aggregates.

2.3 Disulphide State Trapping

The disulphide bridged proteins were kept reduced at every step of the preparation protocol until samples were ready for spectroscopic studies. Extensive dialysis (4 x 1 L for ~2 h followed by 1 x 4 L overnight at room temperature) was then utilized for buffer-exchange into the NMR buffer (50 mM MOPS pH 7, 100 mM NaCl, 10 mM $MgCl_2$, 0.02% NaN_3) and oxidation of the cysteines. It should be noted that no cysteines are native to PKARIα (91-244). Mutants were then concentrated with centrifugal filters (10 kDa MWCO, Millipore) to 100 µM and supplemented with 5% D_2O for locking purposes. In the case of reduced samples, 5 mM DTT was added and incubated for 1 h at room temperature. The mutant sample integrity was checked by both SEC chromatography (Superdex 75 or 200, GE) and NMR. No significant differences were observed between the elution volumes of the mutants and the WT in the absence of DTT, indicating that the cysteine mutations did not result in the formation of soluble aggregates. In addition, the NMR signal-to-noise ratios in the HSQC spectra of the mutants and WT were comparable further ruling out potential mutation-induced aggregates/oligomers.

2.4 Inhibition Kinase Assay

RIα (91-244) at different concentrations (10^{-2} nM – 4.68 x 10^{3} nM) was incubated with the catalytic subunit (4 nM) at room temperature for 10 min in the assay buffer (40mM Tris-HCl pH 7.5, 0.1 mg/mL BSA, and 20 mM $MgCl_2$), as previously described[40]. Two assay reagents, 10 µM Kemptide and 10 µM ATP, were then added to the assay buffer to reach a total volume of 50 µL and to start the phosphorylation reactions. Reactions were allowed to proceed for 60 min after which 50 µL of Ultra-Glo luciferase solution were added. Two controls were also prepared, consisting of a reaction with no Kemptide to provide the maximal luminescence, and another reaction with only RIα absent to obtain the minimal luminescence. Luminescence was measured with a TECAN infinite M200 plate reader.

2.5 NMR Measurements

Uniformly ^{15}N-labeled proteins were concentrated to 100 µM and supplemented with both 5% D_2O for locking, and ^{15}N-acetyl glycine for referencing. For the holo samples, cAMP was added at a total concentration of 1 mM. Sensitivity enhanced heteronuclear single quantum coherence (HSQC) spectra were acquired for all samples in apo and excess +cAMP forms, both with or without DTT, on a Bruker AV 700 spectrometer equipped with a TCI cryogenic probe. Spectra included 256 (t_1) and 1024 (t_2) complex points over spectral widths of 31.82 and 14.06 ppm for the ^{15}N and ^{1}H dimensions, respectively, and were recorded with 4 scans and a 1.70 s recycle delay. Carrier frequencies of ^{1}H and ^{15}N were set at the water and central amide region, respectively. All spectra were recorded at 306 K and processed using NMRpipe[58] with linear prediction. Spectra were analyzed utilizing Sparky[59] and Gaussian line-fitting. Resonance

assignments were established through spectral comparisons with WT RIα (91-244). The combined ^{15}N and ^{1}H chemical shifts were computed as:

$$\Delta\delta = [(\Delta\delta_{1H})^2 + (0.2\Delta\delta_{15N})^2]^{1/2} \quad (4)$$

and a chemical shift cut-off of 0.05 ppm was implemented for the CHESPA analyses (Supplementary Material)[48,49]. The apo and cAMP-bound wild-type forms served as the CHESPA reference states to evaluate the effect of the perturbed state, *i.e.* the apo or cAMP-bound mutant. The fractional activation and cos(θ) values were calculated as previously described[49].

2.6 STD Experiments and Competition Binding Measurements

Purified RIα (91-244) mutants at a concentration of 10 μM were buffer exchanged into 20 mM NaH_2PO_4 pH 6.5, 50 mM NaCl in ≥ 99% D_2O using disposable PD-10 desalting columns (GE) or centrifugal Zeba filters (Thermo Scientific). Reference (STR), difference (STD) ^{1}H spectra with water-gate water suppression were acquired for all samples at 298 K. Off-resonance saturation occurred at 30 ppm, while on-resonance irradiation was placed at 0.79 ppm. This ensured selective irradiation of the protein and not the ligand. A short spin-lock of 5 ms was applied to minimize protein signal interference, while also avoiding reduction in ligand signals. Spectra were digitized with 16 K complex points. The spectral width was 13.03 ppm centered at 4.71 ppm, with 1024 or 512 scans and 8 dummy scans for the STD experiments. For the more sensitive STR experiments, 128 scans were used.

Dissociation constants for the disulphide mutants with cGMP and cAMP were measured by quantifying the fraction of protein bound (<ν>) through the normalized STD amplification

factor (STD_{af}) method[50]. Ligand concentrations varied between 10 µM to 320 µM. In the case of competition experiments, samples were pre-saturated with 500 µM cGMP, and then titrated with increasing amounts of cAMP. Upon addition of cAMP, the sample was incubated at room temperature for 30 min to ensure complete ligand equilibration prior to NMR data acquisition. STD_{af} was determined from the product of the STD:STR ratio, measured for the ^{1}H1' cAMP ribose, and the ratio of total ligand and protein concentration[50]. The STD_{af} values were normalized to the largest STD_{af} to obtain the fraction of protein bound (<ν>):

$$<\nu> = \frac{STD_{af}}{STD_{af,max}} \qquad (5)$$

The experimental <ν> values were then modeled according to the 1:1 binding isotherm:

$$<\nu> = \frac{[L]}{K_D + [L]} \qquad (6)$$

where [L] is the concentration of free cAMP or cGMP and K_D denotes either the K_{Dapp} for cAMP or the actual K_D for cGMP. [L] was obtained from $[L]_{Total}$ by subtracting the concentration of bound ligand:

$$[L] = [L]_{Total} - (<\nu>[P]_{Total}) \qquad (7)$$

Both cGMP K_D and cAMP K_{Dapp} values were determined using Scatchard plots (<ν>/[L] *vs.* <ν>) by computing the negative reciprocal of the slope. The K_{Dapp} values for cAMP were converted to $K_{D,Obs}$ through the Supplementary equation S18.

2.7 Urea Unfolding Monitored by Tryptophan Fluorescence

Purified apo RIα (91-244) was mixed with either 100-fold excess cAMP, then incubated with increasing concentrations of urea (0-8 M) in the assay buffer (50 mM MOPS pH 7, 100 mM NaCl, 10 mM $MgCl_2$) for 3 h at room temperature. Measurements were performed with a TECAN infinite M200 plate reader. Samples were excited at 293 nm and the emissions recorded at 340 nm and 353 nm. The shift in wavelength due to unfolding of CBD-A was monitored using fluorescence intensity ratios (353/340 nm). The resulting unfolding curves were constructed using $X_U = (R_{obs} – R_N)/(R_U – R_N)$, where X_U is the fraction unfolded of the protein and R_{obs} represents the observed ratio of intensity at particular urea concentrations. The fully folded and unfolded states are R_N and R_U, respectively. Free energies of unfolding (ΔG) were calculated using a two-state model: $\Delta G_{unfolding} = -RTln(X_U/X_N)$, where $X_N + X_U = 1$, and X_N is the fraction of folded protein. The free energy of unfolding without denaturants, $\Delta G^{H}2^{O}$, was calculated using $\Delta G = \Delta G^{H}2^{O} + m[Urea]$.

Chapter 3

Measurement of State-Specific Association Constants in Allosteric Sensors through Molecular Stapling and NMR

3.1 Preface

The work outlined in this chapter was accepted and published in the *Journal of the American Chemical Society*. It may be cited as:

Moleschi, K J., Akimoto, M and Melacini, G. Measurement of State-Specific Association Constants in Allosteric Sensors through Molecular Stapling and NMR. *J. Am. Chem. Soc.* **2015**, 137, 10777-10785.

All experimental work was performed by K. Moleschi with invaluable aid in experimental design from M. Akimoto and Dr. G. Melacini. The manuscript was co-written by K. Moleschi and Dr. G. Melacini and approved by all authors.

3.2 Introduction

Allosteric regulation is a fundamental control mechanism of biological systems[1–23] and it has opened new opportunities to design antagonists and agonists with enhanced potency and selectivity for therapeutic targets previously considered undruggable[24–28]. A simple, but effective model to understand allostery elicited by a generic ligand relies on the four-state thermodynamic cycle arising from the coupling of two equilibria: the inhibitory (*i.e.* inactive *vs.* active) equilibrium and the ligand-binding (*i.e.* apo *vs.* holo) equilibrium (Fig. 1a)[3,29–34]. If the ligand does not exhibit active *vs.* inactive selectivity, the binding and inhibitory equilibria are not coupled and binding occurs without activation or further inhibition (*i.e.* antagonism). If the ligand exhibits active *vs.* inactive selectivity, ligand binding stabilizes the state with the highest affinity, leading to an allosteric conformational change (*i.e.* agonism or reverse-agonism). In general, the binding and inhibitory equilibria are allosterically coupled with a coupling free energy equivalent to:

$$\Delta G_{Allosteric\ Coupling} = RT\ ln\left(\frac{K_{a,Inactive}}{K_{a,Active}}\right) \qquad (1)$$

where $K_{a,Inactive}$ and $K_{a,Active}$ denote the association constants of the ligand for the inactive and active states of the allosteric protein, respectively. For agonists $K_{a,Inactive} < K_{a,Active}$, while for reverse-agonists $K_{a,Inactive} > K_{a,Active}$. Hence, measurements of state-specific association constants are essential for dissecting the driving forces underlying allosteric agonism and antagonism. However, currently available methods to measure affinities[35] focus primarily on the quantification of ensemble average association constants only. The observed average affinities are easily computed through binding polynomials (Supplementary Material) based on the allosteric cycle of Fig. 1a, showing that:

$$K_{a,Observed} = X_{Inactive,Apo}\, K_{a,Inactive} + X_{Active,Apo}\, K_{a,Active} \qquad (2)$$

where $X_{Inactive,Apo}$ and $X_{Active,Apo}$ denote the fractions of inactive and active states, respectively, in the absence of ligand. Equation (2) illustrates how the observed average affinities depend on both the position of the apo inhibitory equilibrium and the state-specific association constants. Even when the former is known, measurement of $K_{a,Observed}$ is not sufficient to determine the latter.

Here, we propose a general experimental approach to determine state-specific association constants. This can be achieved through traditional affinity measurements if the apo form of the allosteric system is trapped in either the pure inactive or active states. In principle, an efficient trapping method is provided by state-specific disulphide bridges, referred to here as 'molecular staples'. However, in practice, disulphide bridges alone rarely result in the isolation of pure states. Often molecular stapling simply provides a conformational bias towards the inactive or active states. Nevertheless, we show that the conformational bias provided by molecular stapling is sufficient to determine state-specific association constants, if it is combined with (*a*) measurements of the positions of the perturbed inhibitory equilibria based on NMR chemical shifts and (*b*) with competition binding experiments monitored by Saturation Transfer Difference (STD) NMR spectra. When linear patterns of peak positions are observed in the disulphide-stapled mutant, the combination of conformational stapling through disulphide bridges, NMR chemical shift analyses, and competitive STD experiments results in a general approach for the measurement of state-specific association constants in allosteric regulators.

The proposed method to measure state-specific association constants is illustrated through its application to the regulatory subunit of the cAMP-dependent protein kinase A (PKA

RIα), which represents a prototypical allosteric signalling system[36–41]. The central controlling unit of PKA RIα comprises the (91-244) region, which includes the kinase inhibitory site and a single cAMP-binding domain (CBD) as well as the linker connecting them (Fig. 1b)[42]. RIα (91-244) fully inhibits the PKA catalytic subunit (C) in a cAMP-dependent manner and binds both cAMP and C with affinities comparable to full length RIα[40,43]. Although cAMP-binding to RIα (91-244) is slow in the NMR chemical shift time scale (at 700 MHz), the inactive vs. active exchange is fast in both apo and holo forms[36,40] and therefore measurement of state-specific affinities would be challenging without modification of RIα (91-244). Our results show that the state-specific association constants measured for RIα (91-244) using molecular stapling and NMR are comparable to those measured for another eukaryotic CBD, which binds cAMP with an affinity ~three orders of magnitude weaker than that of RIα (91-244). The surprising similarity in state specific association constants between these two CBDs suggests that the marked difference in their overall affinities arises primarily from changes in the position of the respective apo inhibitory equilibria.

3.3 Results

3.3.1 Design of state-selective molecular staples

The structures of RIα (91-244) bound to either cAMP (*i.e.* active state) or C (*i.e.* inactive state) have been solved[44–46] and based on these structures we identified potential residue pairs to be used as sites for double mutations to cysteine. Such residue pairs meet two key conditions: (*i*) they are not part of the binding sites for the allosteric ligand to avoid affecting its affinity; (*ii*) they are close in the state to be stabilized by the disulphide bridge (*e.g.* C^{β}-C^{β} < 6 Å), but farther apart in the other (*e.g.* C^{β}-C^{β} > 8 Å). Two residue pairs that meet these criteria in RIα (91-244)

are A108/M234 and E143/S236 (Fig. 1c,d). These residue pairs are distal from the sites in contact with cAMP, *i.e.* the phosphate binding cassette and the base binding region (Fig. 1c,d) and correspond to short distances in the inactive (*e.g.* C^{β}-C^{β} < 6 Å), but not in the active state (Fig. 1c,d), suggesting that disulphide bridges at these locations should stabilize the inactive state. Hence, the two double cysteine mutants A108C/M234C and E143C/S236C were engineered and the resulting disulphide bridged constructs were assessed for their shifts in inhibitory equilibrium using a combination of kinase assays and NMR chemical shift analyses.

3.3.2 The designed disulphide mutants partially stabilize the inactive state of the apo form

For both A108C/M234C and E143C/S236C double mutants of PKA-RIα (91-244), kinase inhibition assays were performed in which luminescence measurements report on the amount of residual ATP. Higher luminescence values indicate higher concentrations of ATP and thus lower the activities of the catalytic subunit of PKA (PKA-C), as shown in Fig. 1e,f. Panels 1e,f illustrate that both disulphide mutants of RIα (91-244) inhibit PKA-C more effectively than wild type (WT) RIα (91-244). The IC_{50} values for A108C/M234C (0.8 nM) and E143C/S236C (0.9 nM) are similar, and at least one order of magnitude lower than that of WT (29 nM). The decreased IC_{50} values in the mutants *vs.* WT confirm that the designed disulphide bridges successfully increase the fraction of inactive-state conformations, which exhibit high affinity for the catalytic subunit of PKA.

In order to quantify the increase in the inactive population resulting from the disulphide bridges, we took advantage of recently proposed NMR methods based on chemical shift projection and correlation analyses[47–49]. For this purpose, HSQC spectra were collected for A108C/M234C and E143C/S236C RIα (91-244) both in the absence of cAMP and in the

presence of saturating cAMP concentrations and compared to similar reference spectra acquired for WT RIα (91-244) in the apo, cAMP- and C-bound forms (Fig. 2a-d). The apo, cAMP- and C-bound HSQC WT peak positions of residues that are sufficiently removed from both cAMP- and C-binding interfaces (*e.g.* L221) define linear patterns (Fig. 2a-d), indicating that such residues report primarily on the fast-exchanging active *vs.* inactive equilibrium. Due to the population-weighted averaging occurring in the fast exchange regime, the active *vs.* inactive fractions are encoded directly in the measured NMR chemical shifts. For instance, the WT apo peak is approximately equidistant from the WT RIα:cAMP and WT RIα:C peaks (Fig. 2a), indicating that in WT apo the populations of the active and inactive states are similar, as determined previously[40]. However, for the A108C/M234C disulphide bridged mutant the apo peak (green) is shifted towards the WT RIα:C (purple) position (Fig. 2a), pointing to an increase in inactive state population relative to WT.

As a negative control to confirm that the increase in inactive state population is caused by the 108/234 disulphide bridge, HSQC spectra for the A108C/M234C mutant were also acquired in the presence of the reducing agent dithiothreitol (DTT) (red, Fig. 2a). If inactive state immobilization relies on the molecular staple, it is expected that the spectra of the disulphide bridge mutants would be DTT dependent. When DTT is added to the sample, a partial reversion towards WT apo is observed (Fig. 2a). It is possible that full reversion to WT apo is not observed because the reduced cysteine residues slightly perturb the inactive *vs.* active equilibrium even prior to disulphide bridge formation and/or partial re-oxidation occurs prior to data acquisition. In either case, the lack of full reversion to WT does not affect the measurement of state-specific association constants and Fig. 2a clearly shows that the 108/234 disulphide bridge is effective in selectively stabilizing the inactive state of apo RIα (91-244), as sensed by the selected L221

reporter residue. In order to evaluate to what extent the 108/234 disulphide bridge perturbs the inhibitory equilibrium of cAMP-bound RIα (91-244), similar experiments were repeated in the presence of excess cAMP (Fig. 2b).

3.3.3 The designed disulphide mutants partially stabilize the inactive state of the holo form

Figure 2b shows that the 108/234 disulphide bridge is effective in selectively stabilizing the inactive conformation over that of the active state of RIα (91-244), even in the presence of the endogenous allosteric activator, cAMP. As expected based on the disulphide bridge design criteria, under reducing conditions, the selective stabilization of the inactive state is markedly reduced (red, Fig. 2b). Similar results are obtained for the L221 reporter residue of the other independent mutant E143C/S236C in both apo and cAMP-bound forms (Fig. 2c,d). In order to prove that the inactive *vs.* active state stabilization imparted by the disulphide bridges is not dependent on the specific choice of L221 as a reporter residue for the inhibitory equilibrium (Fig. 2a-d), we also measured the changes in the fractions of inactive state by NMR chemical shifts (δ) correlation analyses (Fig. 2e,g).

Figure 2e,g shows the plot of ($\delta_{Mutant,Apo} - \delta_{WT,Holo}$) *vs.* ($\delta_{WT,Apo} - \delta_{WT,Holo}$). This plot is expected to be linear with a slope equal to $\frac{X_{Inactive,Mutant\ Apo}}{X_{Inactive,WT\ Apo}}$, *i.e.* the ratio between the fractions of inactive state in the mutant apo *vs.* WT apo, provided it is restricted to residues that sense primarily the position of the inhibitory equilibrium (Supplementary Material: residue selection criteria (a-c) p. S4 and equation S17)[49]. The resulting plot for the apo A108C/M234C mutant is shown in Fig. 2e providing a $\frac{X_{Inactive,Mutant\ Apo}}{X_{Inactive,WT\ Apo}}$ ratio of 1.32 ± 0.05, *i.e.* the 108/234 disulphide bridge leads to an overall ~30% increase in the apo inactive population.

A similar approach was utilized to quantify the change in inactive fraction of the holo form. The plot of ($\delta_{Mutant,Holo} - \delta_{WT,Holo}$) *vs.* ($\delta_{Mutant,Apo} - \delta_{WT,Holo}$) for residues reporting on the inhibitory equilibrium is expected to be linear with a slope equal to the $\frac{X_{Inactive,Mutant\ Holo}}{X_{Inactive,Mutant\ Apo}}$ ratio (Supplementary Material: equation S14), which in the case of the A108C/M234C mutant is 0.83 ± 0.04 (Fig. 2f). This result means that unlike WT, the 108/234 disulphide mutant limits the decrease in inactive fraction upon cAMP saturation to just ~15%. Similar results were obtained for the E143C/S236C mutant (Fig. 2g,h). Overall, the data of Fig. 2 clearly indicate that each independent disulphide bridge successfully shifts the inhibitory equilibrium of RIα (91-244) towards the inactive state in both apo and cAMP-bound forms, but residual populations of active state remain in both forms of the disulphide bridged mutants. Given the higher-affinity of cAMP for the active *vs.* inactive state, it is essential to account for the presence of residual active state populations when using the disulphide bridges as molecular staples for determining the association constant of the inactive state. This approach is preferred to other methods introducing additional, potentially invasive perturbations to further stabilize the inactive conformation.

3.3.4 Accounting for residual active state populations

The effect of the residual active state population in the disulphide-bridged mutants designed to trap the inactive state is corrected through the following equation (Supplementary Material):

$$K_{a,Inactive} = K_{a,Observed} \frac{X_{Inactive,Holo}}{X_{Inactive,Apo}} \quad (3)$$

where $X_{Inactive,Holo}$ denotes the fraction of inactive state in the presence of saturating amounts of ligand (*i.e.* large cAMP excess) and the other terms are defined as in equation (2). In principle

equation (3) applies to both WT and mutant proteins, however in the case of WT, the $X_{Inactive,Holo}$ term is often minimal (~0%) and typically affected by a high relative error. Due to the challenges in accurately determining $X_{Inactive,WT\ Holo}$, equation (3) is of little practical utility for the WT protein. However, when equation (3) is applied to the disulphide mutants designed to stabilize the inactive state, $X_{Inactive,Mutant\ Holo}$ is significantly higher than 0% (*e.g.* > 0.5 based on Fig. 2b,d,f,h) and is determined more accurately, making equation (3) an excellent tool to determine state-specific association constants. It should be noted that equation (3) was derived here for the inactive state as this is the state stabilized by the designed molecular staples used here, but a similar equation applies for the active state as well (Supplementary Material: equation S9) and it is useful when the molecular staples selectively stabilize the active state. The implementation of equation (3) requires the determination of $K_{a,Observed}$ and of the $\frac{X_{Inactive,Holo}}{X_{Inactive,Apo}}$ ratio for the mutants. The latter is measured directly through the slope of the ($\delta_{Mutant,Holo} - \delta_{WT,Holo}$) *vs.* ($\delta_{Mutant,Apo} - \delta_{WT,Holo}$) plots shown in Fig. 2f,h. Hence, the last measurement needed to obtain $K_{a,Inactive}$ from equation (3) is that of $K_{a,Observed}$.

3.3.5 Measurement of $K_{a,Observed}$ for the disulphide mutants

Saturation transfer difference (STD) NMR spectroscopy is a robust label-free method to quantify affinities, but the STD signal is typically weak for tightly bound complexes (K_D < ~μM)[50]. This was the case for cAMP binding to the disulphide mutants due to the presence of residual populations of active state, which exhibits high affinity for cAMP and leads to a marginal STD signal for cAMP (Supplementary Fig. S3). To circumvent this problem and widen the K_D window of applicability of the STD measurement, competition-binding experiments were performed with cyclic guanosine monophosphate (cGMP). cGMP binds PKA RIα at the same

site as cAMP but more weakly, resulting in a detectable STD signal for cGMP (Supplementary Fig. S3). This is because the addition of the cGMP amino group at position C2 of the guanine base clashes with the phosphate binding cassette, thereby exhibiting lower affinity[39]. Furthermore, several ^{1}H NMR signals of cGMP are well resolved from those of cAMP (*e.g.* ^{1}H1', Supplementary Fig. S3). Due to these properties, in the presence of cGMP it is possible to measure an STD signal for cAMP, which is utilized to monitor the competitive binding of cAMP to a mutant sample pre-loaded with an excess of cGMP, as shown in Fig. 3c,d. The apparent K_D ($K_{Dapp,Obs}$) obtained from the cAMP *vs.* cGMP competitive binding experiment (Fig. 3c,d) is then scaled down to the actual $K_{D,Obs}$ for cAMP using Supplementary equation S18 (Supplementary Material) and the STD-derived K_D for cGMP (Fig. 3a,b).

3.3.6 Determining the state-specific association constants

The resulting K_D for cGMP as well as the $K_{D,apparent}$ and $K_{D,Observed}$ for cAMP binding to both disulphide mutants are summarized in Table 1. The observed cAMP K_D values for A108C/M234C and E143C/S236C are 0.30 ± 0.1 µM and 0.16 ± 0.03 µM, respectively (Table 1). However, these observed dissociation constants are not the inactive-state specific K_D values, as they must first be corrected for the holo/apo inactive populations according to equation (3). Using the $\frac{X_{Inactive,Holo}}{X_{Inactive,Apo}}$ ratios from the slope of the chemical shift plots (Fig. 2f,h) to scale down according to equation (3) the $K_{D,Observed}$ from the STD competition experiments, the inactive-state specific K_D values are obtained, *i.e.* $K_{D,Inactive} = 0.36 \pm 0.12$ µM and 0.20 ± 0.04 µM for A108C/M234C and E143C/S236C, respectively (Table 1). Although these two dissociation constants were measured for two independent and distinct inactive-state trapping disulphide mutants, their difference is not significant, corroborating the robustness of the proposed approach

and suggesting that the values obtained from the two disulphide bridges can be combined into a single average inactive-state specific K_D (*i.e.* $1/K_{a,Inactive}$) value of 0.28 ± 0.06 μM for PKA-RIα (91-244) (Table 1).

Once the $K_{a,Inactive}$ is determined, the active-state specific K_a (*i.e.* $K_{a,Active}$) is obtained through equation (2) using the known $K_{a,Observed}$ and the inactive *vs.* active molar fractions measured for apo WT[40]. The resulting $K_{D,Active}$ value (*i.e.* 0.5 ± 0.1 nM, Table 1) is at least three-order of magnitude lower than the $K_{D,Inactive}$. Since $K_{a,Active} >> K_{a,Inactive}$, the term in $K_{a,Active}$ in equation (2) dominates the average, demonstrating that it would have been challenging to determine the $K_{a,Inactive}$ without the aid of inactive-state selective molecular staples (*e.g.* disulphide bridges).

3.4 Discussion

Using the proposed protocol, which combines molecular stapling with both ligand- and protein-based NMR as summarized in Fig. 5, we have determined that the $K_{D,Inactive}$ and $K_{D,Active}$ state-specific dissociation constants for the PKA-RIα (91-244):cAMP complex are in the sub-μM and ~nM ranges, respectively (Table 1). These values correspond to a ΔG of allosteric coupling of ~ -6 RT (equation 1), which is sufficient to reach active state populations > 90% when RIα is cAMP-bound[40]. Furthermore, the sub-μM and ~nM ranges for the $K_{D,Inactive}$ and $K_{D,Active}$ state-specific dissociation constants of PKA-RIα (91-244) compare well with those independently measured for a structurally homologous domain, *i.e.* the CBD of the hyperpolarization and cyclic-nucleotide gated (HCN) ion channels (Table 1)[51,52]. Unlike other cAMP-regulated signalling systems, the open *vs.* closed states of the HCN channel can be

selectively stabilized independently of cAMP by voltage alone and therefore the open *vs.* closed dissociation constants are accessible through patch clamp electrophysiology[51]. To the extent that the open/closed states of the HCN channel represent the active/inactive states of the HCN CBD, the currently available active and inactive dissociations constants for the CBD of HCN2 fall in the sub-μM and nM range[51,52], respectively, similarly to those independently measured here for PKA-RIα (91-244) using molecular stapling (Table 1).

The similarity in state-specific association constants between the CBDs of HCN and PKA is remarkable because HCN and PKA bind cAMP with markedly different affinities. While HCN2 exhibits a μM affinity for cAMP, PKA-RIα binds cAMP with an observed K_D in the nM range [40,53,54]. Considering that the observed affinities are averages, as shown by equation (2), the similarity in the state-specific association constants between HCN and PKA implies that the ~three-order of magnitude difference in cAMP affinities arises primarily from changes in the position of the apo inhibitory equilibrium (Fig. 4). This prediction is confirmed by recent investigations showing that the HCN inactive *vs.* active apo populations are significantly different, *i.e.* the apo HCN auto-inhibitory equilibrium is highly skewed towards the inactive (low-affinity) state[53], unlike apo PKA RIα (91-244) for which the inactive *vs.* active populations are comparable (Fig. 4)[40]. Overall, our measurements reveal that the CBD state-specific association constants are largely CBD-independent, suggesting the possibility that differences in cAMP-affinities between CBDs are to a large extent dictated by the dynamics of the apo CBDs rather than by the structures of the holo CBDs, which appear to be largely conserved across different eukaryotic CBDs[55]. While this principle was proven here only for two CBDs of HCN and PKA, it highlights the critical role of differential dynamics in determining binding selectivity.

The sub-μM value determined for $K_{D,Inactive}$ through the proposed molecular stapling approach (Table 1) is lower than the dissociation constant for cAMP binding to the C-bound RIα (91-244), which was previously determined to fall in the ~3-100 μM range[40,46,56]. The reduced cAMP-affinity of the R:C complex compared to the inactive state of the *apo* R-subunit is explained by the direct contacts between the C-subunit of PKA and the PBC of PKA-RIα (91-244), which in turn weaken the interactions between cAMP and the PBC[57]. These observations illustrate that a reliable measurement of state-specific association constants for PKA-R requires that the inactive state of PKA-R be selectively stabilized in the absence of PKA-C.

In conclusion, we have proposed and applied a general method to measure state-specific association constants of allosteric sensors based on three key elements, *i.e.* molecular stapling through disulphide bridges, competition binding STD experiments and chemical shift correlation analyses (Fig. 5). The disulphide "staples" are designed to exploit active *vs.* inactive structural differences and stabilize selected conformational states in both apo and holo forms. As it is often difficult to achieve full immobilization of the selected state, we also developed an approach to account for residual populations of alternative states through equation (3), which requires the measurements of both the mutant association constant and the state-specific populations. The former is effectively obtained through STD competition experiments, which provide a label-free access to a wide-window of association constants and are applicable to large MW systems. The latter are derived from chemical shift correlation and projection analyses[47,49]. Equation (3) is applied to different "stapled" mutants, which serve as reciprocal controls and provide multiple determinations of state specific association constants. The convergence of these independent measurements to a consensus set of state specific association constants supports the non-invasive nature of the designed molecular staples.

While the proposed approach was illustrated here for PKA RIα, the method is general and transferrable to other allosteric sensors, offering otherwise elusive insight on the determinants of binding affinities and of allosteric coupling (*i.e.* equations 1 and 2). For example, through the approach outlined here (Fig. 5) it was possible to address a long outstanding question about the ~three-order of magnitude higher affinity of PKA-RIα relative to other structurally homologous cAMP-binding domains (*e.g.* HCN). This apparent paradox was solved by showing that the state-specific association constants of the cAMP-binding domains of PKA-RIα and HCN are surprisingly similar, but the positions of their apo dynamic inhibitory equilibria are markedly different. These observations clearly illustrate that the dynamics of the apo forms is a critical determinant of affinities. Furthermore, the measurement of $K_{a,Inactive}$ provides a first level of characterization of the holo-inactive intermediate state complex (Fig. 1a), which is often only transiently populated but critical to facilitate the design of allosteric inhibitors.

3.5 Acknowledgements

We thank S. Boulton, N. Jafari, Dr. S.S. Taylor, Dr. C.G. Kalodimos, Dr. A. Guarné and M. Gloyd for helpful discussion. This work was supported by the Canadian Institutes of Health Research (CIHR) and the Natural Sciences and Engineering Research Council of Canada (NSERC). This manuscript is dedicated to the memory of our friend and colleague, Dr. Veronica Esposito (1974-2013).

3.6 References

1. Kuriyan, J. & Eisenberg, D. The origin of protein interactions and allostery in colocalization. *Nature* **450,** 983–990 (2007).

2. Ruschak, a M. & Kay, L. E. Proteasome allostery as a population shift between interchanging conformers. *Proc Natl Acad Sci U S A* **109,** E3454–62 (2012).

3. Vendruscolo, M. Protein regulation: the statistical theory of allostery. *Nat. Chem. Biol.* **7,** 411–412 (2011).

4. Changeux, J.-P. & Edelstein, S. J. Allosteric mechanisms of signal transduction. *Science* **308,** 1424–1428 (2005).

5. Gardino, A. K. *et al.* Transient Non-native Hydrogen Bonds Promote Activation of a Signaling Protein. *Cell* **139,** 1109–1118 (2009).

6. Kern, D. & Zuiderweg, E. R. P. The role of dynamics in allosteric regulation. *Curr. Opin. Struct. Biol.* **13,** 748–757 (2003).

7. Aghazadeh, B., Lowry, W. E., Huang, X. Y. & Rosen, M. K. Structural basis for relief of autoinhibition of the Dbl homology domain of proto-oncogene Vav by tyrosine phosphorylation. *Cell* **102,** 625–633 (2000).

8. Long, D. & Brüschweiler, R. Atomistic kinetic model for population shift and allostery in biomolecules. *J. Am. Chem. Soc.* **133,** 18999–19005 (2011).

9. Smock, R. G. & Gierasch, L. M. Sending signals dynamically. *Science* **324,** 198–203 (2009).

10. Tzeng, S.-R. & Kalodimos, C. G. Dynamic activation of an allosteric regulatory protein. *Nature* **462,** 368–372 (2009).

11. Boehr, D. D., Nussinov, R. & Wright, P. E. The role of dynamic conformational ensembles in biomolecular recognition. *Nat. Chem. Biol.* **5,** 789–796 (2009).

12. Hayashi, I., Wilde, A., Mal, T. K. & Ikura, M. Structural basis for the activation of microtubule assembly by the EB1 and p150Glued complex. *Mol. Cell* **19,** 449–460 (2005).

13. Religa, T. L., Sprangers, R. & Kay, L. E. Dynamic regulation of archaeal proteasome gate opening as studied by TROSY NMR. *Science* **328,** 98–102 (2010).

14. Kim, J. *et al.* Dysfunctional conformational dynamics of protein kinase A induced by a lethal mutant of phospholamban hinder phosphorylation. *Proc. Natl. Acad. Sci.* 201502299 (2015). doi:10.1073/pnas.1502299112

15. Ishiyama, N. *et al.* Dynamic and Static Interactions between p120 Catenin and E-Cadherin Regulate the Stability of Cell-Cell Adhesion. *Cell* **141,** 117–128 (2010).

16. Whittier, S. K., Hengge, A. C. & Loria, J. P. Conformational motions regulate phosphoryl transfer in related protein tyrosine phosphatases. *Science* **341,** 899–903 (2013).

17. Masterson, L. R. *et al.* CAMP-dependent protein kinase A selects the excited state of the membrane substrate phospholamban. *J. Mol. Biol.* **412,** 155–164 (2011).

18. Srivastava, A. K. *et al.* Synchronous Opening and Closing Motions Are Essential for cAMP-Dependent Protein Kinase A Signaling. *Structure* **22,** 1735–1743 (2014).

19. VanSchouwen, B., Akimoto, M., Sayadi, M., Fogolari, F. & Melacini, G. Role of Dynamics in the Autoinhibition and Activation of the Hyperpolarization-activated Cyclic Nucleotide-modulated (HCN) Ion Channels. *J. Biol. Chem.* **290,** 17642–54 (2015).

20. Smith, M. J. & Ikura, M. Integrated RAS signaling defined by parallel NMR detection of effectors and regulators. *Nat. Chem. Biol.* **10,** 223–30 (2014).

21. Mazhab-Jafari, M. T. *et al.* Understanding cAMP-dependent allostery by NMR spectroscopy: Comparative analysis of the EPAC1 cAMP-binding domain in its apo and cAMP-bound states. *J. Am. Chem. Soc.* **129,** 14482–14492 (2007).

22. Jayaraman, B. & Nicholson, L. K. Thermodynamic dissection of the ezrin FERM/CERMAD interface. *Biochemistry* **46,** 12174–12189 (2007).

23. Blyuss, K. B. & Nicholson, L. B. The role of tunable activation thresholds in the dynamics of autoimmunity. *J. Theor. Biol.* **308,** 45–55 (2012).

24. Courilleau, D. *et al.* Identification of a tetrahydroquinoline analog as a pharmacological inhibitor of the cAMP-binding protein Epac. *J. Biol. Chem.* **287,** 44192–44202 (2012).

25. Courilleau, D., Bouyssou, P., Fischmeister, R., Lezoualc'h, F. & Blondeau, J. P. The (R)-enantiomer of CE3F4 is a preferential inhibitor of human exchange protein directly activated by cyclic AMP isoform 1 (Epac1). *Biochem. Biophys. Res. Commun.* **440,** 433–448 (2013).

26. Nussinov, R. & Tsai, C. J. Unraveling structural mechanisms of allosteric drug action. *Trends Pharmacol. Sci.* **35,** 256–264 (2014).

27. Tzeng, S.-R. & Kalodimos, C. G. Allosteric inhibition through suppression of transient conformational states. *Nat. Chem. Biol.* **9,** 462–5 (2013).

28. Das, R. & Melacini, G. A model for agonism and antagonism in an ancient and ubiquitous cAMP-binding domain. *J. Biol. Chem.* **282,** 581–593 (2007).

29. Nussinov, R., Ma, B. & Tsai, C. J. Multiple conformational selection and induced fit events take place in allosteric propagation. *Biophys. Chem.* **186,** 22–30 (2014).

30. Tzeng, S.-R. & Kalodimos, C. G. Protein activity regulation by conformational entropy. *Nature* **488,** 236–240 (2012).

31. De, S. *et al.* Complete thermodynamic and kinetic characterization of the isomer-specific interaction between Pin1-WW domain and the amyloid precursor protein cytoplasmic tail phosphorylated at Thr668. *Biochemistry* **51,** 8583–8596 (2012).

32. Baldwin, A. J. & Kay, L. E. Structural biology: Dynamic binding. *Nature* **488,** 165–166 (2012).

33. Selvaratnam, R., Chowdhury, S., VanSchouwen, B. & Melacini, G. Mapping allostery through the covariance analysis of NMR chemical shifts. *Proc. Natl. Acad. Sci. U. S. A.* **108,** 6133–6138 (2011).

34. Boulton, S., Akimoto, M., Selvaratnam, R., Bashiri, A. & Melacini, G. A Tool Set to Map Allosteric Networks through the NMR Chemical Shift Covariance Analysis. *Sci. Rep.* **4,** 7306 (2014).

35. Pollard, T. D. A guide to simple and informative binding assays. *Mol. Biol. Cell* **21,** 4061–4067 (2010).

36. Das, R. *et al.* cAMP activation of PKA defines an ancient signaling mechanism. *Proc. Natl. Acad. Sci. U. S. A.* **104,** 93–98 (2007).

37. McNicholl, E. T., Das, R., SilDas, S., Taylor, S. S. & Melacini, G. Communication between tandem cAMP binding domains in the regulatory subunit of protein kinase A-Ialpha as revealed by domain-silencing mutations. *J. Biol. Chem.* **285,** 15523–15537 (2010).

38. Sjoberg, T. J., Kornev, A. P. & Taylor, S. S. Dissecting the cAMP-inducible allosteric switch in protein kinase a RIalpha. *Protein Sci.* **19,** 1213–1221 (2010).

39. Das, R. *et al.* Dynamically driven ligand selectivity in cyclic nucleotide binding domains. *J. Biol. Chem.* **284,** 23682–23696 (2009).

40. Akimoto, M. *et al.* Signaling through dynamic linkers as revealed by PKA. *Proc. Natl. Acad. Sci. U. S. A.* **110,** 14231–6 (2013).

41. Das, R. *et al.* Entropy-driven cAMP-dependent allosteric control of inhibitory interactions in exchange proteins directly activated by cAMP. *J. Biol. Chem.* **283,** 19691–19703 (2008).

42. Huang, L. J. S. & Taylor, S. S. Dissecting cAMP binding domain A in the RIalpha subunit of cAMP-dependent protein kinase: Distinct subsites for recognition of cAMP and the catalytic subunit. *J. Biol. Chem.* **273,** 26739–26746 (1998).

43. Herberg, F. W., Taylor, S. S. & Dostmann, W. R. G. Active site mutations define the pathway for the cooperative activation of cAMP-dependent protein kinase. *Biochemistry* **35,** 2934–2942 (1996).

44. Su, Y. *et al.* Regulatory subunit of protein kinase A: structure of deletion mutant with cAMP binding domains. *Science* **269,** 807–813 (1995).

45. Kim, C., Cheng, C. Y., Saldanha, S. A. & Taylor, S. S. PKA-I Holoenzyme Structure Reveals a Mechanism for cAMP-Dependent Activation. *Cell* **130,** 1032–1043 (2007).

46. Badireddy, S. *et al.* Cyclic AMP analog blocks kinase activation by stabilizing inactive conformation: conformational selection highlights a new concept in allosteric inhibitor design. *Mol. Cell. Proteomics* **10,** M110.004390 (2011).

47. Lorieau, J. L., Louis, J. M., Schwieters, C. D. & Bax, A. pH-triggered, activated-state conformations of the influenza hemagglutinin fusion peptide revealed by NMR. *Proc. Natl. Acad. Sci. U. S. A.* **109,** 19994–9 (2012).

48. Selvaratnam, R., Mazhab-Jafari, M. T., Das, R. & Melacini, G. The Auto-Inhibitory Role of the EPAC Hinge Helix as Mapped by NMR. *PLoS One* **7,** 1–9 (2012).

49. Selvaratnam, R. *et al.* The projection analysis of NMR chemical shifts reveals extended EPAC autoinhibition determinants. *Biophys. J.* **102,** 630–639 (2012).

50. Stockman, B. J. & Dalvit, C. NMR screening techniques in drug discovery and drug design. *Prog. Nucl. Magn. Reson. Spectrosc.* **41,** 187–231 (2002).

51. Boulton, S. *et al.* Tapping the translation potential of cAMP signalling: molecular basis for selectivity in cAMP agonism and antagonism as revealed by NMR. *Biochem. Soc. Trans.* **42,** 302–307 (2014).

52. Zhou, L. & Siegelbaum, S. A. Gating of HCN Channels by Cyclic Nucleotides: Residue Contacts that Underlie Ligand Binding, Selectivity, and Efficacy. *Structure* **15,** 655–670 (2007).

53. Akimoto, M. *et al.* A mechanism for the auto-inhibition of hyperpolarization-activated cyclic nucleotide-gated (HCN) channel opening and its relief by cAMP. *J. Biol. Chem.* **289,** 22205–22220 (2014).

54. Lolicato, M. *et al.* Tetramerization dynamics of C-terminal domain underlies isoform-specific cAMP gating in hyperpolarization-activated cyclic nucleotide-gated channels. *J. Biol. Chem.* **286,** 44811–44820 (2011).

55. Rehmann, H., Wittinghofer, A. & Bos, J. L. Capturing cyclic nucleotides in action: snapshots from crystallographic studies. *Nat. Rev. Mol. Cell Biol.* **8,** 63–73 (2007).

56. Khanh, K. D. *et al.* Epac1 and cAMP-dependent protein kinase holoenzyme have similar cAMP affinity, but their cAMP domains have distinct structural features and cyclic nucleotide recognition. *J. Biol. Chem.* **281,** 21500–21511 (2006).

57. Kim, C., Xuong, N.-H. & Taylor, S. S. Crystal structure of a complex between the catalytic and regulatory (RIalpha) subunits of PKA. *Science* **307,** 690–696 (2005).

Table 1. Summary of Observed and State-Specific K_D Values

cAMP-Binding Domain (CBD)	cGMP K_D (μM)	cAMP K_{Dapp} (μM)	cAMP $K_{D,Obs}$ (μM)[a]	$\frac{X_{In,Holo}}{X_{In,Apo}}$	cAMP $K_{D,In}$ (μM)	cAMP $K_{D,Ac}$ (μM)
A108C/M234C RIα (91-244)	16.9 ± 6.1	9.1 ± 1.3	0.30 ± 0.10	0.83 ± 0.04	0.36 ± 0.12	--
E143C/S236C RIα (91-244)	2.4 ± 0.4	32.2 ± 2.0	0.16 ± 0.03	0.81 ± 0.05	0.20 ± 0.04	--
WT RIα (91-244)	--	--	$(1.0 \pm 0.1)10^{-3}$[a]	--	0.28 ± 0.06[b]	$(0.5 \pm 0.1)10^{-3}$
WT HCN2	--	--	3.6 ± 1.3[c]	--	0.84[d]	$(8.0)10^{-3}$[d]

[a]From Ref.[40]. [b]Average $K_{D,inactive}$ between disulphide mutants. [c]From Ref.[54]. [d]From Ref.[52]

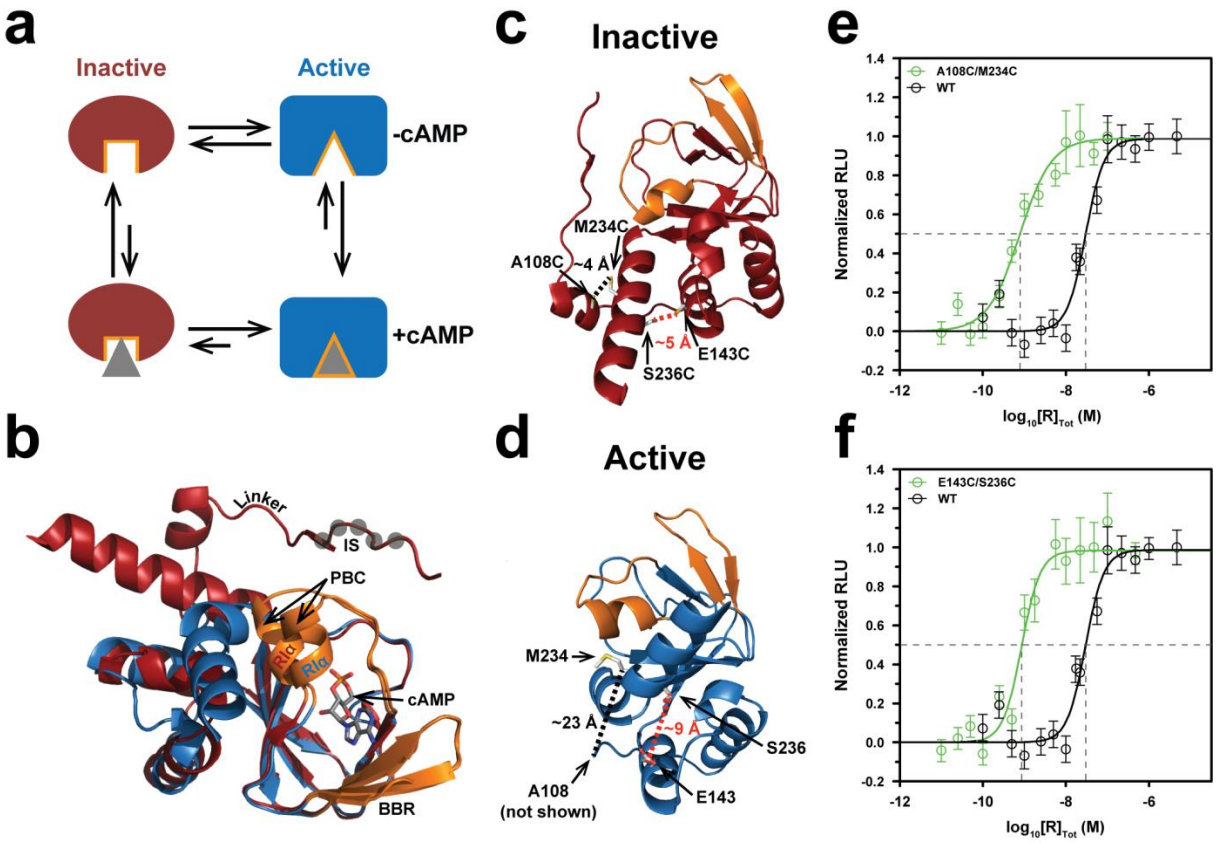

Figure 1. Allosteric thermodynamic cycle and state-selective trapping through molecular staples in PKA-RIα. (**a**) Apo RIα (91-244) samples both the active (blue) and inactive (red) states. The catalytic subunit of PKA preferentially binds the inactive state, while cAMP (gray) exhibits higher affinity for the active state. Weak cross-state interactions do exist, but little information is available due to the inherent dynamics of RIα. The cAMP binding pocket is shown in orange. (**b**) Overlay of the inactive (PDB: 2QCS) and active (PDB: 1RGS) structures[44–46]. Color codes are as in panel (a). Gray circles indicate the residues in the kinase inhibitory site. (**c, d**) Design of molecular staples to stabilize the inactive state of RIα (91-244). Specific residue pairs were mutated to cysteine for the purpose of disulphide bridge formation and stabilization of the inactive state. Residue pairs suitable for mutations are outside the cAMP binding pocket (orange) and exhibit C^{β}-C^{β} distances (dotted lines) < 6 Å in the inactive state but > 8 Å in the active state. The A108/M234 and E143/S236 residue pairs met these criteria and were selected for state-specific trapping. (**e**) Luminescence monitored kinase inhibition assay for A108C/M234C. Increasing amounts of RIα (91-244) were added to the PKA C-subunit to silence its catalytic activity. Increasing relative luminescence units (RLU) indicate enhanced inhibition. Significantly less disulphide-bridged RIα (green, IC_{50} = 0.8 nM) was required to inhibit C, as compared to WT RIα (black, IC_{50} = 29 nM). Error bars represent standard deviations of measurements performed in triplicate. (**f**) Same as (e), but for the E143C/S236C double mutant (green, IC_{50} = 0.9 nM).

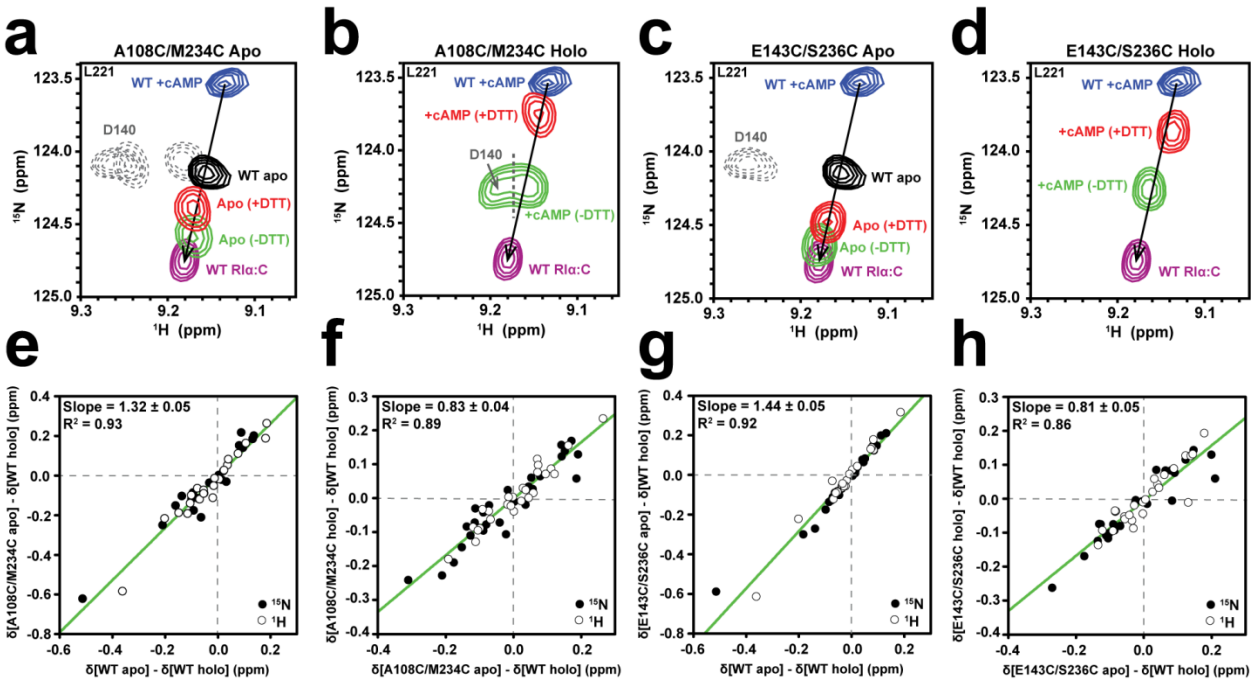

Figure 2. State-selective disulphide bridges partially stabilize the inactive state in both apo and holo forms. (**a-d**) Overlaid HSQC cross-peaks of reporter residue L221 for the disulphide mutants A108C/M234C and E143C/S236C RIα (91-244) in the absence (a, c) or presence (b, d) of cAMP. Due to fast exchange, the observed chemical shifts are linear averages and depend on the relative populations of the inactive and active states. (**a**) The WT apo peak (black) appears in the ~middle of WT RIα (91-244):cAMP (blue) and WT RIα (91-244):C (purple) resonances, indicating comparable sampling of the active and inactive states. Apo A108C/M234C in the absence of the DTT reducing agent (green) exhibits greater inactive state population than apo WT. In the presence of DTT (red), the disulphide bridge is at least partially reduced, causing partial reversion towards apo WT by decreasing the proportion of the inactive state. (**b**) Similar to panel (a) but in the presence of saturating amounts of cAMP. Even in presence of the cAMP activator, the A108C/M234C disulphide bridged construct (green) preserves a significant population of inactivate state. (**c**) As (a), but for disulphide mutant E143C/S236C in the apo form. (**d**) As (c), but for E143C/S236C in the holo (*i.e.* cAMP-bound) form. (**e, f**) Chemical shift correlation plots to measure the change in the overall extent of inactivation in the apo and holo disulphide-bridged A108C/M234C double mutant. Residues included in these plots were selected according to conditions (a-c) in p. S4 of the Supplementary Material. Open and closed circles denote ^{1}H and ^{15}N chemical shift values, respectively, the latter scale by 0.181[47]. Based on Supplementary equations S17 and S14, the slopes of the plots in panels (e) and (f) report on the relative changes in the inactive state populations. For example, in panel f the slope represents the $\frac{X_{Inactive,Mut\ Holo}}{X_{Inactive,Mut\ Apo}}$ ratio, which is required for the $K_{a,Obs}$ correction according to equation (3). (**g**, **h**) As (e, f), but for the disulphide mutant E143C/S236C RIα (91-244).

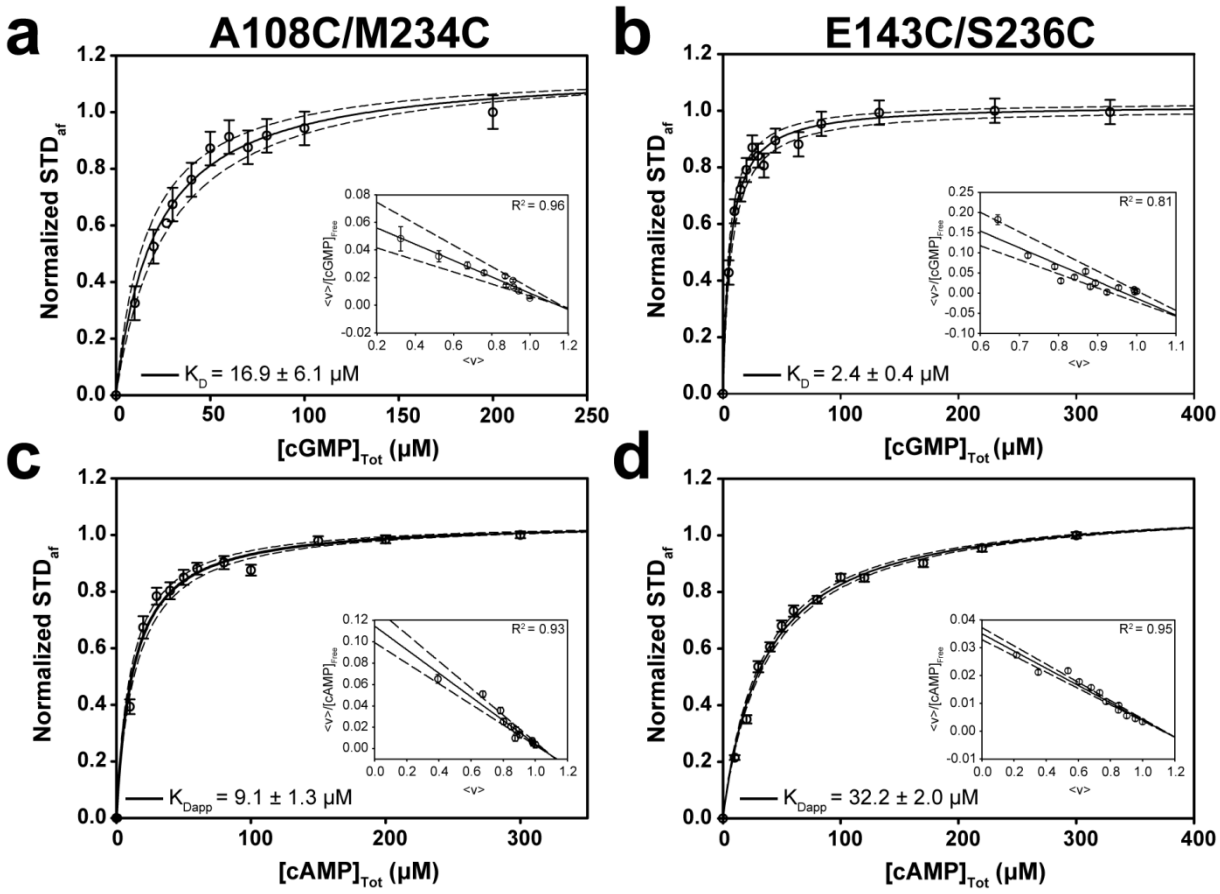

Figure 3. Measuring affinities for the "stapled" mutants. (**a**) Isotherm for the binding of cGMP to the A108C/M234C disulphide-bridged mutant of RIα (91-244). The dissociation constant of cGMP is required to determine the $K_{D,Obs}$ of cAMP from the competition experiment. The STD/STR ratio from the ribose H1' was used to build the dose-response curve. *Inset*: Scatchard plot (<v>/[L] *vs.* <v>) used to calculate the dissociation constant ($K_{D,cGMP}$ = 16.9 ± 6.1 µM). Dashed curves were obtained using the 'edge' values of K_D (*e.g.* 10.8 and 23.0 µM). (**b**) As (a), but for the E143C/S236C double mutant ($K_{D,cGMP}$ = 2.4 ± 0.4 µM). (**c**) Binding isotherm for the cAMP-titration of A108C/M234C pre-saturated with 500 µM cGMP ($K_{Dapp,cAMP}$ = 9.1 ± 1.3 µM). (**d**) As (c), except for the disulphide mutant E143C/S236C ($K_{Dapp,cAMP}$ = 32.2 ± 2.0 µM).

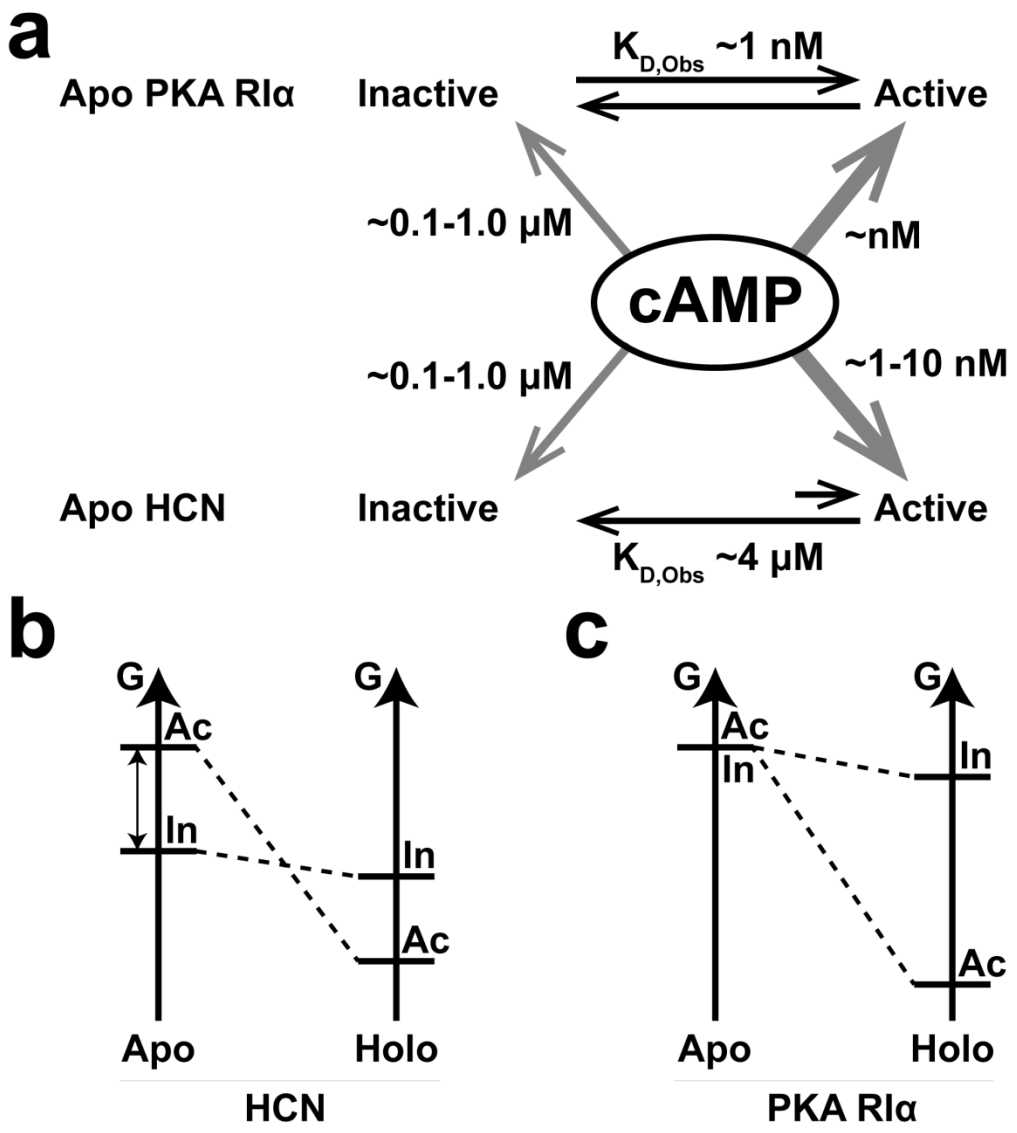

Figure 4. Apo population and state-specific K_D, and free energy comparison for RIα and HCN. (**a**) RIα and HCN bind cAMP with comparable affinities when either in the active (~nM) or inactive (~sub-μM) conformations (thick gray arrows *vs.* thin gray arrows), yet display a ~10^3 difference in observed K_D. This is because their respective apo populations of active *vs*. inactive states differ significantly (black arrows). Apo PKARIα samples active and inactive forms ~equally (~50%), while apo HCN mainly exists in the inactive state, resulting in lower cAMP affinity. (**b**,**c**) Free energy differences between active (Ac) and inactive (In) states of the apo and cAMP-bound forms of HCN (c) and PKA RIα (c). The free energy diagram illustrates qualitative changes and is not to scale.

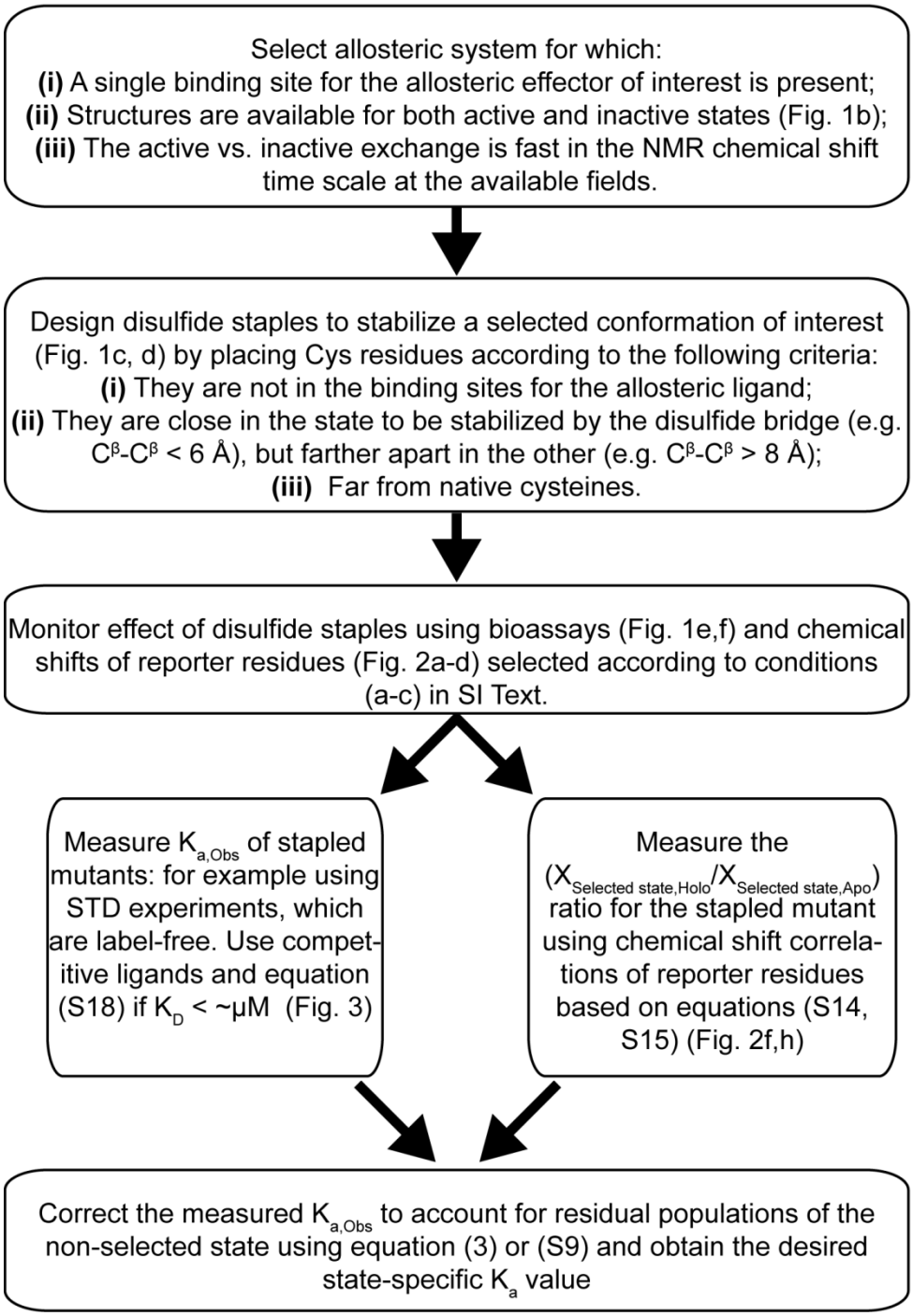

Figure 5. Summary flowchart of the protocol proposed to measure state-specific association constants in allosteric sensors. A similar flowchart is applicable also when the $K_{a,Obs}$ values are measured by methods different from STD (*e.g.* Isothermal Titration Calorimetry, Surface Plasmon Resonance, fluorescence based methods etc.) or when the active *vs.* inactive equilibrium is perturbed by modifications different from disulphide bridges (*e.g.* point mutations, post-translational modifications etc.).

3.7 Supplementary Information

3.7.1 Derivation of Equation (2) through Binding Polynomials

The binding polynomial for the thermodynamic cycle of Fig. 1a is:

$$Q = \left(1 + K_{a,Active}[A]\right) + L(1 + K_{a,Inactive}[A]) \qquad \text{(S1)}$$

where A is the allosteric effector (*e.g.* cAMP), $[A]$ is the concentration of free A and L is the equilibrium constant for the inhibitory equilibrium of the apo form:

$$L = X_{Inactive,Apo}/X_{Active,Apo} \qquad \text{(S2)}$$

Considering that the fractional saturation with respect to A is given by[1].

$$< v > = \frac{\partial \ln Q}{\partial \ln [A]} \qquad \text{(S3)}$$

We obtain:

$$< v > = \frac{K_{a,Obs}[A]}{(1+K_{a,Obs}[A])} \qquad \text{(S4)}$$

with:

$$K_{a,Obs} = \frac{1}{1+L} K_{a,Active} + \frac{L}{1+L} K_{a,Inactive} \qquad \text{(S5)}$$

Considering equation (S2) and the normalization condition:

$$1 = X_{Inactive,Apo} + X_{Active,Apo} \qquad \text{(S6)}$$

equation (S5) re-arranges to equation (2):

$$K_{a,Obs} = X_{Inactive,Apo}K_{a,Inactive} + X_{Active,Apo}K_{a,Active} \qquad (2)$$

3.7.2 Derivation of Equation (3)

In the presence of a large excess of free ligand A (*i.e.* $K_{a,Inactive}|cA| \gg 1$ and $K_{a,Active}|cA| \gg 1$):

$$\frac{X_{Inactive,Holo}}{(1- X_{Inactive,Holo})} \cong L\left(\frac{K_{a,Inacive}}{K_{a,Active}}\right) \qquad (S7)$$

Therefore the $K_{a,Active}$ in equation (2) can be replaced by:

$$K_{a,Active} = LK_{a,Inactive}\frac{(1-X_{Inactive,Holo})}{X_{Inactive,Holo}} \qquad (S8)$$

Considering equations (S2) and (S6), equation (2) then simplifies to:

$$K_{a,Inactive} = K_{a,Obs}(\frac{X_{Inactive,Holo}}{X_{Inactive,Apo}}) \qquad (3)$$

A similar equation is obtained for $K_{a,Active}$ by replacing $K_{a,Inactive}$ in equation (2) with the $K_{a,Inactive}$ derived from equation (S8):

$$K_{a,Active} = K_{a,Obs}(\frac{X_{Active,Holo}}{X_{Active,Apo}}) \qquad (S9)$$

Using equations (3) and (S9), $K_{a,Inactive}$ and $K_{a,Active}$, respectively, are determined directly from the measured $K_{a,Obs}$ values. When the apo (holo) inhibitory equilibrium is highly skewed towards the inactive (active) state, equations (3) and (S9) are most useful as applied to mutants that shift the equilibrium towards either the inactive or the active state, respectively, thus avoiding error-prone scenarios in which $X_{Inactive,Holo} \sim 0$ in equation (3) or $X_{Active,Apo} \sim 0$ in equation (S9). The molar fraction ratios required to implement equations (3) and (S9) are

measured through chemical shift correlation plots, assuming a fast exchanging inactive *vs.* active equilibrium, as explained below.

3.7.3 Measurement of Population Ratios (*e.g.* $\frac{X_{Inactive,Holo}}{X_{Inactive,Apo}}$ in Equation 3) through Chemical Shift Correlations

Residues that are sufficiently far from the binding site of ligand A and from the Cys mutation sites sense primarily the fast exchanging inactive *vs.* active equilibrium. In the case of RIα (91-244) these residues matched three criteria:

(a) C^{β}-C^{β} distances > 8 Å from residues in contact with the cAMP ligand

(b) Nearest atom distance > 5 Å from each mutation site

(c) $|\cos\theta| > 0.9$, where

$$\cos(\theta) = \frac{\vec{A}\cdot\vec{B}}{|\vec{A}||\vec{B}|} \qquad \text{(S10)}$$

$\vec{A}$ is the vector between WT apo and mutant apo, or WT holo and mutant holo, and $\vec{B}$ is the vector between WT apo and WT holo, as typically used for the chemical shift projection analysis (CHESPA, Figure S1)[2,3]. θ is the angle between vectors $\vec{A}$ and $\vec{B}$. Through criteria (a-c) it is possible to find residues that report primarily on the inactive *vs.* active equilibrium (Figure S2). Assuming fast inactive *vs.* active exchange, for these residues the following equation applies:

$$\delta_{Mut,Apo} = X_{Inactive,Mut,Apo}\delta_{Inactive} + \left(1 - X_{Inactive,Mut,Apo}\right)\delta_{Active} \qquad \text{(S11)}$$

where $\delta_{Mut,Apo}$ is the chemical shift for the mutant apo form and $\delta_{Inactive}$ and δ_{Active} represent chemical shifts for the pure inactive and active populations, respectively. The $X_{Inactive,Mut,Apo}$ is

the molar fraction of inactive state for the mutant apo form. Assuming the WT holo sample represents the fully active state, *i.e.* $\delta_{Active} \approx \delta_{WT,Holo}$, equation (S11) re-arranges to:

$$\delta_{Mut,Apo} - \delta_{WT,Holo} = X_{Inactive,Mut,Apo}(\delta_{Inactive} - \delta_{Active}) \quad \text{(S12)}$$

Proceeding similarly for the mutant holo form, a similar equation is obtained:

$$\delta_{Mut,Holo} - \delta_{WT,Holo} = X_{Inactive,Mut,Holo}(\delta_{Inactive} - \delta_{Active}) \quad \text{(S13)}$$

Combining equations (S10) and (S11), we obtain:

$$\frac{(\delta_{Mut,Holo} - \delta_{WT,Holo})}{(\delta_{Mut,Apo} - \delta_{WT,Holo})} = \frac{X_{Inactive,Mut,Holo}}{X_{Inactive,Mut,Apo}} \quad \text{(S14)}$$

Equation (S14) means that plots of $(\delta_{Mut,Holo} - \delta_{WT,Holo})$ *vs.* $(\delta_{Mut,Apo} - \delta_{WT,Holo})$ are linear with a slope equal to the ratio of the inactive populations in the holo *vs.* apo mutant forms, which is needed in equation (3) to correct $K_{a,Obs}$ and find $K_{a,Inactive}$. These types of plots are shown in Fig. 2f,h for the ^{1}H and ^{15}N spins of residues satisfying conditions (a-c) above. Proceeding similarly, it is also possible to show that equation (S11) leads to:

$$\frac{(\delta_{Mut,Holo} - \delta_{Inactive})}{(\delta_{Mut,Apo} - \delta_{Inactive})} = \frac{X_{Active,Mut,Holo}}{X_{Active,Mut,Apo}} \quad \text{(S15)}$$

Equation (S15) is useful to measure the $\frac{X_{Active,Mut,Holo}}{X_{Active,Mut,Apo}}$ ratio required to implement equation (S9) for systems in which the WT apo inhibitory equilibrium is highly skewed towards the inactive state, so that: $\delta_{Inactive} \approx \delta_{WT,Apo}$. Equation (S12) can also be combined with a similar equation derived for the WT apo form:

$$\delta_{WT,Apo} - \delta_{WT,Holo} = X_{Inactive,WT,Apo}(\delta_{Inactive} - \delta_{Active}) \quad \text{(S16)}$$

Resulting in:

$$\frac{(\delta_{Mut,Apo} - \delta_{WT,Holo})}{(\delta_{WT,Apo} - \delta_{WT,Holo})} = \frac{X_{Inactive,Mut,Apo}}{X_{Inactive,WT,Apo}} \qquad \text{(S17)}$$

Equation (S17) means that plots of $(\delta_{Mut,Apo} - \delta_{WT,Holo})$ *vs.* $(\delta_{WT,Apo} - \delta_{WT,Holo})$ are linear with a slope equal to the ratio of the inactive populations in the mutant *vs.* WT apo forms. These types of plots are shown in Fig. 2e,g and provide an estimation of the change of state populations in the apo mutant relative to the apo WT.

3.7.4 Analysis of Competition Binding Experiments

The titration of cAMP into PKA RIα (91-244) mutants was implemented in the presence of a large excess competing ligand (*i.e.* cGMP), in order to bring the resulting apparent affinity for cAMP within the window accessible through the STD experiments, which do not require any exogenous label. This competition-based titration provides only a $K_{Dapp,cAMP}$ for cAMP binding, which is then converted into the actual K_D for cAMP dissociation through the following equation:

$$K_{D,cAMP} = \frac{K_{Dapp,cAMP}}{(1+\frac{[cGMP]}{K_{D,cGMP}})} \qquad \text{(S18)}$$

where $K_{D,cAMP}$ and $K_{D,cGMP}$ are the dissociation constants for cAMP and cGMP, respectively, and [cGMP] is the concentration of excess free cGMP (*i.e.* $[cGMP] \approx [cGMP]_{Tot.} - [Protein]_{Tot.} =$ 490 μM within ~2% error). The $K_{D,cGMP}$ value was measured directly through STD measurements (Figure 3), since cGMP binds PKA R more weakly than cAMP.

3.8 Supplementary References

1. Dill, K. A. & Bromberg, S. *Molecular Driving Force*. *Stat. Thermodyn. Chem.* (2011).

2. Selvaratnam, R. *et al.* The projection analysis of NMR chemical shifts reveals extended EPAC autoinhibition determinants. *Biophys. J.* **102,** 630–639 (2012).

3. Selvaratnam, R., Mazhab-Jafari, M. T., Das, R. & Melacini, G. The Auto-Inhibitory Role of the EPAC Hinge Helix as Mapped by NMR. *PLoS One* **7,** 1–9 (2012).

3.9 Supplementary Figures

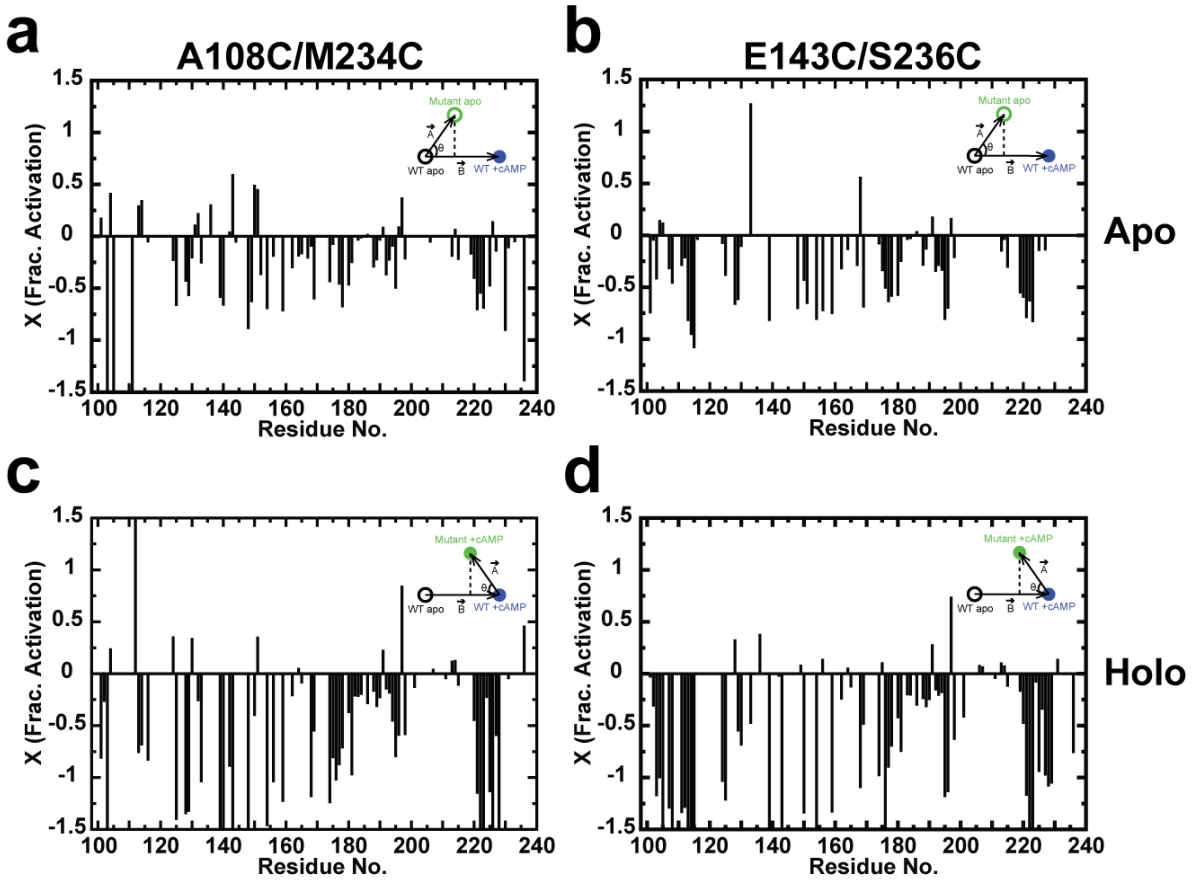

Figure S1. CHESPA Analyses of the disulphide mutants. Chemical shift projection analyses (CHESPA)[48,49] were employed to probe at residue resolution the perturbations caused by the A108C/M234C and E143C/S236C disulphide-bridges in the apo **(a, b)** and holo **(c, d)** forms. The two reference states that define the reference CHESPA vector (*i.e.* A) are WT apo and WT cAMP-bound forms (inset), with the perturbation that defines the CHESPA vector B being the disulphide mutant, either in the apo or holo forms (inset). The X fractional (in)activation reports on the degree of peak shifts, with respect to the reference states[2,3]. For the apo samples in panels (a, b), values of X = +1 indicate projection shifts similar to WT +cAMP, while values of X = -1 indicate comparable projection shifts but in the opposite (inactivating) direction. The projection analyses in panels (a, b) show that the majority of residues exhibit negative fractional activation values, pointing to a shift towards an inactive-like conformation. For the holo samples in panels (c, d), the reference vector changes (inset) to start from WT +cAMP. In this case, values of X = -1 indicate projection shifts close to WT apo. The projection analyses in panels (c, d) illustrate that the majority of residues exhibit negative fractional activation values, indicating a shift towards an inactive-like conformation even in the presence of saturating amounts of the endogenous activator, cAMP.

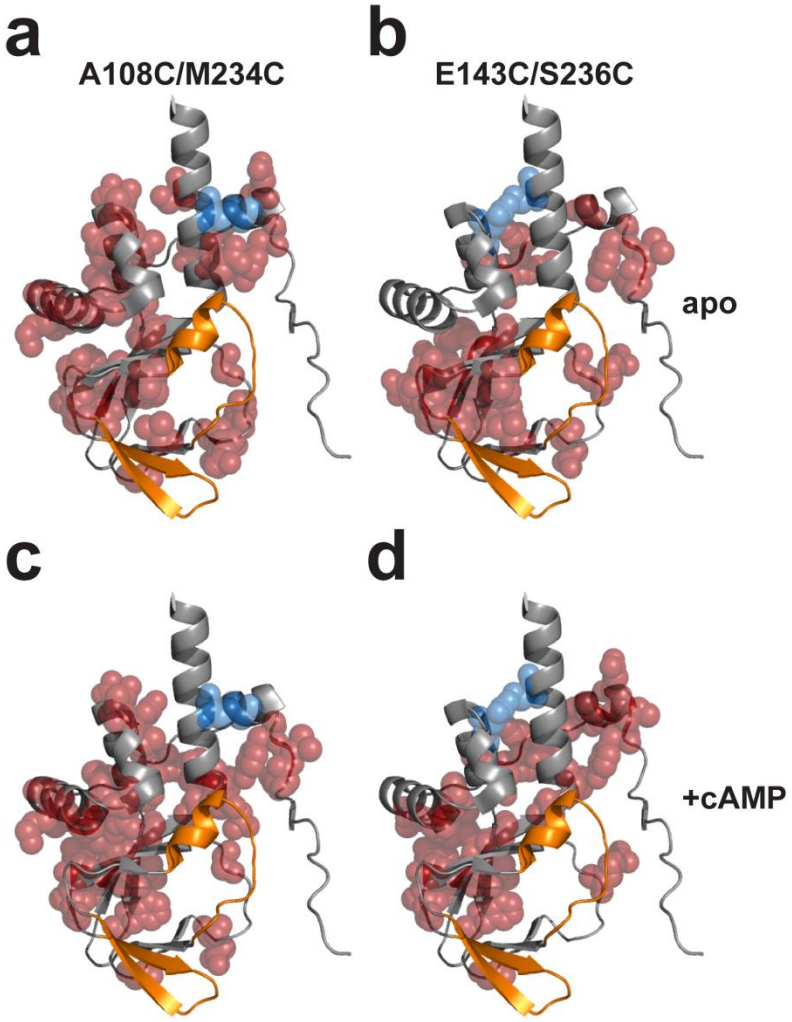

Figure S2. Map of reporter residues used in the assessment of the inactive state populations of RIα (91-244). (a-b) Reporter residues used for apo A108C/M234C and E143C/S236C are shown as red spheres, with the mutation pairs indicated by blue spheres. The orange ribbon denotes the PBC and BBR regions, similarly to Fig. 1. **(c-d)** As (a-b) but for the holo mutants. These residues fulfill conditions (a-c), reported in the supplementary text. Since both apo and holo disulphide mutants mainly capture the inactive form, correlated residues were reported on the C-bound structure of RIα (PDB 2QCS).

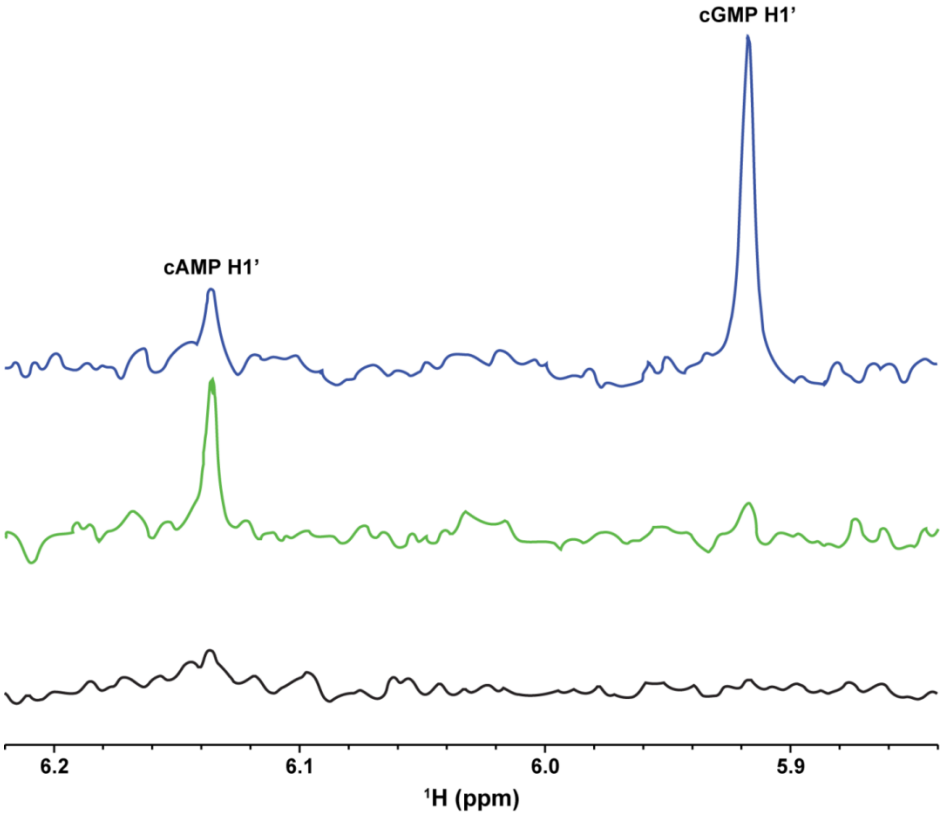

Figure S3. Comparison of cAMP STD signals in the presence and absence of cGMP. In the absence of cGMP (black spectrum), the ^{1}H1' cAMP resonance is marginal even at saturation, since binding is still relatively tight (*i.e.* K_D < ~μM). However, when saturating amounts of cGMP are added (blue spectrum), the cAMP signal increases significantly. When cAMP saturation is reached, in the presence of excess cGMP (green), the ^{1}H1' cAMP signal is maximized, resulting in a reliable measurement of the apparent STD_{af}. These spectra were acquired for the E143C/S236C mutant of RIα (91-244).

Chapter 4

The Importance of Non-Contact Side-Chains and Capping Residues in Tuning PKA RIα cAMP Affinity

4.1 Preface

All experimental work was conducted by K. Moleschi and O. Byun. K. Moleschi cloned majority of the BBR and PBC mutations into PKARIα (91-244), with the exception of A211D and A211T (96-244), which was carried out by O. Byun. The STD NMR screen, acquisition and processing of HSCQs, and urea unfolding assays of BBR and PBC mutants (91-244) were performed by K. Moleschi. HSQC, and both urea unfolding and kinase inhibition assays of A211D/T (96-244) were performed by O. Byun under the supervision of K. Moleschi.

4.2 Introduction

As established in chapter one, CBDs are structurally homologous yet highly variable in cAMP affinity (μM-nM; Table 1). While the position of the pre-equilibrium is one mechanism to control cAMP affinity among CBDs, as discussed in great detail in chapter three, the contributions to cAMP affinity of different cAMP binding regions and of specific residues within these regions is currently not fully understood. CBDs typically bind cAMP through three distinct regions, the PBC, the BBR and the lid. Deletion of the latter has been shown to be dispensable for high affinity (nM) binding of cAMP to PKA RIα CBD-A[1], while the relative contributions of the PBC and BBR to cAMP binding have not been systematically quantified. Sequence alignment shows that the PBC and BBR residues whose side chains contact cAMP are conserved in both low and high affinity CBDs (Fig. 1; Table 1). This observation suggests the hypothesis that other cAMP binding pocket residues, which are not in direct contact with cAMP and are not conserved among other CBDs, may modulate cAMP affinity. To test this hypothesis and dissect residue-specific contributions to cAMP-affinity, we comparatively analyzed multiple BBR and PBC mutants of PKA RIα CBD-A using a combination of STD NMR and urea unfolding monitored by intrinsic fluorescence.

4.3 Dissecting the Role of the BBR in cAMP Binding by STD NMR

Selected mutations of the BBR were generated and tested with STD to determine the possible function of the BBR in modulating the CBD:cAMP affinity. The only cAMP contact within the BBR regions of PKARIα is mediated by V182, whose side chain hydrophobically interacts with the adenine base within cAMP[2]. Hence, V182 is the BBR residue most likely to affect cAMP affinity when mutated. When the STD experiment was performed for V182A in the

presence of cAMP, no ligand signals were observed, similarly to WT. Due to the inherent limitations of the STD K_D window[3], this could be the result of very tight cAMP binding or the complete inability of RIα to bind cAMP. To differentiate between these scenarios, STD experiments were then performed with Sp-cAMPs, a phosphorothioate analogue of cAMP. Similar to cAMP, Sp-cAMPs is an agonist but with lower affinity than the endogenous activator cAMP[4,5]. The resonances of both H2/H8 and H1' were observed in the STD spectrum of Sp-cAMPs, indicating that in the previous STD experiment on V182A in the presence of cAMP, binding was still occurring, but too tightly to be detected (Fig. 2a). However, even when comparing the Sp-cAMPs STD:STR ratios of V182A for H2/H8 and H1' signals, intensities remain within error of WT, suggesting that the V182 hydrophobic contact does not contribute significantly to cAMP affinity. Given that V182 is the only BBR contact residue, the marginal role of V182 in cAMP affinity suggests that the BBR does not significantly contribute to cAMP affinity. This prediction was confirmed through further mutations.

Two other residues in the RIα BBR were mutated to the corresponding side-chains of another structurally homologous CBD, HCN2 and 4, which bind cAMP with low (μM) affinity (Table 1). This included M180 and N186 , which align to V and G, respectively, in the BBR of HCN2 and 4 (Table 1). Similar to the V182A mutant, no observable STD signal was generated in the presence of cAMP, and so Sp-cAMPs was utilized (Fig. 2a). Again, the STD intensities seen in Fig. 2 mostly remain within error of WT, suggesting that the mutated side-chains are not key determinants of the high affinity for cAMP observed in RIα. The STD:STR value of H2/H8 for N186G is slightly outside the error of WT. Nonetheless, the fact that no STD:STR signal is observed for N186G with cAMP strongly suggests minimal changes to cAMP affinity. The

combination of these data suggests that the BBR contributes minimally to cAMP affinity. As such, we turned to dissecting the role of PBC residues in cAMP affinity modulation.

4.4 Dissecting the Role of PBC Residues in cAMP Binding by STD NMR

An alanine scan of the PBC was performed to test its role in cAMP binding. All non-alanine PBC residues were mutated to alanine (*i.e.* L201, L203, I204, Y205, G206, T207, and P208), with the exception of E200 and R209, whose side-chain are essential for cAMP binding to both low and high affinity CBDs (Table 1). Several PBC mutants generated significant increases in STD signal, relative to the WT and other mutants (Fig. 2b). Clear resonances were observed for ^{1}H2, ^{1}H8, and ^{1}H1' within the cAMP ligand[6] (Fig. 2b). When compared to the STR in the form of an STD:STR ratio, relative binding affinities can be estimated considering that the cAMP concentration was kept constant in all STD experiments reported in Fig. 2[3]. For example, signals with an increase in the STD signal, relative to the reference spectra (STR), exhibit lower cAMP affinity.

Among the tested mutated amino acids, L201A and Y205A showed the largest STD:STR intensity ratio increases, or lowest cAMP affinities (Fig. 2c). The remaining tested residues (*i.e.* L203A, I204A, G206A, T207A, and P208A) were within error of the wild-type ratios. Statistical Z-scores were used to quantify the significance of the changes in STD/STR ratios. The Z-scores and population means for H1', which is the best resolved resonance of cAMP, are reported directly in the Figure 2c. The Z-scores are a measure of the number of standard deviations a sample is from the population mean. Mutants L201A and Y205A exhibit significantly higher STD:STR intensity ratios than the other mutants, and are greater than the population mean,

resulting in positively large Z-scores. In addition to the STD screen, urea unfolding data was also obtained for the PBC mutants.

4.5 Urea Unfolding of Selected PBC Mutants

The STD data was complemented with affinity determinations through urea unfolding. The apo *vs.* holo unfolding free energy differences (*i.e.* ΔΔG) were utilized to quantify cAMP binding affinities (Table 2). Figure 3 focuses on a sub-set of four representative Ala mutations, *i.e.* L201A and Y205A, with positive Z-scores (Figure 2c), and L203A and I204A, which represent residues with negative Z-scores (Figure 2c) based on the STD pre-screening. For these four, mutant urea unfolding was monitored through intrinsic fluorescence, since residues Trp188 and Trp222 are located in the CBD-A[1].

The measured ΔΔG values (Table 2) confirm the unique differences among the PBC mutants identified through the STD screening (Figure 2). Mutants L203A and I204A result in ΔΔG values that correspond to only minimal changes in the overall cAMP affinity (*i.e.* ~one order of magnitude from WT; Table 2). In contrast, more significant changes are detected for mutants L201A and Y205A, with ΔΔG values corresponding to cAMP affinities reduced by two-three orders of magnitude relative to WT (Table 2), in agreement with the enhanced STD signal observed for these mutants (Figure 2). Considering that the measured affinities are averages over the active and inactive states sampled by the apo CBD, the reduced affinities observed for L201A and Y205A may arise from changes in the active *vs.* inactive apo populations or from alterations in state-specific association constants. To differentiate between these scenarios, we gauged the position of the apo inhibitory equilibria of the mutants in Table 2, using chemical shift correlation analyses.

4.6 Equilibrium and State-Specific K_a Analysis

Taking advantage of recent NMR chemical shift comparisons[7], we obtained spectra for the apo mutant and apo WT forms to determine if any difference in the apo conformational equilibrium was detected (Fig. 3a-d). The slopes of the $Mut_{Apo} - WT_{Holo}$ *vs.* $WT_{Apo} - WT_{Holo}$ chemical shifts are expected to be linear, as shown in Fig. 3a-d, with a slope equivalent to the change in autoinhibitory equilibrium. For the L201A, L203A and I204A mutants the slope is close to ~1 (*i.e.* ≤ 1.1), suggesting that in these mutants the position of the autoinhibitory equilibrium remains largely unperturbed; while for Y205A a slope of ~1.2 is measured, pointing to a ~20% increase in the fraction of apo-inactive state. However, the 20% increase in the population of inactive state cannot account for the large decrease in cAMP affinity. The back-calculated K_D for the Y205A:cAMP complex, using the increased apo inactive state population, is 1.3 nM, *i.e.* only a 0.30 nM increase over WT. Clearly this change in the apo autoinhibitory equilibrium elicits only a negligible effect on the K_D for cAMP and does not account for the observed lowered cAMP affinity. These results suggest that the L201A and Y205A mutations induce significant changes at the level of state-specific K_a values. Considering that the PBC is a major cAMP affinity determinant and that a critical active *vs.* inactive difference is the stability of the PBC helix, the impact of the non-contact side-chains of L201 and Y205 on the state-specific affinities is consistent with a destabilization of the PBC helix upon mutations of these side-chains to Ala. In fact, a key helix stabilizing interaction involves Van der Waals contacts between the side-chains of Leu/Val and Tyr residues at positions (i, i + 4), as is the case for L201 and Y205 in RIα[8] (Fig. 4).

4.7 CNC/Acrodysostosis Associated Mutations within the PBC

Many CNC/acro mutants have been discovered that translate directly into the amino acid sequence of PKARIα and two have been identified within the C-terminal region of the PBC[9–12]. RIα mutants A211D and A211T were cloned into 96-244 and assessed for any changes in structure, conformational equilibria, and cAMP affinity. This was performed using a combination of chemical shifts, projection analyses, and urea unfolding monitored by intrinsic tryptophan fluorescence.

To see whether any changes to the autoinhibitory equilibrium (*i.e.* active *vs.* inactive populations) are induced by the A211D/T mutations, we used residue L221 as a reporter residue as it is sufficiently removed from the cAMP binding interface, and primarily reports on conformational exchange of the two states[1] (Fig. 5a). In the case of apo A211D, the L221 resonance remains on top of the WT apo peak, suggesting that there is little to no change in the pre-equilibrium. When cAMP is added, a marginal shift towards WT +cAMP is seen indicating partial activation. It could be that mutant A211D has become desensitized to cAMP or perhaps saturating ligand concentrations were not reached. For binding, T190 was used as a reporter residue, as it resides within the BBR and is sensitive to the presence or absence of ligand. No peak for A211D is seen for T190 +cAMP (Fig. 5b). This peak could be broadened beyond detection due to intermediate-regime chemical exchange or perhaps the T190 reporter is close enough to A211 to result in nearest neighbour effects.

As to the RIα A211T mutant, both cAMP affinity and the level of activation are affected. The apo A211T cross-peak of reporter residue L221 superimposes well with WT apo, meaning little change to the apo autoinhibitory equilibrium is occurring (Fig. 5c). When excess cAMP is added to the sample, a large shift towards activation is observed, but less so than WT holo. The

binding reporter residue T190 suggests that the BBR for A211T is not fully cAMP-bound when cAMP binds (Fig. 5d). There appears to be some desensitization and reduced affinity for cAMP.

To expand on the reporter residue L221, chemical shift analyses were performed for all resonance assigned in A211D and A211T to check for changes in the apo autoinhibitory equilibrium. As such apo mutant shifts were compared to WT apo/holo forms and were plotted in Fig. 6a,b. The resulting linear slope reports on the $\frac{Mut_{Apo}-WT_{Holo}}{WT_{Apo}-WT_{Holo}}$ ratio, which provides a direct measure of changes to the pre-equilibrium. Slope values for both A211D and A211T are ~1, suggesting little change to the populations of the active *vs.* inactive states, consistent with the L221 probe. To expand on the NMR work, urea unfolding was also utilized to monitor free energy as well as cAMP binding affinities.

Urea-induced unfolding assays monitored by intrinsic tryptophan fluorescence were performed on the apo and holo forms of WT, A211D, and A211T (Fig. 7a). The ΔG values extracted from the apo/holo WT forms (Fig. 7b) were used to generate ΔΔG's to compute cAMP affinity K_Ds (Fig. 7c). This equated to a cAMP K_D of ~2 nM for the WT form, which matches well with previous data (Table 3)[1]. The urea unfolding curve for apo A211D is moderately less stable than apo WT, as seen by the lower inflection point (Fig.7). When the unfolding was performed for holo A211D, the apo *vs.* holo curves remained similar, and within error from the apo form suggesting cAMP desensitization. With 100x excess ligand in the urea assay and still no real changes observed between apo and holo A211D curves, and considering the 10x cAMP concentration in the NMR with little spectral changes, it is likely that cAMP saturation is incomplete in both cases. Table 2 illustrates the various thermodynamic parameters extracted from the urea unfolding experiments. An extrapolated ΔΔG of 0.3 Kcal/mol equates to a cAMP

K_D of ~200 µM, confirming the predicted knockdown in cAMP affinity by NMR (Table 3). As for mutant A211T, considerable change is noted for the holo form, but less so for the apo sample, in comparison to their WT counterparts. Apo A211T is within error of apo WT, indicating no change in the pre-equilibrium, as shown by NMR. A large destabilization of holo A211T is observed, owing to the lesser cAMP affinity. Overall these data show lesser cAMP affinities of these mutants when compared to WT, and are in agreement with the NMR results. This work was also complemented with kinase inhibition assays.

Luminescence based kinase inhibition assays were performed for WT and mutant samples (91-244) to test whether the position of the apo autoinhibitory equilibrium was affected (Fig. 8). The degree of inhibition is measured through residual ATP concentrations which are then reported as relative luminescence units (RLU). It is expected that if the populations of the active and inactive states changed, this would then affect the affinity of RIα for the C-subunit, ultimately affecting the degree of inhibition. When comparing the IC_{50} values for WT, A211D, and A211T, they all remain very similar and thus the mutants retain similar affinity towards the C-subunit. These results also match well with previously published data[1]. This suggests that the active *vs*. inactive (*i.e.* pre-equilibrium) populations have not changed, and each are still sampled ~50%, similarly to WT. These data are supported by the results obtained by NMR via the reporter residue L221.

4.8 Hydrophobic Capping by PBC C-terminal Alanines

Structural studies have yielded that the C-terminal PBC alanine residues, A210 and A211, act as hydrophobic capping components to secure the adenine base of cAMP (Fig. 9). It is not surprising then that substitutions at these positions (*ie.* A211D/T) result in reduced cAMP

affinities and degrees of PKA activation. If A210 and A211 are sufficient to cap cAMP, anything with greater steric bulk is expected to perturb cAMP binding. In addition, the polar end-groups of aspartate and threonine are a potential source of electrostatic repulsion with the adjacent cAMP phosphate, which would further hinder binding. Both A211D and A211T possibly lack the necessary hydrophobicity to stabilize the adenine base.

Table 1. cAMP Binding Pocket Sequence and Affinity Comparisons.[a]

Protein	Sequence		Affinity
	BBR	PBC	
PKARIα (A)	^{180}MDVYVNNEWATSV^{192}	^{199}G**E**LALIYGTP**R**AA^{211}	4 nM
PKARIα (B)	AAVLQRRS-RVGRL	G**E**IALLMNRP**R**AA	< 1 nM
PKARIIβ (A)	FDIYVKCD-VGNYD	G**E**LALMYNTP**R**AA	1 nM
PKARIIβ (B)	VRITMKRK-EIARC	G**E**LALVTNKP**R**AA	12 nM
HCN4	VSVLTKGN KETKL	G**E**ICLLTRGR**RT**A	1 μM
HCN1	AGVITKSS KEMKL	G**E**ICLLTKGR**RT**S	2 μM
HCN2	VSVLTKGN KEMKL	G**E**ICLLTRGR**RT**A	4 μM

[a]Hydrophobic contact, **side-chain H-bond**, backbone H-bond (Fig. 1)

Table 2. Thermodynamic Unfolding Parameters of RIα (91-244)

RI Type	Apo ΔG^{oH_2O} (Kcal/mol)	Holo ΔG^{oH_2O} (Kcal/mol)	$\Delta\Delta G^{oH_2Oa}$ (Kcal/mol)	K_D (nM)
WT	3.7 ± 0.2	11.4 ± 0.2	7.7 ± 0.3	1
L201A	8.0 ± 1.0	9.9 ± 0.7	1.9 ± 1.2	1034
L203A	4.1 ± 0.4	9.7 ± 0.4	5.6 ± 0.6	29
I204A	4.5 ± 0.5	9.9 ± 0.4	5.4 ± 0.6	54
Y205A	6.0 ± 0.2	9.8 ± 1.2	3.8 ± 1.2	738
WT[b]	5.4 ± 0.3	12.8 ± 0.7	7.4 ± 0.8	2
A211D[b]	3.9 ± 0.1	4.2 ± 0.3	0.3 ± 0.3	200000
A211T[b]	5.8 ± 0.2	8.8 ± 0.3	3 ± 0.4	5000

[a]$\Delta\Delta G = \Delta G_{Holo} - \Delta G_{Apo}$, [b](96-244)

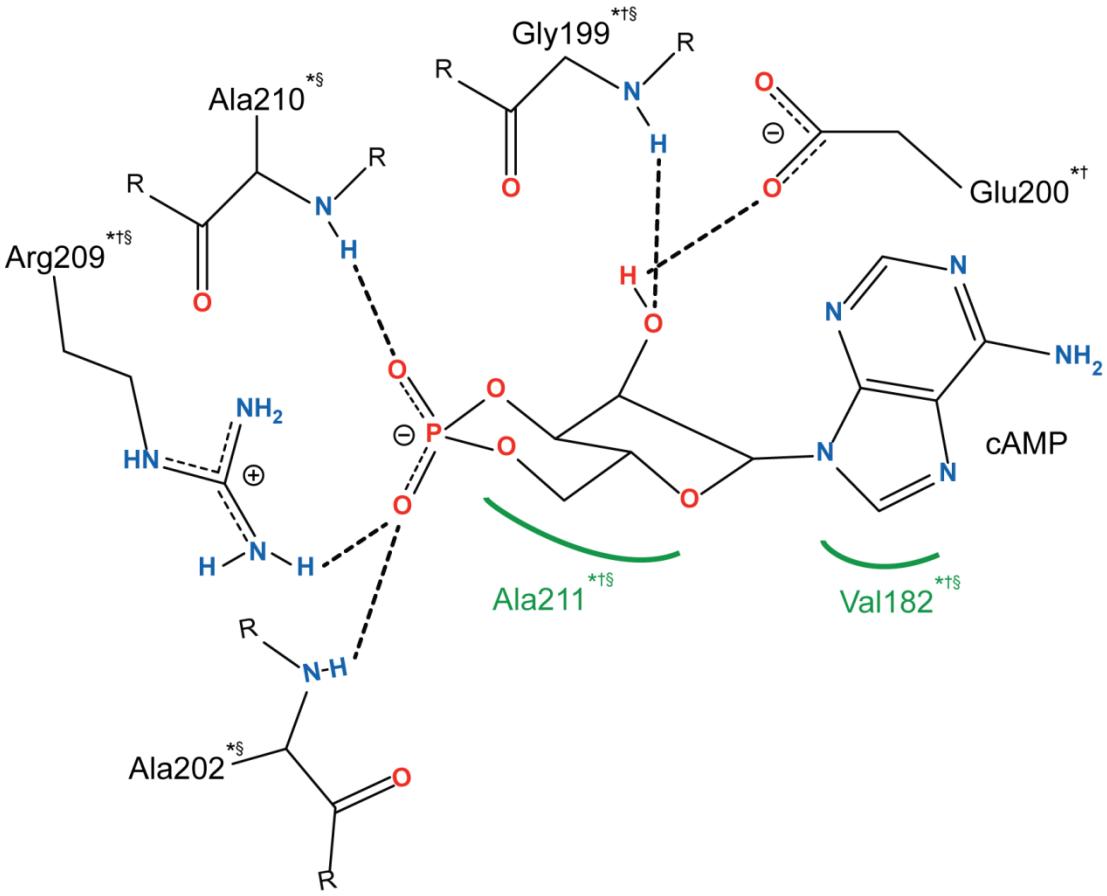

Figure 1. Important cAMP binding residues in CBD-A of RIα. Essential side-chain and backbone hydrogen bonds are shown as dashed lines, with hydrophobic contacts shown in green. Superscripts denote the CBD in which residue contacts are conserved: PKA RIIα/IIβ[*], HCN2/4[†], and EPAC2[§]). cAMP residue contacts were built from the PDB ligand explorer.

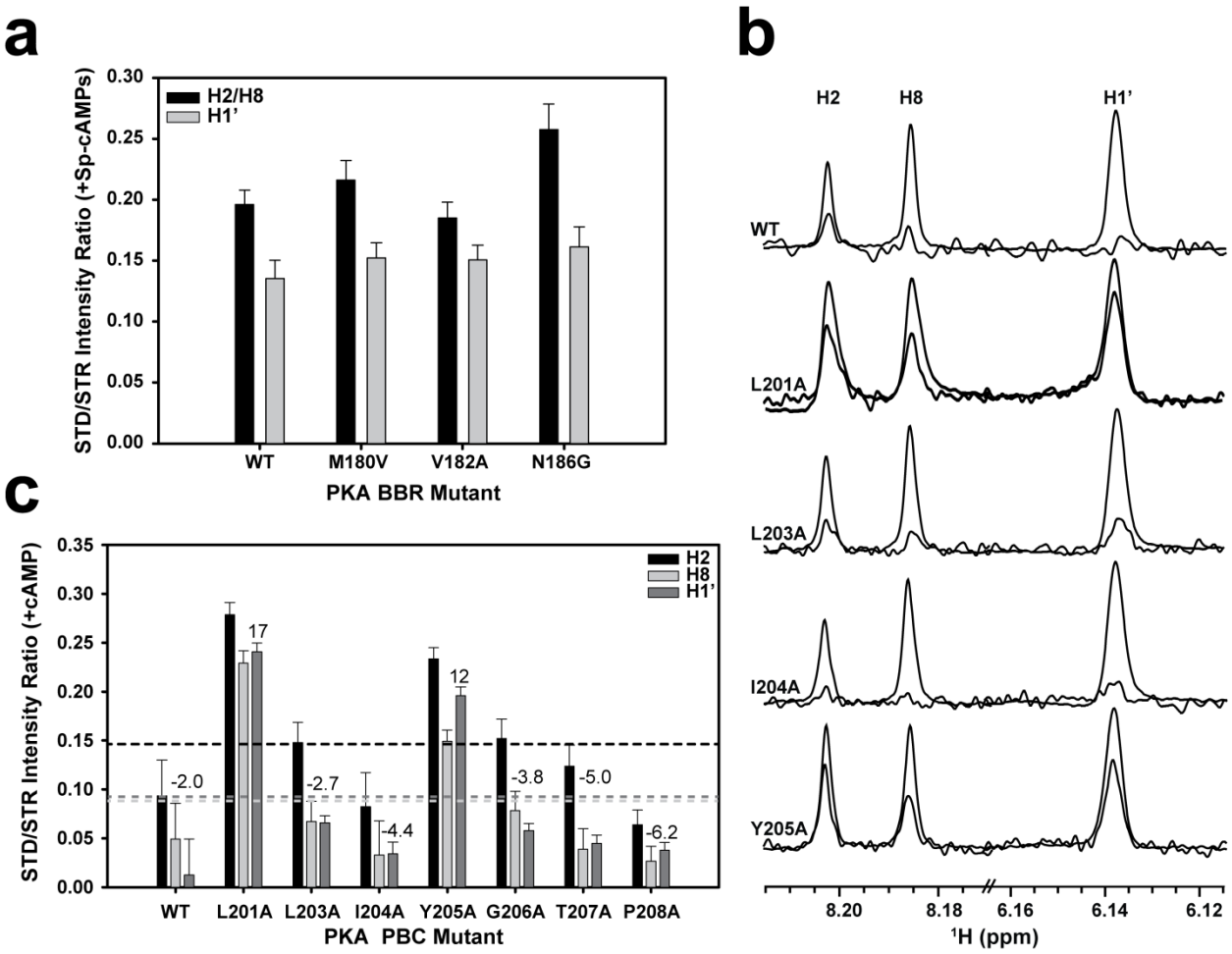

Figure 2. STD screening of BBR and PBC mutations. (**a**) BBR STD/STR intensity values of select mutations for the unresolved H2/H8 peak (black), as well as H1' (light gray) in the presence of the cAMP phosphorothioate analogue, Sp-cAMPs. Error bars report on spectral noise. (**b**) Raw STD spectra of select PBC mutants (L201A-Y250A) for H2, H8, and H1' resonances within the cAMP ligand. STD intensities were multiplied by 4-fold for clarity. The dashed line in the axis indicates a break. (**c**) STD/STR intensity ratios for entire Ala scan of PBC in the presence of cAMP. Ratio values are shown for H2 (black), H8 (light gray), and H1' (dark gray). Statistical Z-scores are reported directly in the figure for H1' with the populations means shown as dashed line following the same colour scheme. Error bars are a measure of spectral noise

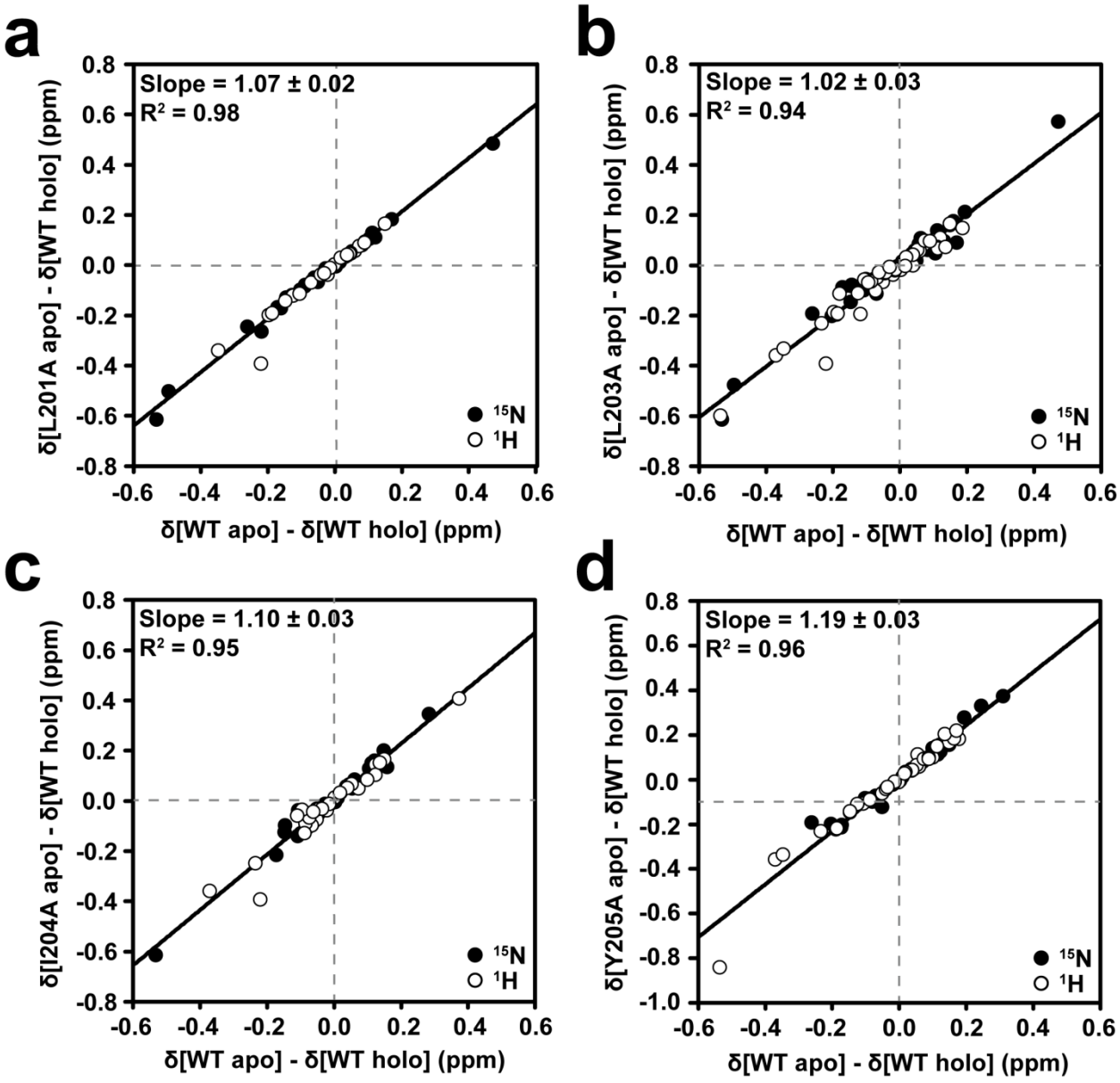

Figure 3. Effect on the apo autoinhibitory equilibrium by the PBC mutants. (**a**-**d**) Chemical shift analyses between mutant apo and WT apo/holo forms for determining changes in the position of the pre-equilibrium. The slopes are expected to be linear and equivalent to $\frac{X_{Inactive,Mut\ Apo}}{X_{Inactive,WT\ Apo}}$ with the slopes directly reporting on the equilibrium. Slope values ~1 indicate no change. Open and closed circles denote ^{1}H and ^{15}N chemical shift values, respectively, the latter scale by 0.181

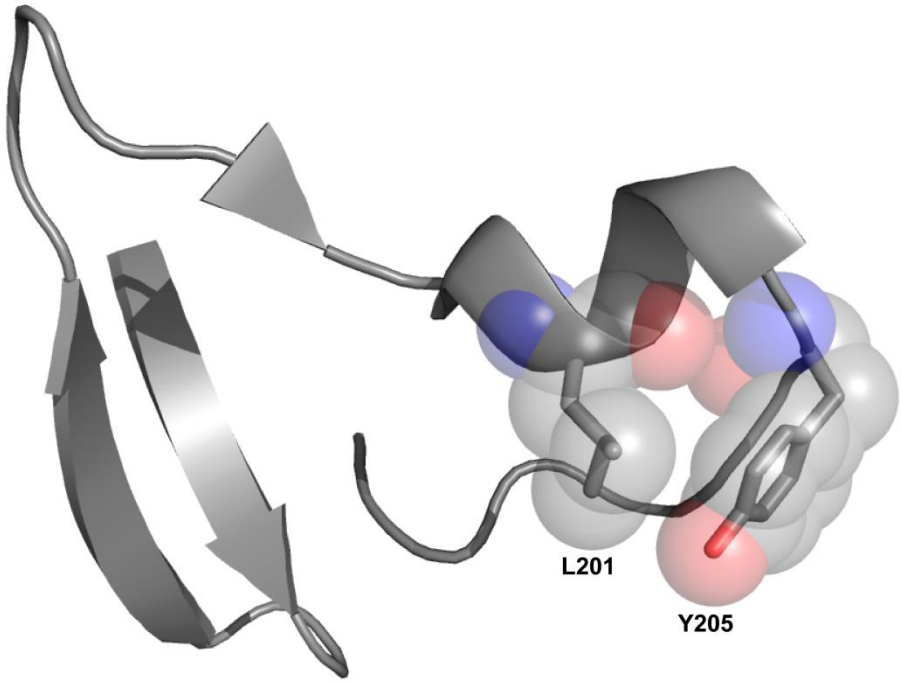

Figure 4. Helix stabilizing interaction between L201 and Y205. The cAMP binding pocket of PKA RIα (PDB 2QCS) is shown, illustrating the potential Van der Waals contacts between L201 and Y205 due to (*i*, *i* + 4) spacing within the phosphate binding cassette helix.

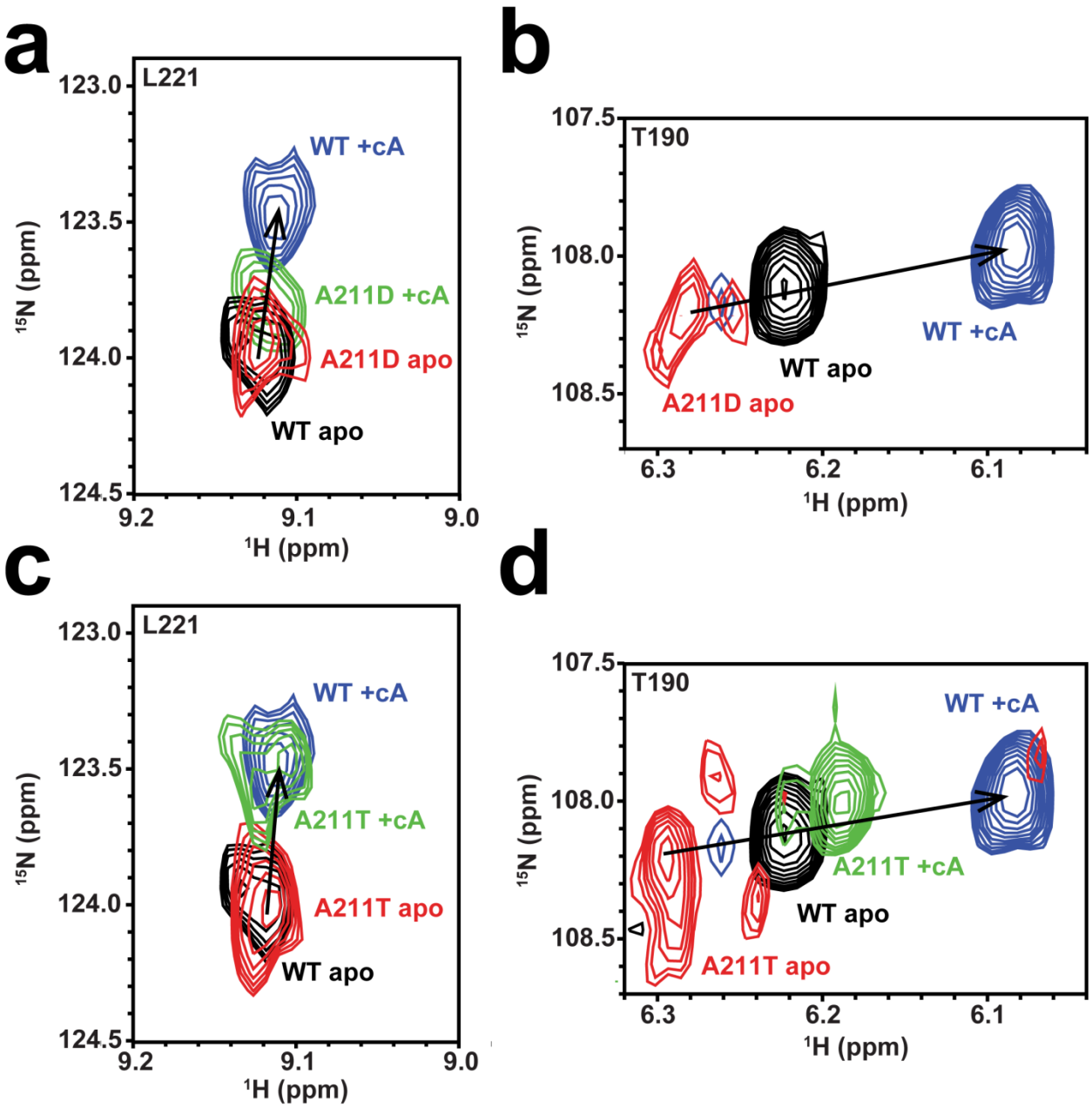

Figure 5. Reporter residues of conformational equilibrium and cAMP binding for disease-related mutants A211D/T. (**a-d**) Overlaid ^{1}H-^{15}N HSQC spectra of WT apo (black), WT +cAMP (blue), A221D/T apo (red), and A211D/T +cAMP (green) samples for reporter residue L221 (a,b) or T190 (c,d). This work was performed by O. Byun under the supervision of K. Moleschi.

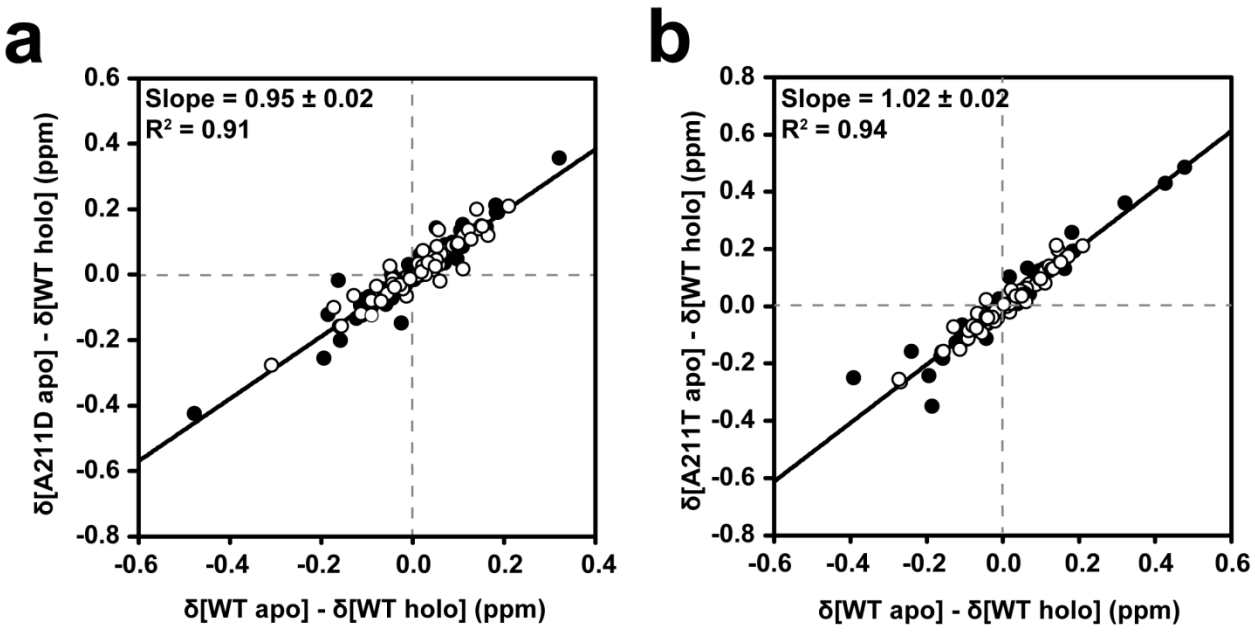

Figure 6. C-terminal PBC mutants A211D/T do not perturb the apo populations of active *vs.* inactive states. (**a**,**b**)Chemical shift correlation plots to measure the change in the overall extent of inactivation in the apo PBC mutants. The slope represents $\frac{X_{Inactive,Mut\ Apo}}{X_{Inactive,WT\ Apo}}$ and is ~1 if little change is occurring to the equilibrium. Open and closed circles denote ^{1}H and ^{15}N chemical shift values, respectively, the latter scale by 0.181. This work was performed by O. Byun under the supervision of K. Moleschi.

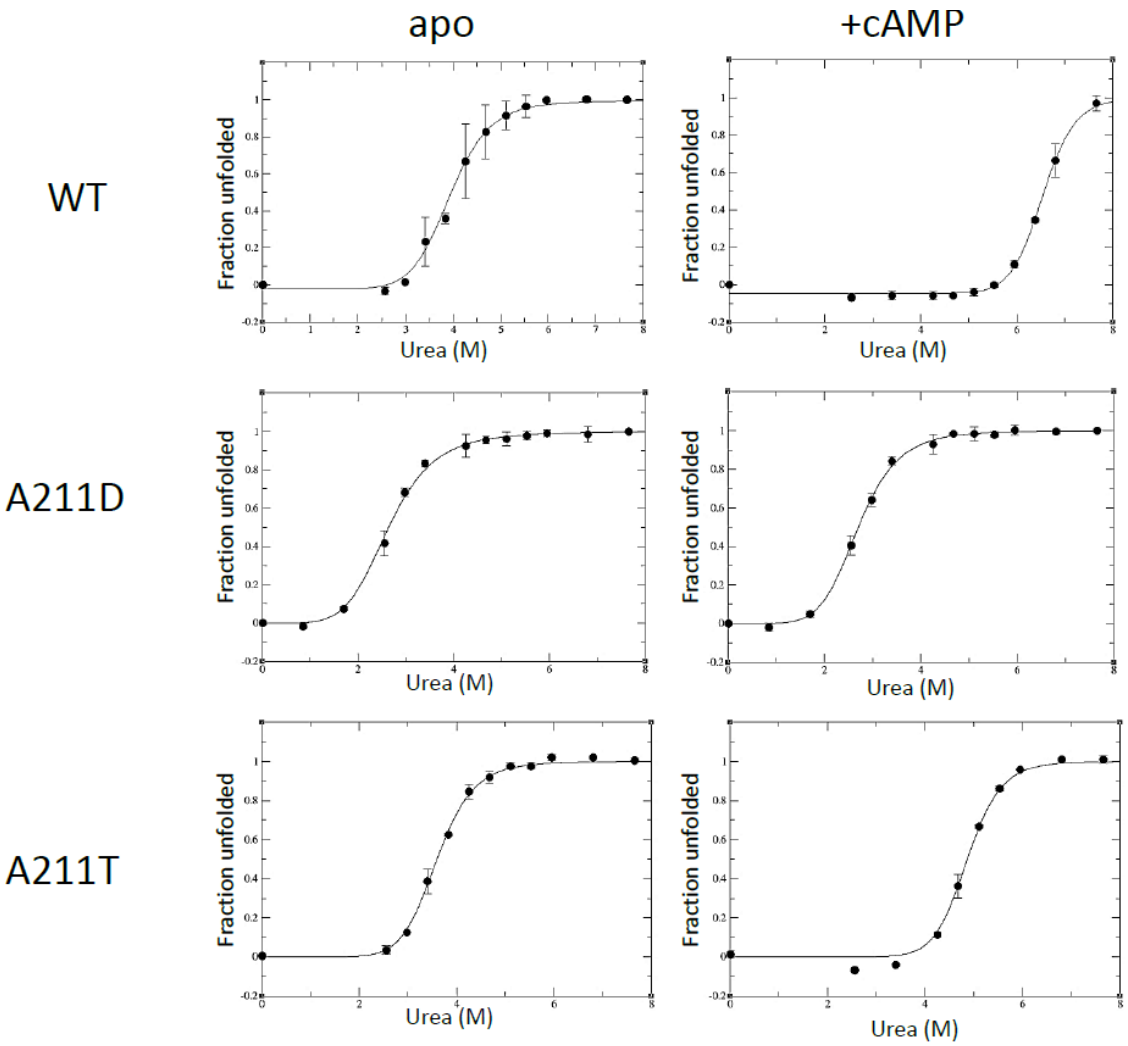

Figure 7. Urea unfolding curves of WT RIα and A221D/T (96-244) in apo and holo forms. The urea-induced unfolding monitored by intrinsic tryptophan fluorescence is shown for apo (left panel) excess cAMP (right panel) forms for WT (top), A211D (middle), and A211 (bottom). Each point was performed in duplicate with error bars indicating standard deviation. This work was performed by O. Byun under the supervision of K. Moleschi.

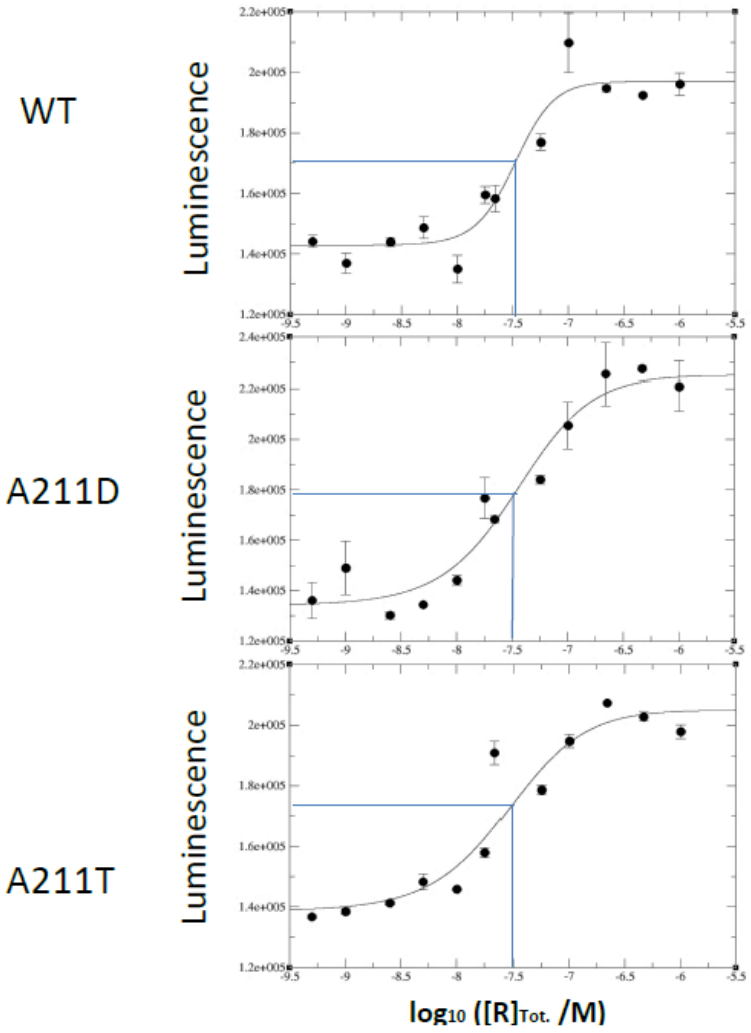

Figure 8. Luminescence based kinase inhibition assays of WT and A211D/T (91-244). Increasing amounts of R-subunit were added to inhibit the activity of C. Larger luminescence values indicate inhibition. Blue lines indicate half maximal inhibition (IC_{50}).Error bars are a measure of standard deviation with samples performed in triplicate. This work was performed by O. Byun under the supervision of K. Moleschi.

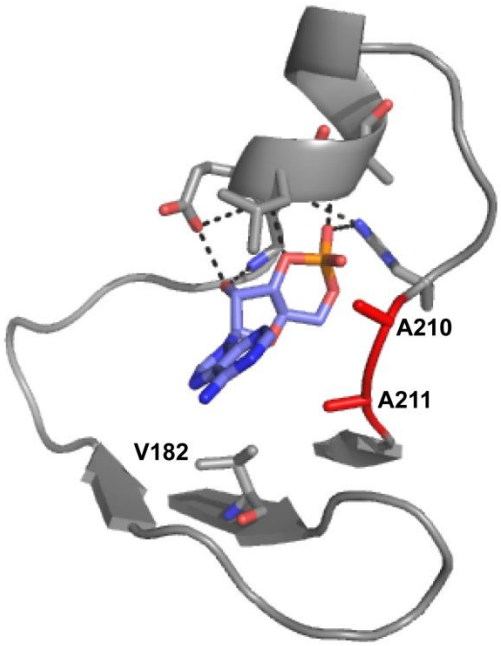

Figure 9. Cartoon representation of the proximity of the C-terminal PBC alanine residues to cAMP. The RIα cAMP binding pocket is shown as a gray ribbon with important cAMP-binding residues shown as gray sticks. C-terminal PBC alanine residues are shown in red and are adjacent to the adenine base of cAMP.

4.9 References

1. Akimoto, M. *et al.* Signaling through dynamic linkers as revealed by PKA. *Proc. Natl. Acad. Sci. U. S. A.* **110,** 14231–6 (2013).

2. Su, Y. *et al.* Regulatory subunit of protein kinase A: structure of deletion mutant with cAMP binding domains. *Science* **269,** 807–813 (1995).

3. Stockman, B. J. & Dalvit, C. NMR screening techniques in drug discovery and drug design. *Prog. Nucl. Magn. Reson. Spectrosc.* **41,** 187–231 (2002).

4. Wu, J., Jones, J. M., Nguyen-Huu, X., Ten Eyck, L. F. & Taylor, S. S. Crystal structures of RIalpha subunit of cyclic adenosine 5'-monophosphate (cAMP)-dependent protein kinase complexed with (Rp)-adenosine 3',5'-cyclic monophosphothioate and (Sp)-adenosine 3',5'-cyclic monophosphothioate, the phosphothioate analogues of cA. *Biochemistry* **43,** 6620–6629 (2004).

5. Dostmann, W. R. G. *et al.* Probing the cyclic nucleotide binding sites of cAMP-dependent protein kinases I and II with analogs of adenosine 3',5'-cyclic phosphorothioates. *J. Biol. Chem.* **265,** 10484–10491 (1990).

6. Das, R. *et al.* Dynamically driven ligand selectivity in cyclic nucleotide binding domains. *J. Biol. Chem.* **284,** 23682–23696 (2009).

7. Lorieau, J. L., Louis, J. M., Schwieters, C. D. & Bax, A. pH-triggered, activated-state conformations of the influenza hemagglutinin fusion peptide revealed by NMR. *Proc. Natl. Acad. Sci. U. S. A.* **109,** 19994–9 (2012).

8. Padmanabhan, S. & Baldwin, R. L. Helix-stabilizing interaction between tyrosine and leucine or valine when the spacing is i, i + 4. *J. Mol. Biol.* **241,** 706–713 (1994).

9. Greene, E. L. *et al.* In vitro functional studies of naturally occurring pathogenic PRKAR1A mutations that are not subject to nonsense mRNA decay. *Hum. Mutat.* **29,** 633–639 (2008).

10. Horvath, A. *et al.* Mutations and polymorphisms in the gene encoding regulatory subunit type 1-alpha of protein kinase a (PRKAR1A): An update. *Hum. Mutat.* **31,** 369–379 (2010).

11. Cazabat, L. *et al.* Inactivation of the carney complex gene 1 (PRKAR1A) alters spatiotemporal regulation of cAMP and cAMP-dependent protein kinase: A study using genetically encoded FRET-based reporters. *Hum. Mol. Genet.* **23,** 1163–1174 (2014).

12. Bertherat, J. *et al.* Mutations in regulatory subunit type 1A of cyclic adenosine 5′-monophosphate-dependent protein kinase (PRKAR1A): Phenotype analysis in 353 patients and 80 different genotypes. *J. Clin. Endocrinol. Metab.* **94,** 2085–2091 (2009).

Chapter 5

Conclusions and Future Directions: PKA-RIα Signal Termination by Mammalian Phosphodiesterase 8A

5.1 Preface

The mini-review within this chapter, co-written by K. Moleschi and Dr. G. Melacini, introduces the PKARIα:PDE8A interaction as a means for cAMP signal termination and was published in the *Biophysical Journal* as an invited commentary. It may be cited as:

Moleschi, K. and Melacini, G. Signaling at Crossroads: The Dialogue between PDEs and PKA is Spoken in Multiple Languages. *Biophys. J.* **2014**, 107, 1259-1260.

The current preliminary experimental work outlined in this chapter was solely performed by K. Moleschi and potentially opens new avenues to pursue in PKA signal termination. The catalytic domain of human PDE8A, in cDNA and protein form, was kindly provided by Dr. Ganesh Anand and colleagues (National University of Singapore).

5.2 Thesis Outline

The affinity of cAMP binding domains (CBDs) for cAMP is mediated through several mechanisms. In this thesis, we reveal two previously unanticipated but key determinants of cAMP-affinity, *i.e.* the position of the *apo* auto-inhibitory equilibrium of CBDs, as well as unique phosphate binding cassette (PBC) side-chains not interacting directly with cAMP. As illustrated in chapter three, observed ligand affinities are simply averages of state-specific association constants weighed by their apo populations. Using disulphide state trapping (*i.e.* molecular staples), in conjunction with NMR chemical shift analyses, saturation transfer competition (STD) experiments, and inhibition kinase assays, we were able to measure the state-specific association constants for domain A of the regulatory subunit Iα of protein kinase A (PKA RIα CBD-A). Surprisingly, these state-specific K_a values are very similar to those reported for a structurally homologous domain, hyperpolarization-activated cyclic nucleotide (HCN) gated ion channels, which binds cAMP with three-orders of magnitude lower affinity. This suggests that their observed cAMP affinities are primarily controlled by the position of the apo inhibitory equilibrium, which are markedly different in these systems. For instance, apo PKA samples the active and inactive conformations with nearly equal probabilities, while this equilibrium is highly skewed in the case of apo HCN (> 90% inactive). Since more high-affinity cAMP active state is present in apo RIα than HCN, this explains the ~10^3-fold difference in cAMP affinity observed between RIα (~nM) and HCN (~μM). Another unique feature of RIα concerns specific side-chain interactions within the PBC

A combination of chemical shift analyses, STD, and urea unfolding, revealed that PBC residues L201, Y205, and A211 are critical in maintain high cAMP affinity in RIα, as outlined in chapter four. Interestingly, mutations of L201 or Y205 to Alanine severely reduced cAMP

affinity, without significantly perturbing the inhibitory pre-equilibrium. The (*i*, *i* + 4) spacing of these Leu and Tyr residues promotes a hydrophobic stack through Van der Waals interactions, which in turn stabilizes the PBC short helix. The (*i*, *i* + 4) L201 and Y205 hydrophobic stack is required for high cAMP affinity, as seen through the reduction of their affinities upon mutation to Alanine. Residue A211 also contributes significantly to cAMP affinity, albeit likely through different mechanisms. The A211 PBC residue hydrophobically caps the adenine base of cAMP, and mutants A211D or A211T are connected to Carney Complex (CNC) and acrodysostosis, respectively. HSQC spectral analyses paired with urea unfolding assays of mutants A211D/T, show that cAMP affinity is adversely affected, again without significantly changing the overall position of the auto-inhibitory equilibrium. This is likely a local effect induced by steric bulk of the Asp or Thr mutation, in combination with electrostatic repulsion between the adjacent cAMP phosphate and Asp/Thr side-chains. The extent of full activation in these mutants remains to be assessed.

5.3 Future Directions

One of the primary mechanisms to regulate the effective concentration of cyclic AMP (cAMP) and cyclic GMP (cGMP) is through the 3',5'-phosphate bond hydrolysis, which is catalyzed by cyclic nucleotide phosphodiesterases (PDEs) (Fig. 1). Hence, PDEs control the amount of cAMP and cGMP second messengers locally available for the activation of a multitude of downstream signalling pathways and, in turn, for the control of a wide array of intracellular responses to extracellular stimuli[1–4]. Because specific subtypes or isoforms within the large PDE superfamily can be selectively inhibited, PDEs are also valuable drug targets. PDE inhibition provides a means to locally activate cAMP and/or cGMP-dependent signalling within

particular subcellular micro-domains, with a selectivity that would be challenging to match through direct activation of downstream cyclic nucleotide receptors.

Among the eukaryotic cyclic nucleotide receptors, protein kinase A (PKA) serves as a primary relay of the cAMP signal and the interplay between PDEs and PKAs is central to the tight regulation of signalling in eukaryotes. The PDE:PKA crosstalk occurs at multiple levels. It has been known for over a decade that PDE and PKA are not only part of coupled feedback loop networks, but they are also co-localized to the same subcellular compartments through A-kinase anchoring proteins (AKAPs)[4]. The combined action of feedback loops and AKAP-mediated subcellular compartmentalization involving specific PDE and PKA isoforms results in an exquisitely fine-tuned spatiotemporal control of the cAMP signal, tailored to specific cellular demands[1–6].

Recently, Krishnamurthyet al.[7] added a new potential dimension in the complex PDE:PKA interplay by exploring the possibility of direct, AKAP-independent PDE/PKA interactions as a complement to AKAP-mediated tethering. Krishnamurthy et al.[7] focused on the Iα isoform of the regulatory subunit of PKA (RIα), which is known to bind cAMP with high affinity (K_D ~ nM), and address a long outstanding question in cAMP signalling: how is the cAMP signal terminated by PDEs after cAMP binds RIα and activates PKA?

When cAMP is sequestered within PKA R, it is inaccessible to PDEs and the approximately nM affinity of RIα for cAMP suggests that, in the absence of direct interactions between R and PDEs, signal termination through PDEs would be kinetically limited by the very slow off-rate for the dissociation of cAMP from RIα. Krishnamurthy et al.[7] propose a brilliant solution to this paradox by hypothesizing that PDEs can bind R, facilitate the dissociation of cAMP from RIα, and channel the cyclic nucleotide substrate directly from the phosphate binding

cassette of RIα to the active site of the PDE (Fig. 2). This hypothesis was inspired by prior work from the same group on PKA and RegA in Dictyostelium discoideum[8] and it is extended here to mammalian PDEs. For this purpose, Krishnamurthy et al.[7] screened several mammalian PDE isoforms for RIα binding, utilizing fluorescence polarization measurements and found that RIα binds PDE8A, a close cAMP-selective PDE homolog of RegA. Although PKA RIα is likely to directly bind other PDE isoforms, the PDE8A:RIα complex was selected for further biophysical studies. The PDE8A/RIα interface was mapped using a combination of peptide arrays, hydrogen/ deuterium exchange mass spectrometry, and computational docking[7].

Although the work of Krishnamurthy et al.[7] opens new perspectives on cAMP signal termination by PDEs, it also generates additional questions that must be addressed through further investigations. First, it will be critical to fully probe the existence and functional relevance of endogenous AKAP-independent R:PDE interactions *in vivo* using, for instance, co-immunoprecipitation methods. Although potential competition between PDEs and the endogenous PKA C-subunit for binding to PKA R is a possible confounding complication, these or other in vivo approaches are also expected to reveal which R isoforms (Iα, IIα, Iβ, and IIβ) bind which PDE sub-types/isoforms. The PDE-versus-PKA R selectivity patterns are anticipated to provide additional means to rationalize the complex crosstalk between PKA and PDE. In this respect, we expect that the contribution of Krishnamurthy et al.[7] could be an example in which biophysics prompts further investigations in cell biology, rather than the other way around, as often observed. If confirmed *in vivo*, the work by Krishnamurthy et al.[7] will reveal a new function of PDEs as additional anchor proteins for PKA and it will be interesting to further dissect the interplay between the AKAP-mediated and the AKAP-independent PDE:PKA cross-talk. For instance, the PKA R:PDE interaction may also occur in the context of AKAP

complexes. Thus, the anchoring protein may provide the subcellular location and limit the range of action of the PKA R:PDE subcomplex.

Second, whereas the docking approach taken by Krishnamurthy et al.[7] was useful to show that the proposed model for the PDE8A:RIα complex is structurally viable, accurate modeling of the PDE:R interactions is challenging due to the inherent dynamic nature of R[3,9], which may change in conformation upon PDE binding. Once the PDE8A:RIα interface is accurately mapped, it may provide a structural rationalization for the selectivity exhibited by RIα for different PDE isoforms. Further structural studies on the PDE8A:RIα complex will also clarify how these interactions involving PKA affect other known PDE8A partners, including the Raf-1 kinase that is also bound to and regulated by PDE8A[10].

Third, it should be considered that, although PDE-assisted weakening of the interactions of cAMP with RIα is a central part of the model proposed by Krishnamurthy et al.[7], the mechanism underlying the reduction of cAMP affinity is still not fully understood. In this respect, it will be critical to reassess the PDE8A:RIα interactions in the context of the allosteric thermodynamic cycle for cAMP-dependent control of PKA[9]. This cycle arises from the coupling of the inhibitory and binding equilibria affecting apo RIα. The apo RIα form is often neglected because it is only minimally and transiently populated in vivo, inasmuch as PKA R is primarily bound to either cAMP or the catalytic subunit of PKA (C). However, the dynamics of apo RIα is believed to be a key determinant of the affinities of RIα for cAMP and C, as well as of PKA activation[9]. Apo RIα samples a dynamic equilibrium of inactive and active conformations[9]. In the case of the RIα cAMP binding domain A, the free energy landscape for the apo inhibitory equilibrium is nearly degenerate, resulting in comparable populations of inactive and active states and in maximal sensitivity to state-selective interactions, such as those with cAMP or C[9].

Whereas cAMP selectively stabilizes the active conformation of RIα, C preferentially binds the inactive state of RIα.

One hypothesis to explain how PDE8A reduces the affinity of cAMP for RIα is to assume that PDE8A, similarly to C, selectively binds the inactive conformation of RIα, thus reducing the effective population of the active state, which binds cAMP with high affinity. As of this writing, this hypothesis is purely speculative, and may not capture the full complexity of PDE:PKA interactions, which may also cause currently uncharacterized structural perturbations. Overall, the work by Krishnamurthy et al.[7] is an important contribution to the field of cAMP signalling and opens new perspectives to understand how PDEs terminate and modulate the cAMP signal in time and space, both in an AKAP-dependent and independent manner.

5.4 Preliminary Results

In an attempt to better understand the specific interaction of RIα:PDE8A described by Krishnamurthy *et al*[7]. we made use of transverse relaxation-optimized spectroscopy (TROSY). Due to the high molecular weight of the 2-domain RIα construct (96-379), in addition to the dimeric PDE8A catalytic subunit, the combined complex MW approaches ~200 kDa, exceeding the limits of more traditional HSQC experiments that require relatively fast molecular tumbling for observable signal line-widths. TROSY-based NMR takes advantage of the slower transverse relaxation, in conjunction with protein deuteration, to observe large MW systems, such as RIα:PDE8A. However, the large MW of this system is even at the border of detection for backbone resonances of ^{2}H-^{15}N labeled proteins. Consequently, it is unlikely that the PDE8A bound RIα cross-peaks are directly detectable even using TROSY and deuteration techniques. Instead, we can rely on residue-specific signal broadening to characterize the binding between

^{2}H-^{15}N labeled RIα and sub-stoichiometric amounts of unlabelled PDE8A. TROSY spectra were acquired for WT RIα (96-379) in the presence of cAMP before and after addition of 0.10 equivalents of PDE8A (Fig. 3). As expected, significant residue-specific intensity losses are observed when PDE8A is added to the RIα sample. Figure 3 shows that the observed intensity losses are not due to sample dilution by the PDE, as in this case we would observe comparable intensity losses across all residues. Hence, the observed changes suggest a direct and specific interaction between RIα (96-379) and PDE8A. The atomic resolution provided by NMR allowed us to dissect the residues perturbed by the proposed PDE:cAMP channelling and how the autoinhibitory equilibrium changes.

We attempted to assess PDE-induced perturbations on RIα using several CBD-A and CBD-B reporter residues. In order to assess the conformational equilibrium of CBD-A, the typical L221 residue was utilized (Fig. 4a)[9]. Interestingly, upon addition of 0.10 equivalents of PDE8A, a minor apo-like population is seen, indicated by the small blue peak on top of the purple resonance. When more PDE is added, there is roughly 50% of cAMP-bound (holo) and cAMP-unbound (apo) samples, but in the slow exchange regime. This suggests that the PDE is incrementally removing cAMP, subjecting this residue to the typical apo-holo slow exchange of CBD-A. Over time, and as more PDE is added, only one peak is seen. This is representative of the apo form, likely due to cAMP hydrolysis. Furthermore, little or no change in peak intensities are observed between 0.10 and 0.20 PDE equivalents for cAMP-free RIα. Although these data may be biased by ongoing cAMP hydrolysis, these observations may suggest that the PDE is not directly altering the autoinhibitory equilibrium through binding, but rather simply through cAMP hydrolysis. Residues of the cAMP binding pocket were than analyzed to see whether the PDE induced cAMP channelling.

In the case of identifying cAMP channelling, residues T207 and T217 were used as well-resolved indicators for PDE-induced perturbations (Fig. 4b). Residue T207 resides within the PBC, while T217 is C-terminal, but adjacent, to the PBC of CBD-A. Consequently, these residues would then be sensitive to cAMP binding/hydrolysis and PDE channelling. Given the intensity loss of T207 with 0.10 equivalents of PDE8A, and with little change in chemical shift, it is likely that the PDE is directly affecting the PBC to channel cAMP out for hydrolysis. The peak continues to diminish with the addition of more PDE. It also remains possible that cAMP hydrolysis would result in loss of intensity for T207 due to slow apo *vs.* holo exchange for this residue. Residue T217 normally exhibits slow apo *vs.* holo chemical exchange, as seen through cAMP titrations. However, in the presence of PDE and during cAMP hydrolysis, residue T217 interestingly switches to the fast exchange regime, and the T217 peaks shift towards the apo peak confirming that CBD-A is becoming more apo-like due to accelerated cAMP exit via substrate channelling. CBD-B was also analyzed in a similar fashion.

Reporter residues of CBD-B were used to gauge any changes in the conformational equilibrium, as well as cAMP hydrolysis. In this case, residue G317 in CBD-B is sufficiently removed from the cAMP binding pocket to primarily report on the chemical exchange between active *vs.* inactive states, similarly to L221 in CBD-A. G317 is subject to slow apo *vs.* holo exchange, and with sequential addition of PDE, resonances move towards the apo form (Fig. 4c). Residues R333 (PBC) and G341 (C-terminal to PBC) were used to monitor cAMP hydrolysis and channelling in CBD-B. In the CBD-B cAMP binding pocket, again similar results are obtained in comparison with CBD-A. A moderate decrease in intensity is observed for R333 with the increasing amounts of PDE8A. Furthermore, the fast-exchanging G341 shifts towards the apo cross-peak with the addition of PDE (Fig. 4d), similar to T217 in CBD-A. In comparing

Fig. 4a,b and c,d, the observed trends are nearly identical. Perhaps cAMP is being simultaneously accessed in both CBD-A and CBD-B by PDE8a, with accelerated removal of cAMP by the PDE. While this is in principle in agreement with PDE-induced cAMP channelling, it may not be the case because at a particular PDE concentration, free cAMP is already being hydrolyzed, thereby driving the equilibrium back towards the apo state. In addition, the PDE concentration was increased to probe the binding interface through signal intensity losses, which may also be equilibrium dependent. This creates a 'moving target' scenario, with more than one condition changing at any given time. As a result, further experimentation with more stable conditions is required to accurately model the complex RIα:PDE interactions. This can be achieved either by using PDE inhibitors and/or by removing cAMP. The latter scenario is easily obtained by taking advantage of the fact that sub-stoichiometric amounts of PDE (*i.e.* 0.1 molar equivalents) are sufficient to revert cAMP-bound RIα, over time, towards the apo form (Fig. 5), as the PDE is highly effective in hydrolyzing cAMP, even if tightly bound to RIα. Hence, in an attempt to map the binding interface, and circumvent the 'moving target' problem, we used apo RIα. By using apo RIα, we avoid time-dependent changes to sample conditions when PDE is present.

It is expected that the PDE8A should bind apo RIα irrespective of whether it is conformationally selective for the active or inactive forms of RIα, since apo RIα ~equally samples both states,. Therefore, TROSY spectra were collected for RIα (96-379) in the absence and presence of 0.20 molar equivalents of PDE8A (Fig. 6a). The normalized peak intensities were then compared between the two forms to map the binding interface, as they report on perturbations by the PDE. Intensities were considered to be significant if they were beyond one standard deviation. Significant intensity changes were then plotted on the two-domain structure

of RIα for mapping. Interestingly, the mapped intensities here match well with regions previously probed by hydrogen-deuterium exchange mass spectrometry (HDXMS)[7]. The majority of the residues are on the 'back' of RIα, distal to both cAMP binding pockets, as shown previously[7]. There are several BBR residues perturbed in both CBD-A and CBD-B, suggesting cAMP channelling by PDE8A. More residues within the cAMP binding pocket are expected to be perturbed. Since the apo from was used in this comparison, the resonance assignment of the binding pocket is much more sparse in comparison to cAMP-bound RIα, resulting in few residues observed. Nonetheless, the data acquired here confirm a specific RIα:PDE8 interaction and are highly corroborative of a previously described binding model[7].

In addition to mapping the binding interface, PDE catalysis was also tracked via one-dimensional ^{1}H spectra to monitor how excess ligands evolve overtime. Using cAMP derivatives as standards, identification of the catalytic products becomes possible (Fig. 7). As expected, the main catalytic product from the PDE is 5'-AMP. Interestingly, there are also minor products of adenosine and adenine. These derivative structures are shown in Figure 8. This occurs both in the presence and absence of RIα for PDE-inclusive samples. There still remains an identified peak in RIα samples. It could be possible that this is a bound form of the ligand, indicated by the significant line broadening of the peak. In conclusion, the more interesting data analysis seems to be on the protein complex side rather than from the small molecule and catalysis perspective.

5.5 Outstanding RIα:PDE8A Questions

It is of great use to selectively stabilize one state of PKA with a non-hydrolyzable cAMP analogue, to increase the extent of residue assignment and better map the PDE interface at residue resolution. This was attempted using both Sp-cAMPs and Rp-cAMPs, which were

previously thought to be non-hydrolysable by PDEs due to the bulkier sulphur-oxygen bond. However, PDE8A was able to hydrolyze both Sp-cAMPs, and Rp-cAMPs. Using the phosphorothioate analogues would then be of little use in stabilizing a specific RIα conformation without equilibrium changes through ligand hydrolysis. This would again introduce the 'moving target' issue.

Rather than tracking binding through ^{2}H-^{15}N TROSY intensity losses, it remains possible to use chemical shift based analyses using ^{2}H-^{13}C (methyl side-chain) TROSY, which offers enhanced sensitivity for high molecular weight systems. This would require enriched media with full deuteration and selectively labelled amino acids or precursors (*i.e.* ^{2}H-^{13}C Ile, Leu, and Val), as well as a complete assignment using triple resonance experiments. While being costly and time consuming, greater information could be extracted about the RIα:PDE8a complex.

As a negative control to confirm specific binding, a mutation could be engineered in RIα to disrupt the PKA and PDE interface, while perturbing RIα as little as possible. Perhaps replacing a small side-chain with a bulky tryptophan, or introducing a polar residue in a natively hydrophobic RIα:PDE8A contact would weaken or abolish binding altogether. In this case, it is expected that TROSY intensities should be approximately unaffected by the addition of PDE. Another possible experimental strategy to separate binding from hydrolysis effects is through PDE inhibitors. Repeat the TROSY intensity change mapping experiment in the presence of PDE inhibitors will provide information of RIα:PDE interactions without biases from hydrolysis. However, it is currently unknown whether PDE inhibitors affect the interaction between PDE and RIα.

In summary, the questions that remain to be addressed about the PDE:PKA R interactions can be recapitulated as follows:

1. Does the PDE preferentially bind the inactive *vs*. active state of CBD-A? Rp-cAMPs and Sp-cAMPS analogues may help address this question if used in conjunction with PDE-inhibitors.
2. As (1) but for CBD-B
3. Does the PDE accelerate the apo *vs*. holo exchange in CBD-A and B? This question can be addressed expanding on the slow-to-fast exchange regime transition observed for T217 and G341 in Figure 4b,d and using ranked HSQC ppm changes.
4. Does the PDE accelerate the apo vs. holo exchange in CBD-B to the same extent as CBD-A?
5. What is the binding interface of RIα for the PDE? This question can be addressed through cross-saturation experiment on unlabeled PDE and deuterated and 15N-labeled apo RIα.
6. What is the structure of PDE-bound RIα? For this methyl TROSY approaches will be necessary, as explained above.
7. Does RIα modify the catalytic turnover of cAMP in any way? In addition to the standards already prepared, phosphorus NMR can be used to simplify spectra and the respective peak assignments.

5.6 Other Leads for Future Research

5.6.1 Disulphide-Trapped Active State of RIα (A150C/S228C)

A disulphide bridged mutant was created for PKA RIα to capture the active state (Fig. 8). By following the selection criteria outlined in chapter three, residues A150 and S228 were identified as they are adjacent in the active state but farther apart in the inactive state. Consequently, the resulting disulphide bridge is adequate in trapping the active state of RIα , as shown in Fig. 9.

5.6.2 Apo and Rp-cAMPs Urea Unfolding

Urea unfolding data exist for PBC mutants L201A, L203A, I204A, and Y205A in the apo and Rp-cAMPs forms (Fig. 10). It still remains unclear how the apo and Rp-cAMPs forms of the mutants are stabilized relative to WT in these respective states.

5.6.3 Rp-cAMPs Chemical Shifts of PBC Mutants

In addition to the unfolding data in the presence of Rp-cAMPs, chemical shift data derived from HSQCs were also collected for mutants L201A and Y205A (Fig. 11). This was used to assess whether there is greater stabilization of the inactive state. Data is yet to be collected for mutants L203A and I204A.

5.6.4 State-Specific Association Constants of RIα for Rp-cAMPs

STD titrations were performed for the RIα disulphide bridge mutants (*ie.* A108C/M234C and E143C/S236C) as well for WT (91-244) with the reverse agonist Rp-cAMPs. Rough K_D measurements were performed (disulphides K_D = ~15 µM, WT K_D = ~40 µM, Fig. 12), but the chemical shift data for the disulphide mutants must be further analyzed, in conjunction with re-examining the binding isotherms, to extract the correction ratios to accurately determine the state-specific association constant of Rp-cAMPs for RIα. In general, the work on state-specific association constants presented in Chapters 2 and 3 can be extended to mutations and cAMP-analogs, although some of the equations used may need to be adapted to these changes (*i.e.* mutant rather than WT or Rp-cAMPS rather than cAMP).

5.6.5 1-Dimensional ^{1}H Time Course of RIα+cAMP PDE Hydrolysis

Data were collected for cAMP hydrolysis in both the presence of and absence of RIα by acquiring ^{1}H spectra over time. As expected, the main product of PDE catalysis is 5'-AMP, with other cAMP derivatives as minor products (Fig. 7). Interestingly, the previously thought non-hydrolyzable phosphorthioate cAMP analogues, *ie.* Sp-cAMPs (Fig. 13) and Rp-cAMPs (Fig. 14) are easily hydrolyzed by PDE8A.

5.6.6 1 Domain RIα (96-244) PDE Trials

In addition to the data collected for two domain RIα (96-379) and PDE, experiments were also performed for the one domain construct (96-244). cAMP-bound RIα (96-244) was made apo by the presence of sub-stoichiometric amounts of PDE, likely due to cAMP channelling (Fig. 15).

5.7 References

1. Maurice, D. H. *et al.* Advances in targeting cyclic nucleotide phosphodiesterases. *Nat. Rev. Drug Discov.* **13,** 290–314 (2014).

2. Stangherlin, a. & Zaccolo, M. Local termination of 3′-5′-cyclic adenosine monophosphate signals: the role of a kinase anchoring protein–tethered. **58,** 345–353 (2011).

3. Smith, F. D. *et al.* Intrinsic disorder within an AKAP-protein kinase A complex guides local substrate phosphorylation. *Elife* **2013,** 1–19 (2013).

4. Carlisle Michel, J. J. *et al.* PKA-phosphorylation of PDE4D3 facilitates recruitment of the mAKAP signalling complex. *Biochem. J.* **381,** 587–592 (2004).

5. Means, C. *et al.* An entirely specific type I A-kinase anchoring protein that can sequester two molecules of protein kinase A at mitochondria. **108,** 1227–1235 (2011).

6. Taylor, S. S., Zhang, P., Steichen, J. M., Keshwani, M. M. & Kornev, A. P. PKA: Lessons learned after twenty years. *Biochim. Biophys. Acta - Proteins Proteomics* **1834,** 1271–1278 (2013).

7. Krishnamurthy, S. *et al.* Active Site Coupling in PDE:PKA Complexes Promotes Resetting of Mammalian cAMP Signaling. *Biophys. J.* **107,** 1426–1440 (2014).

8. Moorthy, B. S., Gao, Y. & Anand, G. S. Phosphodiesterases catalyze hydrolysis of cAMP-bound to regulatory subunit of protein kinase A and mediate signal termination. *Mol. Cell. Proteomics* **10,** M110.002295 (2011).

9. Akimoto, M. *et al.* Signaling through dynamic linkers as revealed by PKA. *Proc. Natl. Acad. Sci. U. S. A.* **110,** 14231–6 (2013).

10. Brown, K. M. *et al.* Phosphodiesterase-8A binds to and regulates Raf-1 kinase. *Proc. Natl. Acad. Sci. U. S. A.* **110,** E1533–42 (2013).

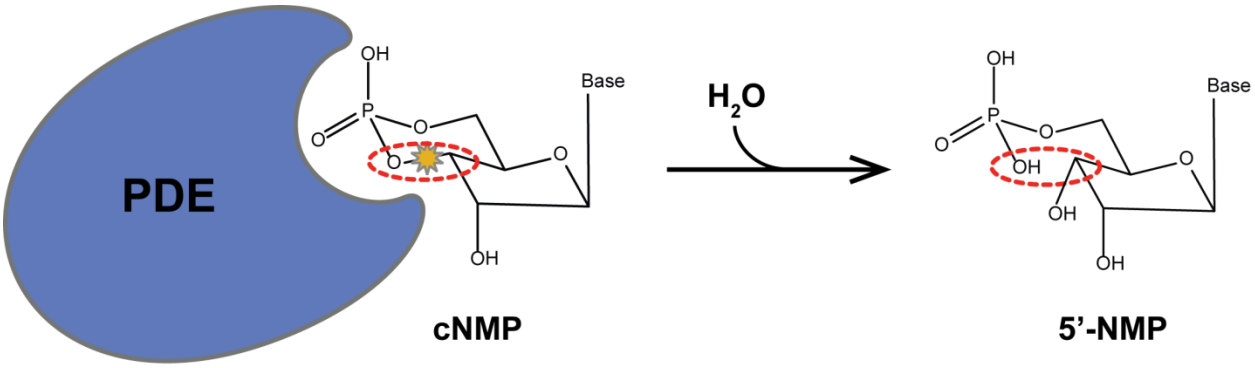

Figure 1. PDE-assisted cyclic nucleotide hydrolysis. General hydrolysis by a generic PDE for a given cyclic nucleotide by breaking of the 3',5'-phosphodiester bond (red dashed oval).

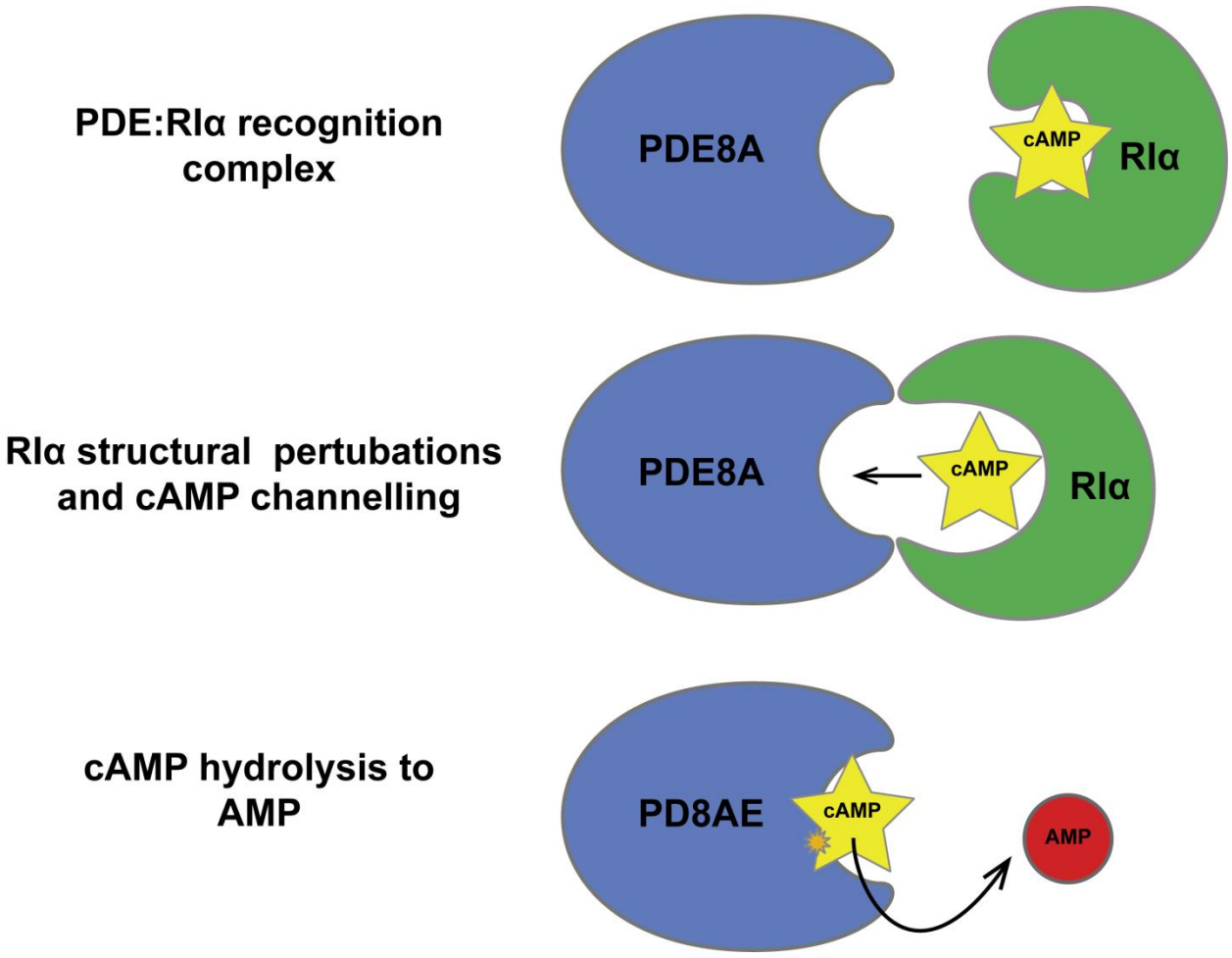

Figure 2. Proposed mechanism of PDE channelling of cAMP from RIα. PDE8A recognizes a specific conformation of RIα and binds. To release cAMP, which is kinetically limited to a slow off rate due to the tight binding between RIα and cAMP, PDE8A structurally perturbs the cAMP binding pocket for subsequent ligand channelling. Once cAMP has moved to the PDE catalytic site, it can then hydrolyze the cyclic bond, thereby converting cAMP to 5'-AMP.

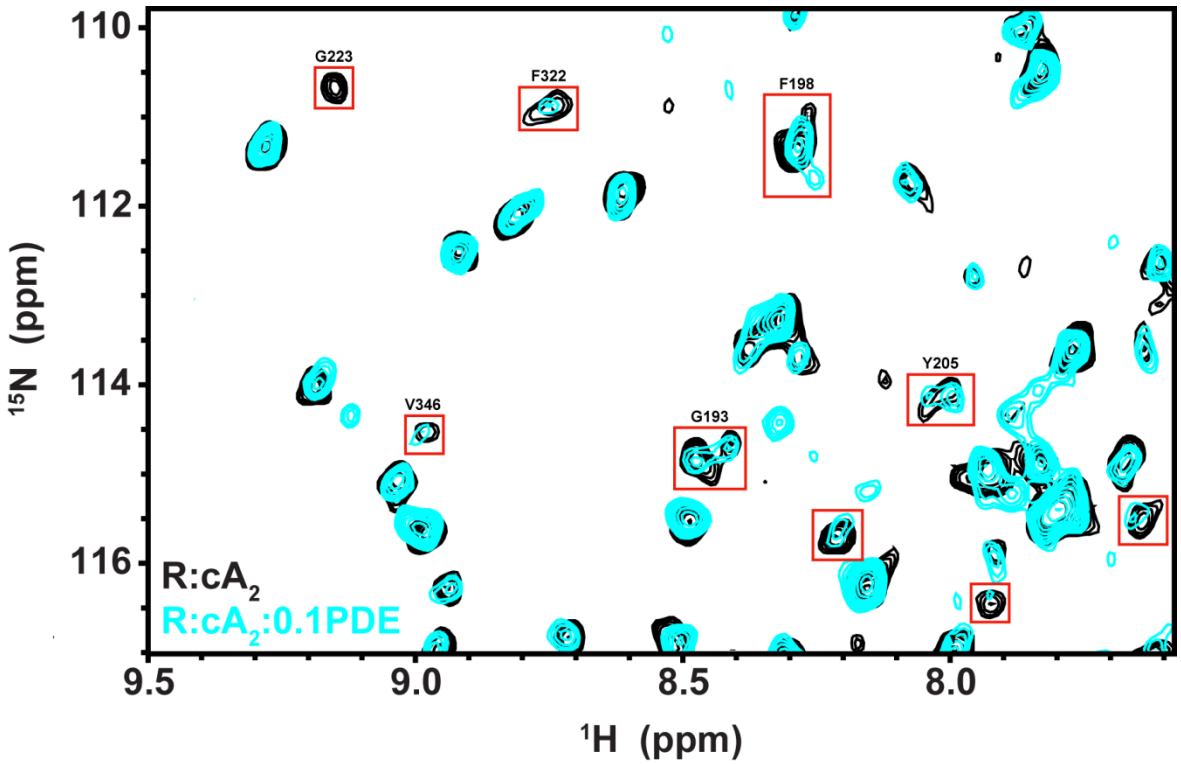

Figure 3. Active ($cAMP_2$-bound) PKA RIα-subunit (96-379) specifically interacts with PDE8A. ^{2}H-^{15}N TROSY spectral overlay of $cAMP_2$-bound RIα (96-379) in the absence of any PDE8A (black) and $cAMP_2$-bound RIα (96-379) in the presence of 0.10 equivalents of PDE8A (cyan). Notable residue-specific signal decreases and resonance broadening are shown in red boxes with the respective assignment, or unlabelled if the assignment is unknown.

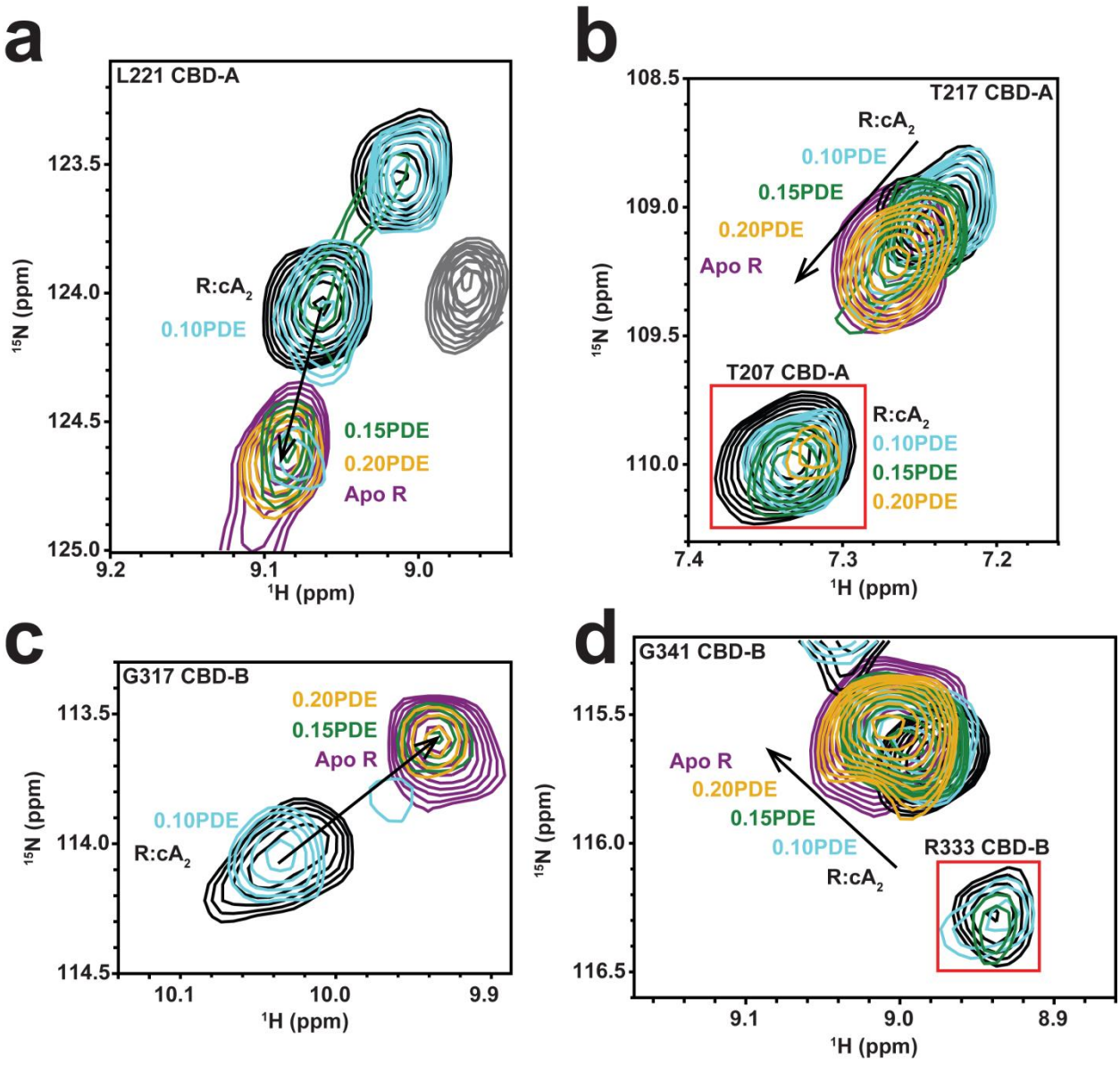

Figure 4. PDE8A-dependent changes in the active *vs.* inactive equilibrium and the amount of bound cAMP in CBD-A and CBD-B of PKA RIα (96-379). (**a-d**) ^{2}H-^{15}N TROSY spectral overlay of RIα +cAMP (black) with 0.10 (light blue), 0.15 (green), and 0.20 (gold) PDE8A equivalents. Residues shown in (a,c) primarily report on the active *vs.* inactive populations, while residues shown in (b,d) are proximal to the binding pocket and are sensitive to the presence of cAMP. Different residues within the same panel are boxed in red. Arrows indicate significant changes in chemical shift. Spectra were acquired ~ 2 h after the addition of each PDE molar equivalent.

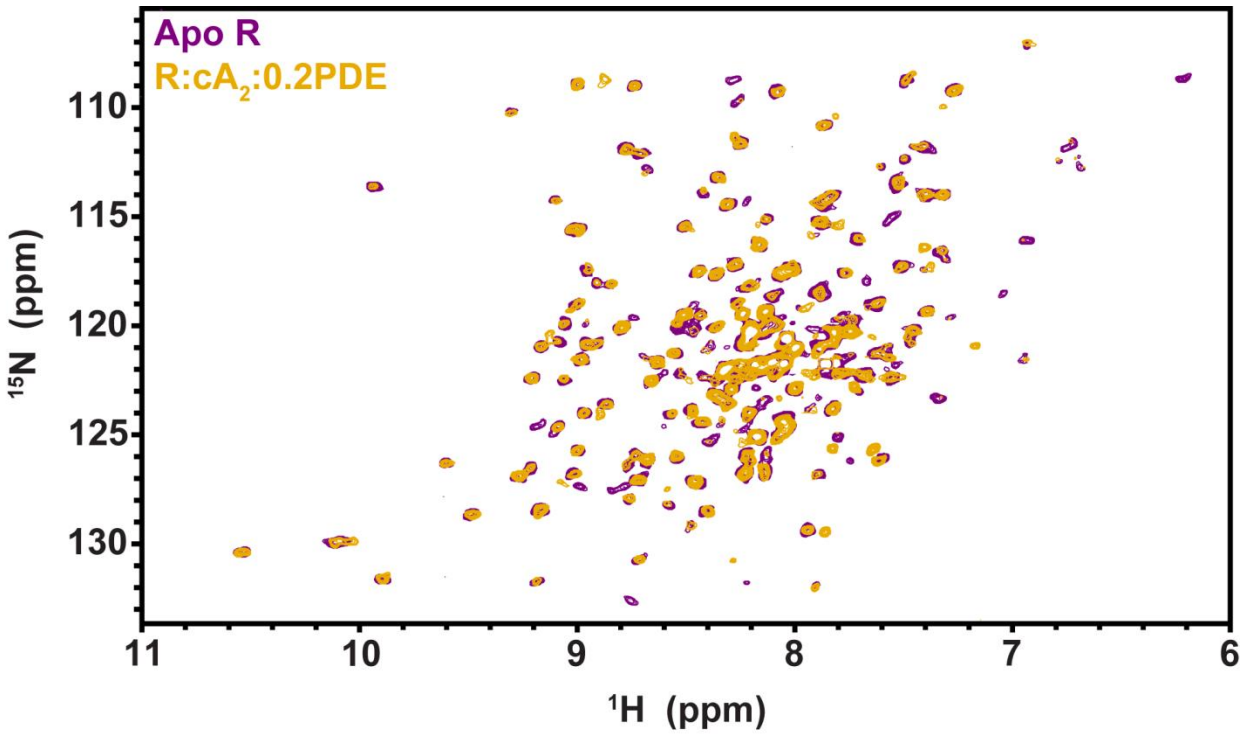

Figure 5. cAMP hydrolysis by PDE8A reverts $cAMP_2$-bound PKA RIα (96-379) back to the apo state. ^{2}H-^{15}N TROSY spectral overlay of apo RIα (purple) and RIα pre-loaded with cAMP to which 0.20 equivalents of PDE8A were added (gold).

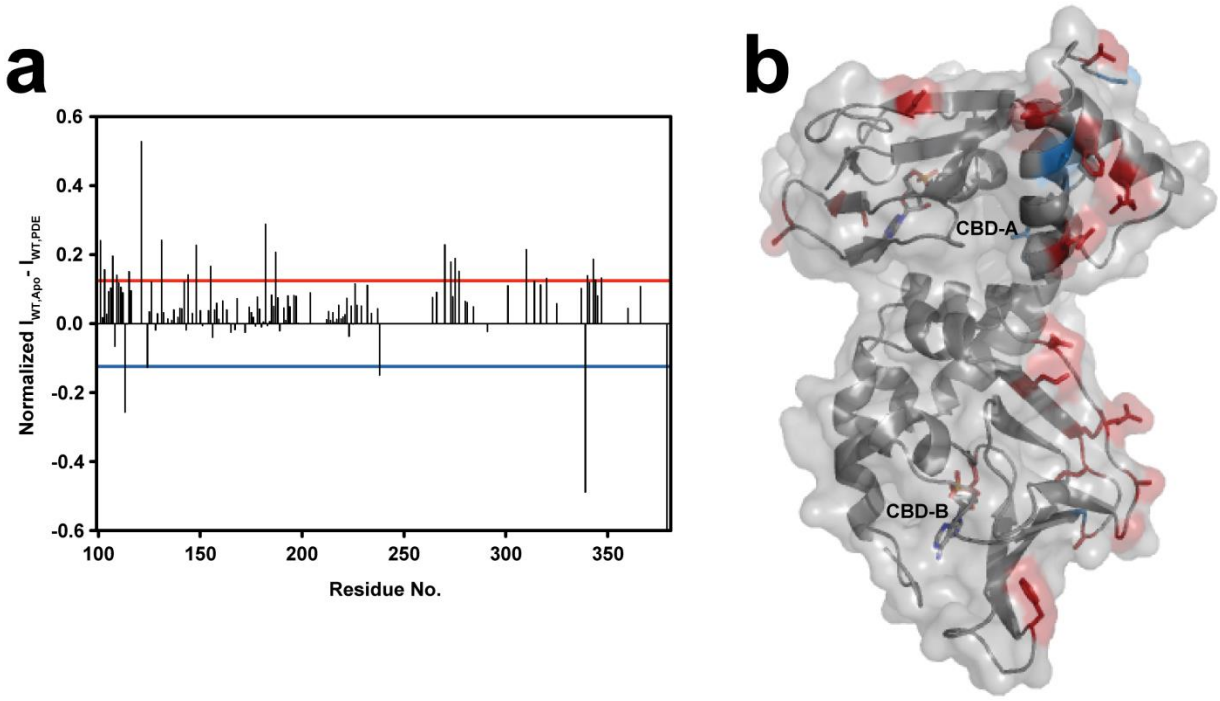

Figure 6. Mapping the RIα:PDE8A binding interface through TROSY-peak intensity changes. (**a**) Peak intensity differences were taken from apo WT RIα and WT RIα with 0.20 molar equivalents of PDE8A at equilibrium. The presence of PDE8A results in significant residue-dependent line broadening, allowing for mapping of the binding interface. Residues with greater than one standard deviation of $I_{WT,Apo} - I_{WT,PDE}$ intensities are above the red line, and indicate intensity losses of RIα:PDE8A in comparison to apo RIα. Residues less than one negative standard deviation are below the blue line, equating to gain in signal intensity. (**b**) Mapped residues of RIα (PDB: 1RGS) with greater than one standard deviation of the intensity differences. The colour code is the same as (a), with cAMP shown as blue sticks.

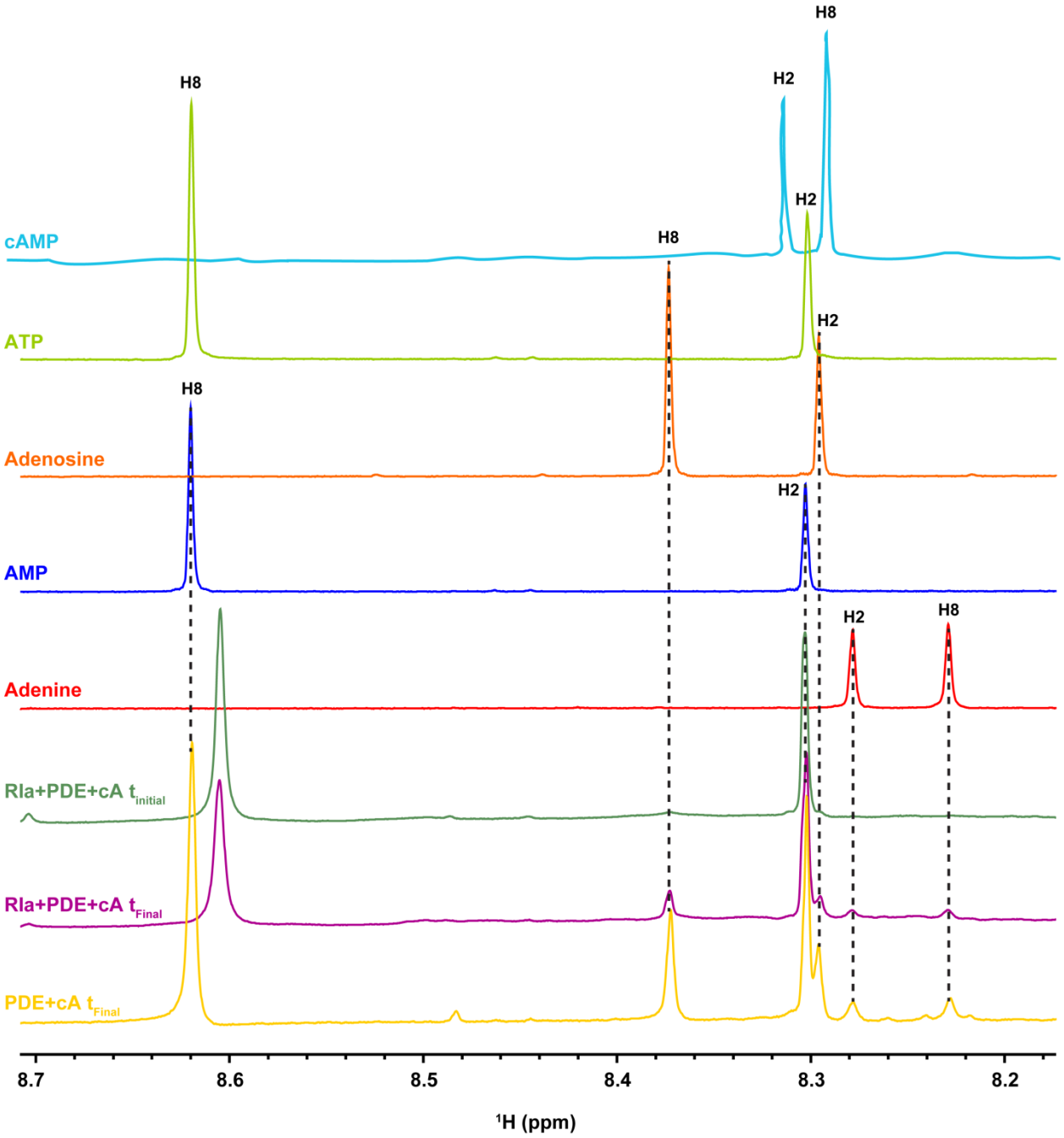

Figure 7. 1D ^{1}H NMR spectra of cAMP derivative standards for the identification of PDE catalytic products. cAMP (light blue), ATP (light green), adenosine (orange), AMP (blue), and adenine (red) were used as standard to assign the peaks in an initial sample (first ~5 min experiment after addition of PDE) of RIα+PDE+cAMP (dark green), final sample (~24 h after addition of initial PDE) of RIα+PDE+cAMP (purple), as well as the PDE and cAMP alone without RIα (yellow). Dotted lines indicate the assignment of the PDE samples.

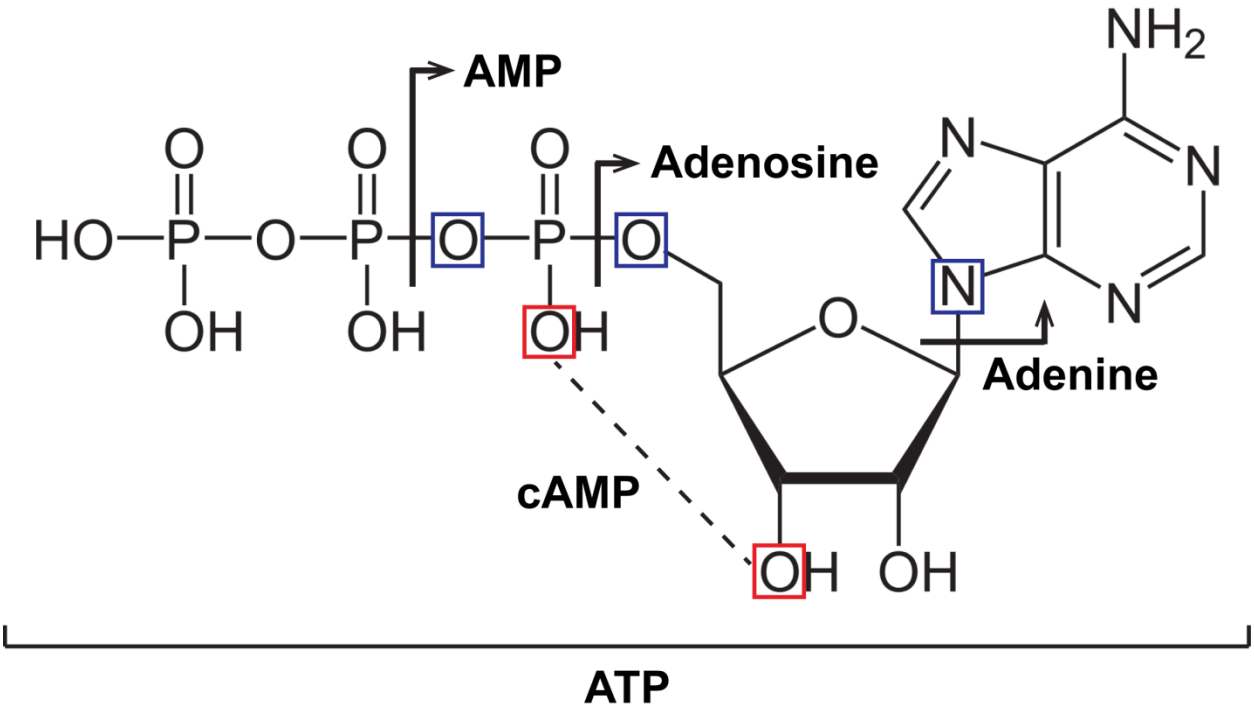

Figure 8. Structures of cAMP derivatives. Adenosine triphosphate (ATP) was used as a structural scaffold to model the other derivatives. The right-angled arrows indicate the structures of the derivatives. Atoms in blue boxes become protonated in the derivative form, while atoms in red boxes become deprotonated. The dashed line represents the formation of the 3'-5'cyclic bond for cAMP, which includes one phosphate moiety.

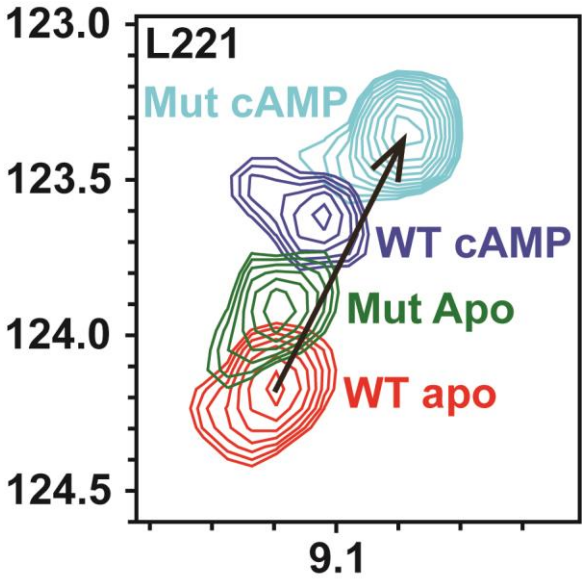

Figure 9. Disulphide state trapping of the active state of RIα (96-244). Overlaid HSQC spectra of WT apo and holo, along with disulphide mutant A150C/S228C also in apo and holo forms.

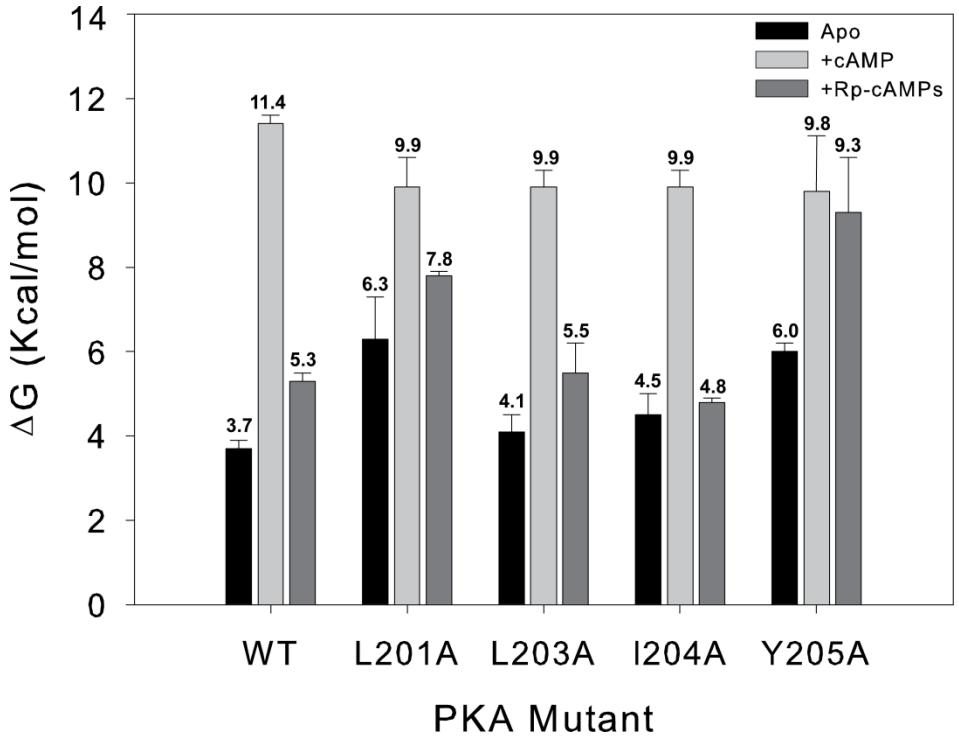

Figure 10. Urea unfolding of apo, +cAMP, and +Rp-cAMPs forms of RIα (91-244). The urea induced unfolding of RIα is shown in the apo (left), cAMP- (middle), and Rp- (right) bound forms.

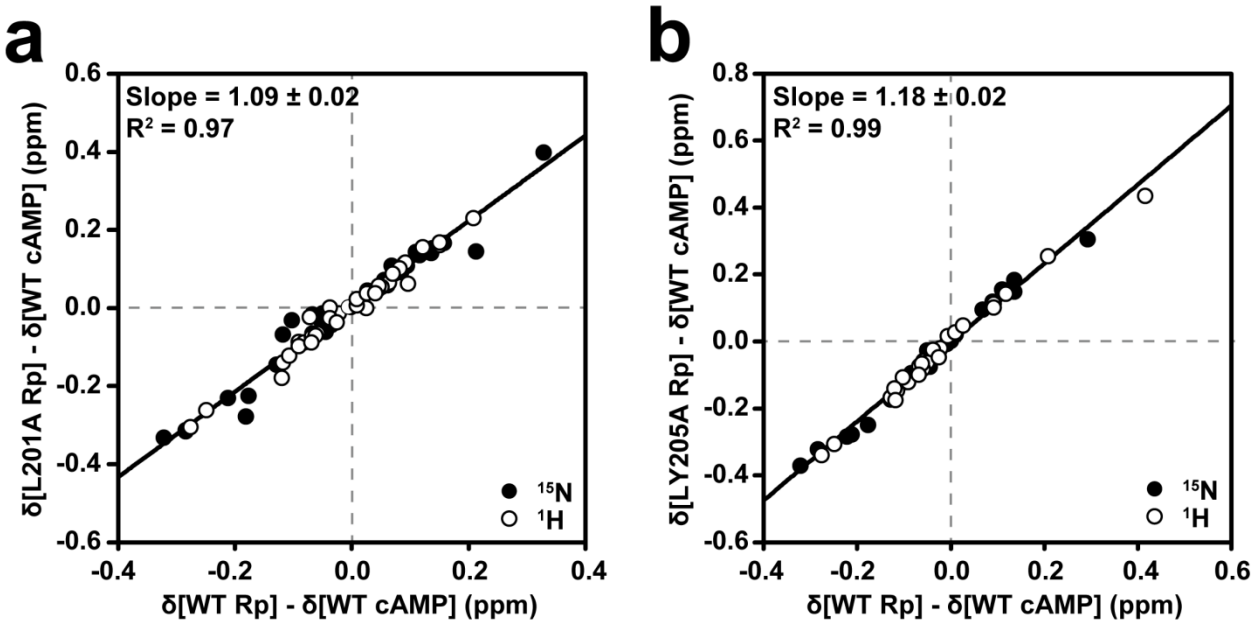

Figure 11. Rp-cAMPS chemical shift analyses of L201A and Y205 PBC mutants. (a,b) Shifts towards inactivation for (a) L201A and (b) Y205A are monitored by $\frac{Mut_{Rp} - WT_{cAMP}}{WT_{Rp} - WT_{cAMP}}$, where the slope reports on the overall population of the inactive form.

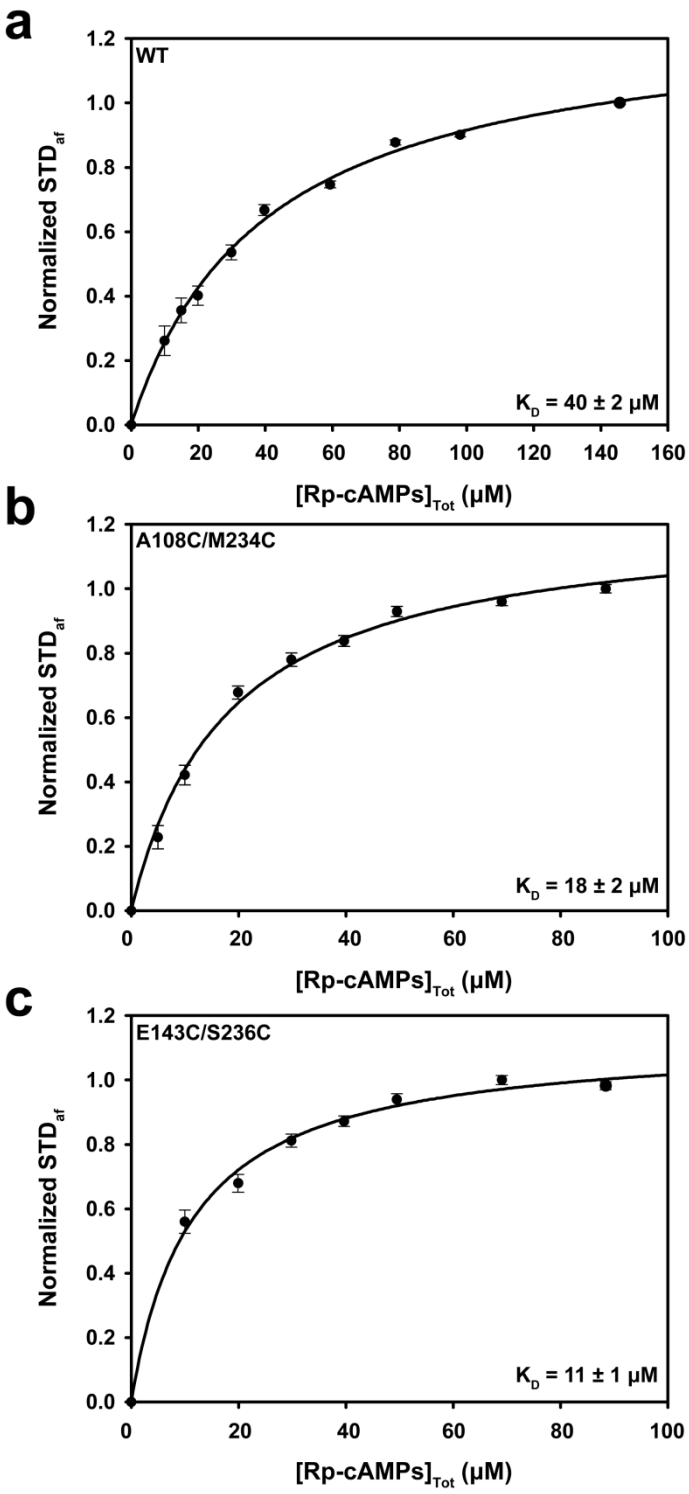

Figure 12. STD-derived binding isotherms of WT RIα and disulphide mutants for Rp-cAMPs. (a-c) Increasing amounts of Rp-cAMPs were added to (a) WT (K_D = 40 ± 2 µM), (b) A108C/M234C (K_D = 18 ± 2 µM), and (c) E143C/S236C (K_D = 11 ± 1 µM) to determine the strength of binding.

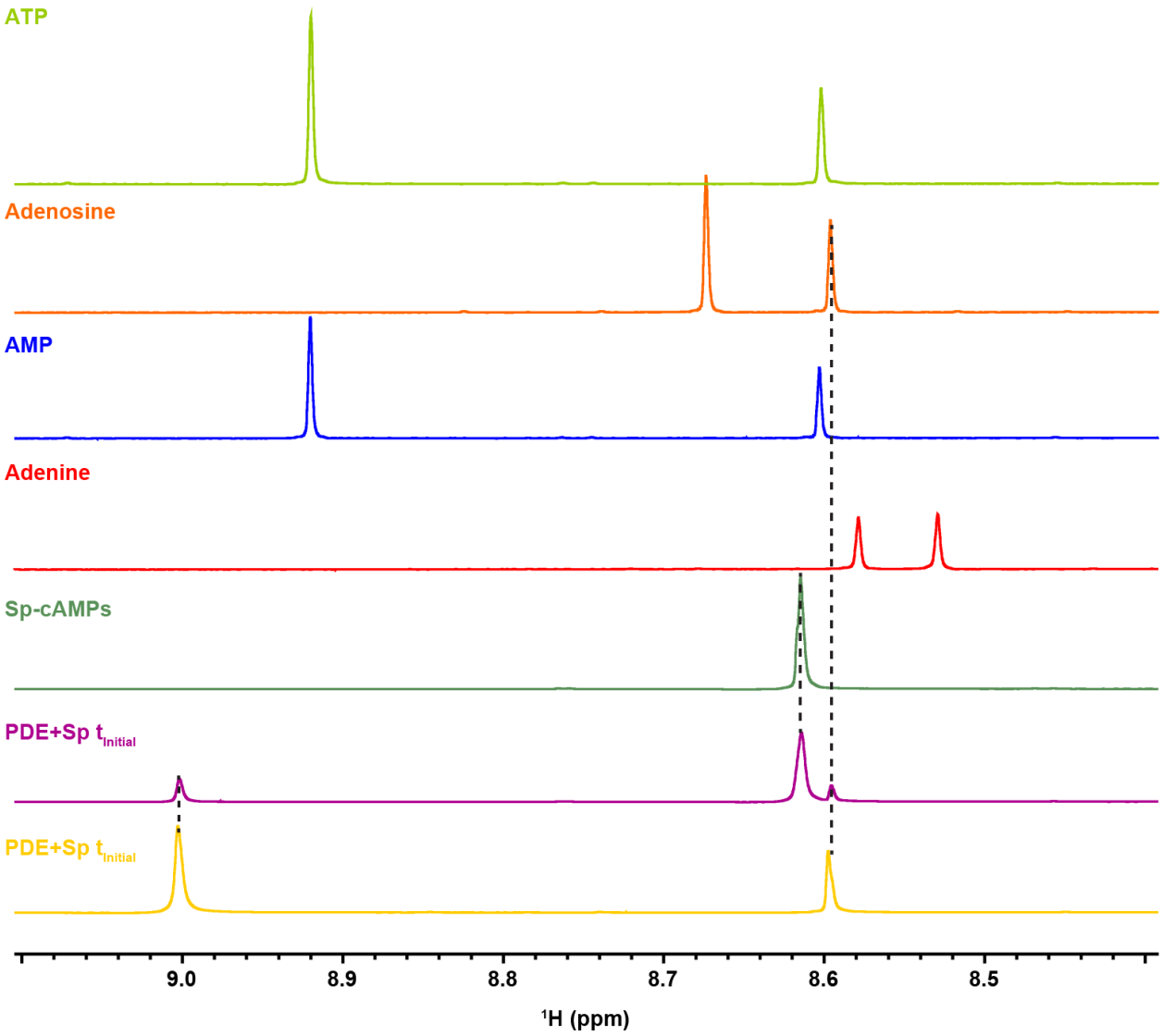

Figure 13. PDE hydrolysis of the phosphorothioate analogue Sp-cAMPs. Initial PDE (first ~5 min experiment after the addition of PDE) +Sp-cAMPs (purple) and final PDE (~24 h after the addition of initial PDE) +Sp-cAMPs (yellow) spectra show the hydrolysis of Sp-cAMPs. Reference cAMP derivative spectra are shown for comparison (ATP: green, adenosine: orange, adenine: red, Sp-cAMPs: green).

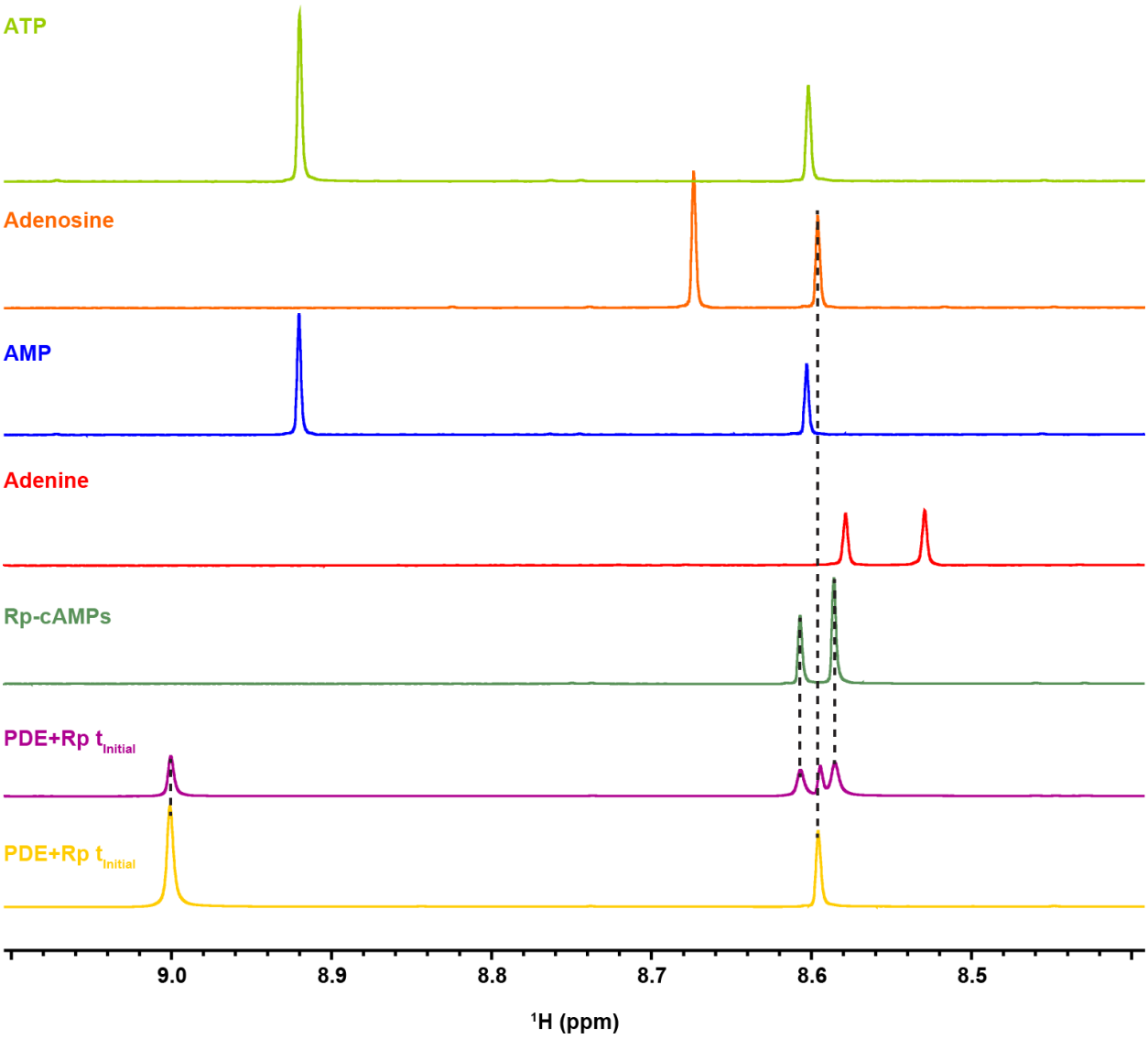

Figure 14. PDE hydrolysis of the phosphorothioate analogue Rp-cAMPs. Initial PDE (first ~5 min experiment after addition of PDE) +Rp-cAMPs (purple) and final PDE (~24 h after the addition of initial PDE) +Rp-cAMPs (yellow) spectra show the hydrolysis of Rp-cAMPs. Reference cAMP derivative spectra are shown for comparison (ATP: green, adenosine: orange, adenine: red, Rp-cAMPs: green).

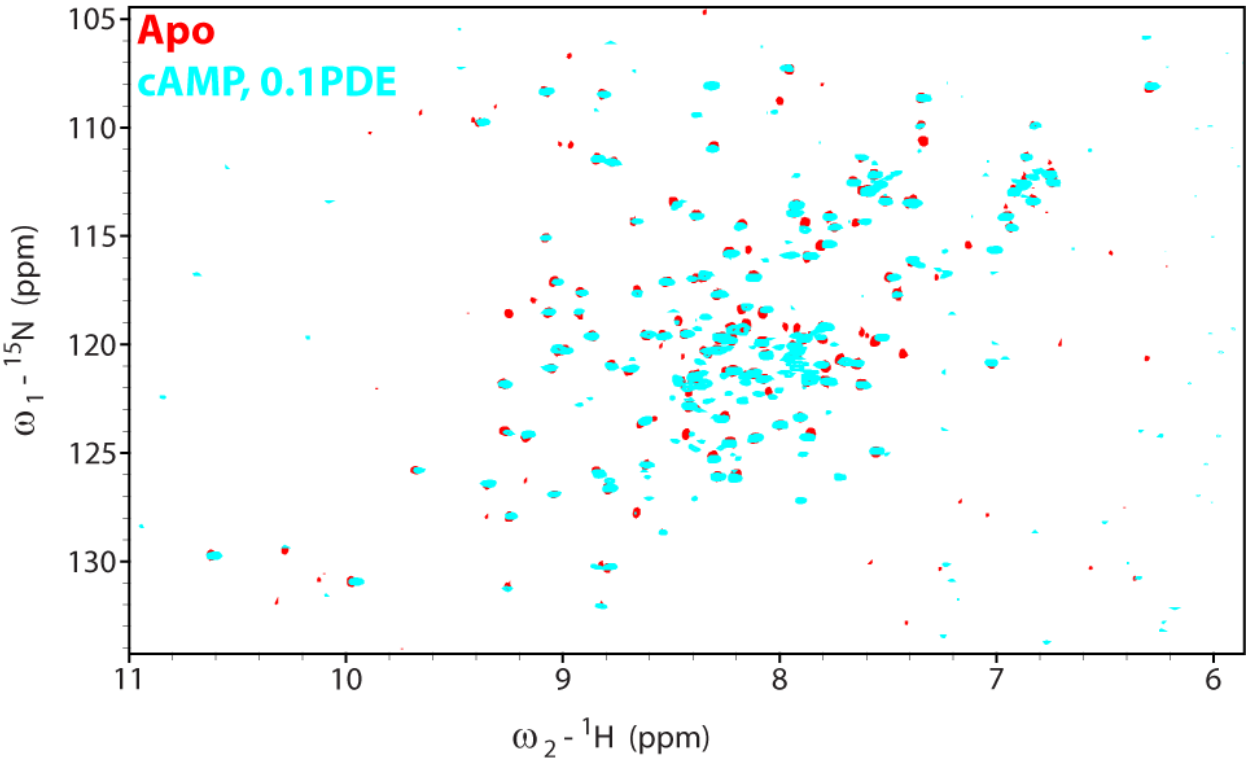

Figure 15. cAMP hydrolysis of holo RIα (96-244) by PDE8A. RIα was initially saturated with excess cAMP (cyan) then supplemented with 0.20 molar equivalents of PDE8A. Within the dead-time of the experiment (~20 min), the sample was made apo. An apo spectrum without PDE (red) is included for comparison.